Galaxy And Mass Assembly (GAMA): stellar mass estimates

Taylor, E.N.; Hopkins, A.M.; Baldry, I.K.; Brown, M.J.I.; Driver, S.P.; Kelvin, L.S.; ... ; Wijesinghe, D.

Monthly Notices
of the
ROYAL ASTRONOMICAL SOCIETY

Mon. Not. R. Astron. Soc. **418,** 1587–1620 (2011) doi:10.1111/j.1365-2966.2011.19536.x

Galaxy And Mass Assembly (GAMA): stellar mass estimates

Edward N. Taylor,[1,2⋆] Andrew M. Hopkins,[3] Ivan K. Baldry,[4] Michael J. I. Brown,[5] Simon P. Driver,[6] Lee S. Kelvin,[6] David T. Hill,[6] Aaron S. G. Robotham,[6] Joss Bland-Hawthorn,[1] D. H. Jones,[5] R. G. Sharp,[7] Daniel Thomas,[8] Jochen Liske,[9] Jon Loveday,[10] Peder Norberg,[11] J. A. Peacock,[11] Steven P. Bamford,[12] Sarah Brough,[3] Matthew Colless,[3] Ewan Cameron,[13] Christopher J. Conselice,[12] Scott M. Croom,[1] C. S. Frenk,[14] Madusha Gunawardhana,[1] Konrad Kuijken,[15] R. C. Nichol,[8] H. R. Parkinson,[11] S. Phillipps,[16] K. A. Pimbblet,[5] C. C. Popescu,[17] Matthew Prescott,[4] W. J. Sutherland,[18] R. J. Tuffs,[19] Eelco van Kampen[9] and D. Wijesinghe[1]

[1]*Sydney Institute for Astronomy, School of Physics, University of Sydney, NSW 2006, Australia*
[2]*School of Physics, The University of Melbourne, Parkville, VIC 3010, Australia*
[3]*Australian Astronomical Observatory, PO Box 296, Epping, NSW 1710, Australia*
[4]*Astrophysics Research Institute, Liverpool John Moores University, Twelve Quays House, Egerton Wharf, Birkenhead CH41 1LD*
[5]*School of Physics, Monash University, Clayton, VIC 3800, Australia*
[6]*School of Physics & Astronomy, University of St Andrews, North Haugh, St Andrews KY16 9SS*
[7]*Research School of Astronomy & Astrophysics, Mount Stromlo Observatory, Weston Creek, ACT 2611, Australia*
[8]*Institute of Cosmology and Gravitation (ICG), University of Portsmouth, Portsmouth PO1 3FX*
[9]*European Southern Observatory, Karl-Schwarzschild-Str. 2, 85748 Garching, Germany*
[10]*Astronomy Centre, University of Sussex, Falmer, Brighton BN1 9QH*
[11]*Institute for Astronomy, University of Edinburgh, Royal Observatory, Blackford Hill, Edinburgh EH9 3HJ*
[12]*Centre for Astronomy and Particle Theory, University of Nottingham, University Park, Nottingham NG7 2RD*
[13]*Department of Physics, Swiss Federal Institute of Technology (ETH-Zürich), 8093 Zürich, Switzerland*
[14]*Institute for Computational Cosmology, Department of Physics, Durham University, Durham DH1 3LE*
[15]*Leiden Observatory, Leiden University, PO Box 9500, 2300 RA Leiden, the Netherlands*
[16]*Astrophysics Group, HH Wills Physics Laboratory, University of Bristol, Tyndall Avenue, Bristol BS8 1TL*
[17]*Jeremiah Horrocks Institute, University of Central Lancashire, Preston PR1 2HE*
[18]*Astronomy Unit, Queen Mary University London, Mile End Road, London E1 4NS*
[19]*Max Planck Institute for Nuclear Physics (MPIK), Saupfercheckweg 1, 69117 Heidelberg, Germany*

Accepted 2011 July 28. Received 2011 July 26; in original form 2011 January 12

ABSTRACT

This paper describes the first catalogue of photometrically derived stellar mass estimates for intermediate-redshift ($z < 0.65$; median $z = 0.2$) galaxies in the Galaxy And Mass Assembly (GAMA) spectroscopic redshift survey. These masses, as well as the full set of ancillary stellar population parameters, will be made public as part of GAMA data release 2. Although the GAMA database does include near-infrared (NIR) photometry, we show that the quality of our stellar population synthesis fits is significantly poorer when these NIR data are included. Further, for a large fraction of galaxies, the stellar population parameters inferred from the optical-plus-NIR photometry are formally inconsistent with those inferred from the optical data alone. This may indicate problems in our stellar population library, or NIR data issues, or both; these issues will be addressed for future versions of the catalogue. For now, we have chosen to base our stellar mass estimates on optical photometry only. In light of our decision to ignore the available NIR data, we examine how well stellar mass can be constrained based on optical data alone. We use generic properties of stellar population synthesis models to

⋆E-mail: ent@physics.usyd.edu.au

demonstrate that restframe colour alone is in principle a very good estimator of stellar mass-to-light ratio, M_*/L_i. Further, we use the observed relation between restframe $(g-i)$ and M_*/L_i for real GAMA galaxies to argue that, modulo uncertainties in the stellar evolution models themselves, $(g-i)$ colour can in practice be used to estimate M_*/L_i to an accuracy of $\lesssim$0.1 dex (1σ). This 'empirically calibrated' $(g-i)$–M_*/L_i relation offers a simple and transparent means for estimating galaxies' stellar masses based on minimal data, and so provides a solid basis for other surveys to compare their results to $z \lesssim 0.4$ measurements from GAMA.

Key words: catalogues – galaxies: evolution – galaxies: formation – galaxies: fundamental parameters – galaxies: stellar content.

1 INTRODUCTION

One of the major difficulties in observationally constraining the formation and evolutionary histories of galaxies is that there is no good observational tracer of formation time or age. In the simplest possible terms, galaxies grow through a combination of continuous and/or stochastic star formation and episodic mergers. Throughout this process – and in contrast to other global properties like luminosity, star formation rate, restframe colour, or luminosity-weighted mean stellar age – a galaxy's evolution in stellar mass is nearly monotonic and relatively slow. Stellar mass thus provides a good, practical basis for evolutionary studies.

Further, it is now clear that stellar mass plays a central role in determining – or at least describing – a galaxy's evolutionary state. Virtually all of the global properties commonly used to describe galaxies – e.g. luminosity, restframe colour, size, structure, star formation rate, mean stellar age, metallicity, local density, and velocity dispersion or rotation velocity – are strongly and tightly correlated (see e.g. Minkowski 1962; Faber & Jackson 1976; Tully & Fisher 1977; Sandage & Visvanathan 1978; Dressler 1980; Djorgovsky & Davis 1987; Dressler et al. 1987; Strateva et al. 2001). One of most influential insights to come from the ambitious wide- and deep-field galaxy censuses of the 2000s has been the idea that most, if not all, of these correlations can be best understood as being primarily a sequence in stellar mass (e.g. Shen et al. 2003; Kauffmann et al. 2003b, 2004; Tremonti et al. 2004; Blanton et al. 2005; Baldry et al. 2006; Gallazzi et al. 2006). Given a galaxy's stellar mass, it is thus possible to predict most other global properties with considerable accuracy. Presumably, key information about the physical processes that govern the process of galaxy formation and evolution are encoded in the forms of, and scatter around, these stellar mass scaling relations.

1.1 Galaxy And Mass Assembly (GAMA)

This paper presents the first catalogue of stellar mass estimates for galaxies in the Galaxy And Mass Assembly (GAMA) survey (Driver et al. 2009, 2011). At its core, GAMA is an optical spectroscopic redshift survey, specifically designed to have near total spectroscopic completeness over a cosmologically representative volume. In terms of survey area and target surface density, GAMA is intermediate and complementary to wide-field, low-redshift galaxy censuses like the Sloan Digital Sky Survey (SDSS; York et al. 2000; Strauss et al. 2002; Abazajian et al. 2009), 2dFGRS (Colless et al. 2001, 2003; Cole et al. 2005), 6dFGS (Jones et al. 2004, 2009), or the MGC (Liske et al. 2003; Driver et al. 2005) and deep-field surveys of the high-redshift Universe like VVDS (Le Fèvre et al. 2005), DEEP-2 (Davis et al. 2003), COMBO-17 (Wolf et al. 2003, 2004), COSMOS and zCOSMOS (Lilly et al. 2007; Scoville et al. 2007). The intermediate-redshift regime ($z \lesssim 0.3$) that GAMA probes is thus largely unexplored territory: GAMA provides a unique resource for studies of the evolving properties of the general galaxy population.

In a broader sense, GAMA aims to unite data from a number of large survey projects spanning nearly the full range of the electromagnetic spectrum, and using many of the world's best telescopes. At present, the photometric backbone of the data set is optical imaging from SDSS and near-infrared (NIR) imaging taken as part of the Large Area Survey (LAS) component of the UKIRT (United Kingdom Infrared Telescope) Infrared Deep Sky Survey (UKIDSS; Dye et al. 2006; Lawrence et al. 2007). *GALEX* UV imaging from the Medium Imaging Survey (MIS; Martin et al. 2005; Morrissey et al. 2007) is available for the full GAMA survey region. At longer wavelengths, mid-infrared imaging is available from the WISE all-sky survey (Wright et al. 2010); far-infrared imaging is available from the *Herschel*-ATLAS project (Eales et al. 2010) and metre-wavelength radio imaging is being obtained using the Giant Metre-wave Radio Telescope (GMRT; PI: M. Jarvis). In the near future, the SDSS and UKIDSS imaging will be superseded by significantly deeper, sub-arcsec resolution optical and NIR imaging from the VST-KIDS project (PI: K. Kuijken) and from the VISTA-VIKING survey (PI: W. Sutherland). Looking slightly further ahead, a subset of the GAMA fields will also be targeted by the ASKAP-DINGO project (PI: M. Meyer), adding 21 cm data to the mix. By combining these many different data sets into a single and truly panchromatic database, GAMA aims to construct 'the ultimate galaxy catalogue', offering the first laboratory for simultaneously studying the active galactic nuclei (AGN), stellar, dust and gas components of large and representative samples of galaxies at low-to-intermediate redshifts.

The stellar mass estimates, as well as estimates for ancillary stellar population (SP) parameters like age, metallicity, and restframe colour, form a crucial part of the GAMA value-added data set. These values are already in use within the GAMA team for a number of science applications. In keeping with GAMA's commitment to providing these data as a useful and freely available resource, the stellar mass estimates described in this paper are being made publicly available as part of the GAMA data release 2, scheduled for mid-2011. Particularly in concert with other GAMA value-added catalogues, and with catalogues from other wide- and deep-field galaxy surveys, the GAMA stellar mass estimates are intended to provide a valuable public resource for studies of galaxy formation and evolution. A primary goal of this paper is therefore to provide a standard reference for users of these catalogues.

1.2 Stellar mass estimation

Stellar mass estimates are generally derived through stellar population synthesis (SPS) modelling (Tinsley & Gunn 1976;

Tinsley 1978; Bruzual 1993). This technique relies on stellar evolution models (e.g. Leitherer et al. 1999; Le Borgne & Rocca-Volmerange 2002; Bruzual & Charlot 2003; Maraston 2005; Percival et al. 2009). Assuming a stellar initial mass function (IMF), these models describe the spectral evolution of a single-aged or simple stellar population (SSP) as a function of its age and metallicity. The idea behind SPS modelling is to combine the individual SSP models according to some fiducial star formation history (SFH), and so to construct composite stellar populations (CSPs) that match the observed properties of real galaxies. The SP parameters – including stellar mass, star formation rate, luminosity-weighted mean stellar age and metallicity, and dust obscuration – implied by such a fit can then be ascribed to the galaxy in question (see e.g. Brinchmann & Ellis 2000; Cole et al. 2001; Bell et al. 2003; Kauffmann et al. 2003a; Gallazzi et al. 2005).

SPS fitting is most commonly done using broad-band spectral energy distributions (SEDs) or spectral indices (see the comprehensive review by Walcher et al. 2011). This presents two interrelated challenges. First is the question of the accuracy and reliability of the spectral models that make up the stellar population library (SPL) used as the basis of the fitting, including both the stellar evolution models that underpin the SSPs, and the SFHs used to construct the CSPs in the SPL. Secondly, there is the question of what SED or spectral features provide the strongest and/or most robust constraints on a galaxy's SP, taking into account the uncertainties and assumptions intrinsic to the models.

In principle, the accuracy of SPS-derived parameter estimates is limited by generic degeneracies between different SP models with the same or similar observable properties – for example, the well-known dust–age–metallicity degeneracy (see e.g. Worthey 1994). Further, the SPS fitting problem is typically badly underconstrained, inasmuch as it is extremely difficult to place meaningful constraints on a given galaxy's particular SFH. This issue has been recently explored by Gallazzi & Bell (2009), who tested their ability to recover the known SP parameters of mock galaxies, in order to determine the limiting accuracy of stellar mass estimates. In the highly idealized case that the SPL contains a perfect description of each and every galaxy, that the photometry is perfectly calibrated and that the dust extinction is known exactly, Gallazzi & Bell (2009) argue that SP model degeneracies mean that both spectroscopic and photometric stellar mass estimates are generically limited to an accuracy of $\lesssim$0.2 dex for galaxies with a strong burst component, and $\sim$0.10 dex otherwise.

In practice, the dominant uncertainties in SPS-derived parameter estimates are likely to come from uncertainties inherent to the SSP models themselves. Despite the considerable progress that has been made, there remain a number of important 'known unknowns'. The form and universality (or otherwise) of the stellar IMF is a major source of uncertainty (van Dokkum 2008; Wilkins et al. 2008; Gunawardhana et al. 2011). From the stellar evolution side, the treatment of NIR-luminous thermally pulsating asymptotic giant branch (TP-AGB) stars is the subject of some controversy (Maraston 2005; Maraston et al. 2006; Kriek et al. 2010). As a third example, there is the question of how to appropriately model the effects of dust in the interstellar medium (ISM), including both the form of the dust obscuration/extinction law, and the precise geometry of the dust with respect to the stars (Driver et al. 2007; Wuyts et al. 2009; Wijesinghe et al. 2011). Many of these uncertainties and their propagation through to stellar mass estimates are thoroughly explored and quantified in the excellent work of Conroy, Gunn & White (2009) and Conroy & Gunn (2010), who argue that (when fitting to full UV-to-NIR SEDs) the net uncertainty in any individual $z \sim 0$ stellar mass determination is on the order of $\lesssim$0.3 dex.

Differential systematic errors across different galaxy populations – that is, biases in the stellar masses of galaxies as a function of their mass, age, SFH, etc. – are at least as great a concern as the net uncertainty on any individual galaxy. The vast majority of stellar mass-based science focuses on differences in the (average) properties of galaxies as a function of inferred mass. In such comparative studies, differential biases have the potential to induce a spurious signal, or, conversely, to mask true signal. In this context, Taylor et al. (2010b) have used the consistency between stellar and dynamical mass estimates for SDSS galaxies to argue that any such differential biases in M_*/L_i (cf. M_*) as a function of SP are limited to $\lesssim$0.12 dex (40 per cent), i.e. small.

In a similar way, systematic differential biases in the masses and SP parameters of galaxies at different redshifts are a major concern for evolutionary studies, inasmuch as any such redshift-dependent biases will induce a false evolutionary signal. Indeed, for the specific example of measurement of the evolving comoving number density of massive galaxies at $z \lesssim 2$, such differential errors are the single largest source of uncertainty, random or systematic (Taylor et al. 2009). More generally, such differential biases will be generically important whenever the low-redshift point makes a significant contribution to the evolutionary signal; that is, whenever the amount of evolution is comparable to the random errors on the high-redshift points. In this context, by probing the intermediate-redshift regime and thus providing a link between $z \approx 0$ surveys like SDSS and 2dFGRS and $z \gg 0$ deep surveys like VVDS and DEEP-2, GAMA makes it possible to identify and correct for any such differential effects. GAMA thus has the potential to significantly reduce or even eliminate a major source of uncertainty for a wide variety of lookback survey results.

1.3 This work

Before we begin, a few words on the ethos behind our SPS modelling procedure: we have deliberately set out to do things as simply and as conventionally as is possible and appropriate. There are two main reasons for this decision. First, this is only the first generation of stellar mass estimates for GAMA. We intend to use the results presented here to inform and guide future improvements and refinements to our SPS fitting algorithm. Secondly, in the context of studying galaxy evolution, GAMA's unique contribution is to probe the intermediate-redshift regime; GAMA becomes most powerful when combined with very wide low-redshift galaxy censuses on the one hand, and with very deep lookback surveys on the other. To maximize GAMA's utility, it is therefore highly desirable to provide masses that are directly comparable to estimates used by other survey teams. This includes using techniques that are practicable for high-redshift studies.

With all of the above as background, the programme for this paper is as follows. After describing the subset of the GAMA database that we will make use of in Section 2, we lay out our SPS modelling procedure in Section 3. In particular, in Section 3.4, we show the importance of taking a Bayesian approach to SP parameter estimation.

In Section 4, we look at how our results change with the inclusion of NIR data. Specifically, in Section 4.1, we show that our SPL models do not yield a good description of the GAMA optical-to-NIR SED shapes. Further, in Section 4.2, we show that for a large fraction of galaxies, the SP parameter values derived from the full optical-plus-NIR SEDs are formally inconsistent with those

derived from just the optical data. Both of these statements are true irrespective of the choice of SSP models used to construct the SPL (Section 4.3).

In order to interpret the results presented in Section 4, we have conducted a set of numerical experiments designed to test our ability to fit synthetic galaxies photometry, and to recover the 'known' SP parameters of mock galaxies. Based on these tests, which we describe in Appendix A, we have no reason to expect the kinds of differences found in Section 4 – we therefore conclude that, at least for the time being, it is better for us to ignore the available NIR data (Section 4.5).

In light of our decision not to use the available NIR data, in Section 5, we investigate how well optical data can be used to constrain a galaxy's M_*/L. Using the SPL models, we show in Section 5.2 that, in principle, $(g-i)$ colour can be used to estimate M_*/L_i to within a factor of $\lesssim$2. In Section 5.3, we use the empirical relation between (*ugriz*-derived) M_*/L_i and $(g-i)$ colour to show that, in practice, $(g-i)$ can be used to infer M_*/L_i to an accuracy of $\approx$0.1 dex. The derived colour–M/L relation presented in this section is provided to enable meaningful comparison between stellar mass-centric measurements from GAMA and other surveys.

Finally, in Section 6, we discuss how we might improve on the current SP parameter estimates for future catalogues. In particular, in Section 6.2, we examine potential causes and solutions for our current problems in incorporating the NIR data. In this section, we suggest that we have reached the practical limit for SP parameter estimation based on grid-search-like algorithms using a static SPL. In order to improve on the current estimates, future efforts will require a fundamentally different conceptual approach. However, as we argue in Section 6.1, this will not necessarily lead to significant improvements in the robustness or reliability of our stellar mass estimates.

Separately, we compare the SDSS and GAMA photometry and stellar mass estimates in Appendix B. Despite there being large and systematic differences between the SDSS `model` and GAMA `auto` SEDs, we find that the GAMA- and SDSS-derived M_*/Ls are in excellent agreement. On the other hand, we also show that, as a measure of total flux, the SDSS `model` photometry suffers from structure-dependent biases; the differential effect is at the level of a factor of 2. These large and systematic biases in total flux translate directly to biases in the inferred total mass. For SDSS, this may in fact be the single largest source of uncertainties in their stellar mass estimates. In principle, this will have a significant impact on stellar mass-centric measurements based on SDSS data.

Throughout this work, we adopt the concordance cosmology: $(\Omega_\Lambda, \Omega_\mathrm{m}, h) = (0.7, 0.3, 0.7)$. Different choices for the value of h can be accommodated by scaling any and all absolute magnitudes or total stellar masses by $+5\log h/0.7$ or $-2\log h/0.7$, respectively (i.e. a higher value of the Hubble parameter implies a lower luminosity or total mass). All other SP parameters, including restframe colours, ages, dust extinctions and mass-to-light ratios, can be taken to be cosmology-independent, inasmuch as they pertain to the SPs at the time of observation. Our stellar mass estimates are based on the Bruzual & Charlot (2003, hereafter BC03) SSP models; we briefly consider the effect of using the Maraston (2005, hereafter M05) models or a 2007 update to the BC03 models (hereafter CB07; see also Bruzual 2007) in Section 4.3. We assume a Chabrier (2003) IMF, and use the Calzetti et al. (2000) dust obscuration law. In discussions of stellar mass-to-light ratios, we use M_*/L_X to denote the ratio between stellar mass and luminosity in the restframe *X*-band; where the discussion is generic to all (optical and NIR) bands, we will drop the subscript for convenience. In all cases, the L_X in M_*/L_X should be understood as referring to the absolute luminosity of the galaxy, i.e. without correction for internal dust extinction. We thus consider effective, and not intrinsic, stellar mass-to-light ratios. Unless explicitly stated otherwise, quantitative values of M_*/L_Xs are given using units of L_X equivalent to an AB magnitude of 0 (rather than, say, $\mathrm{L}_{\odot,\mathrm{X}}$). All quoted magnitudes use the AB system.

2 DATA

2.1 Spectroscopic redshifts

The lynchpin of the GAMA data set is a galaxy redshift survey targeting three $4^\circ \times 12^\circ$ equatorial fields centred on $9^\mathrm{h}00^\mathrm{m} + 1^\mathrm{d}$, $12^\mathrm{h}00^\mathrm{m} + 0^\mathrm{d}$ and $14^\mathrm{h}30^\mathrm{m} + 0^\mathrm{d}$ (dubbed G09, G12 and G15, respectively), for an effective survey area of 144 square degrees. Spectra were taken using the AAOmega spectrograph (Saunders et al. 2004; Sharp et al. 2006), which is fed by the 2dF fibre positioning system on the 4-m Anglo-Australian Telescope (AAT). The algorithm for allocating 2dF fibres to survey targets, described by Robotham et al. (2010) and implemented for the second and third years of observing, was specifically designed to optimize the spatial completeness of the final catalogue. Observations were made using AAOmega's 580V and 385R gratings, yielding continuous spectra over the range 3720–8850 Å with an effective resolving power of $R \approx 1300$. Observations for the first phase of the GAMA project, GAMA I, have recently been completed in a 68 night campaign spanning 2008–2010. GAMA has just been awarded AAT long-term survey status with a view to trebling its survey volume; observations for GAMA II are underway, and will be completed in 2012.

Target selection for GAMA I has been done on the basis of optical imaging from SDSS (DR6; Adelman-McCarthy et al. 2008) and NIR imaging from UKIRT, taken as part of the UKIDSS LAS (Dye et al. 2006; Lawrence et al. 2007). The target selection is described in full by Baldry et al. (2010). In brief, the GAMA spectroscopic sample is primarily selected on *r*-band magnitude, using the (Galactic/foreground extinction-corrected) `petro` magnitudes given in the basic SDSS catalogue. The main sample is magnitude-limited to $r_\mathtt{petro} < 19.4$ in the G09/G15 fields, and $r_\mathtt{petro} < 19.8$ in G12. (The definitions of the SDSS `petro` and `model` magnitudes can be found in Section B1.) In order to increase the stellar mass completeness of the sample, there are two additional selections: $z_\mathtt{model} < 18.2$ or $K_\mathtt{auto} < 17.6$ (AB). For these two additional selections, in order to ensure both photometric reliability and a reasonable redshift success rate, it is also required that $r_\mathtt{model} < 20.5$. The effect of these additional selections is to increase the target density marginally by $\sim$7 per cent (1 per cent) in the G09/G15 (G12) fields. Star–galaxy separation is done based on the observed shape in a similar manner as for the SDSS (see Baldry et al. 2010; Strauss et al. 2002, for details), with an additional $(J-K)-(g-i)$ colour selection designed to exclude those double/blended stars that still fall on the stellar locus in colour–colour space.

To these limits, the survey spectroscopic completeness is high ($\gtrsim$98 per cent; see Driver et al. 2011; Liske et al., in preparation). The issue of photometric incompleteness in the target selection catalogues is being investigated by Loveday et al. (2011) using SDSS Stripe 82: the SDSS imaging completeness is >99 (90) per cent for $\mu < 22.5$ (23) mag arcsec^{-2}.

The process for the reduction and analysis of the AAOmega spectra is described in Driver et al. (2011). All redshifts have been measured by GAMA team members at the telescope, using the interactive redshifting software RUNZ (developed by Will Sutherland and now maintained by Scott Croom). For each reduced and

sky-subtracted spectrum, RUNZ presents the user with a first redshift estimate. Users are then free to change the redshift in the case that the RUNZ-derived redshift is deemed incorrect, and are always required to give a subjective figure of merit for the final redshift determination.

To ensure the uniformity and reliability of both the redshifts and the quality flags, a large subset (approximately 1/3, including all those with redshifts deemed 'maybe' or 'probably' correct) of the GAMA spectra have been independently 're-redshifted' by multiple team members. The results of the blind re-redshifting are used to derive a probability for each redshift determination, p_z, which also accounts for the reliability of the individual who actually determined the redshift (Liske et al., in preparation). The final values of the redshifts and quality flags, `nQ`, given in the GAMA catalogues are then based on these 'normalized' probabilities. (Note that this work makes use of 'year 3' redshifts, which had not yet undergone the re-redshifting process.) Driver et al. (2011) suggest that the redshift 'blunder' rate for galaxies with $\texttt{nQ} = 3$ (corresponding to $0.90 < p_z < 0.95$) is in the range 5–15 per cent, and that for $\texttt{nQ} = 4$ (corresponding to $p_z > 0.95$) is 3–5 per cent. A more complete analysis of the GAMA redshift reliability will be provided by Liske et al. (in preparation).

The redshifts derived from the spectra are, naturally, heliocentric. For the purposes of calculating luminosity distances (see Section 3.2), we have computed flow-corrected redshifts using the model of Tonry et al. (2000). The details of this conversion will be given by Baldry et al. (2011).

The GAMA I main galaxy sample ($\texttt{SURVEY\_CLASS} \geq 4$ in the GAMA catalogues) comprises 119 852 spectroscopic targets, of which 94.5 per cent (113 267/119 852) now have reliable ($\texttt{nQ} \geq 3$) spectroscopic redshifts. Of the reliable redshifts, 83 per cent (94448/113267) are measurements obtained by GAMA. The remainder are taken from previous redshift surveys, principally SDSS (DR7; Abazajian et al. 2009, 13 137 redshifts), 2dFGRS (Colless et al. 2003, 3622 redshifts) and MGCz (Driver et al. 2005, 1647 redshifts). As a function of SDSS `fiber` magnitude (taken as a proxy for the flux seen by the 2 arcsec 2dF spectroscopic fibres), the GAMA redshift success rate ($\texttt{nQ} \geq 3$) is essentially 100 per cent for $r_{\texttt{fibre}} < 19.5$, dropping to 98 per cent for $r_{\texttt{fibre}} = 20$ and then down to ∼50 per cent for $r_{\texttt{fibre}} = 22$ (Loveday et al. 2011). For the r-selected survey sample ($\texttt{SURVEY\_CLASS} \geq 6$), the net redshift success rate is 95.4 per cent (109 222/114 250).

Stellar mass estimates have been derived for all objects with a spectroscopic redshift $0 < z \leq 0.65$. For the purposes of this work, we will restrict ourselves to considering only those galaxies with $z > 0.002$ (to exclude stars), and those galaxies with $\texttt{nQ} \geq 3$ (to exclude potentially suspect redshift determinations). We quantify the sample completeness in terms of stellar mass, restframe colour and redshift in Section 3.5.

2.2 Broad-band spectral energy distributions (SEDs)

This work is based on version 6 of the GAMA master catalogue (internal designation `catgama_v6`), which contains *ugrizYJHK* photometry for galaxies in the GAMA regions. The photometry is based on SDSS (DR7) optical imaging, and UKIDSS LAS (DR4) NIR imaging. The SDSS data have been taken from the Data Archive Server (DAS[1]); the UKIDSS data have been taken from the WFCAM Science Archive (WSA,[2] Hambly et al. 2008).

In each case, the imaging data are publicly available in a fully reduced and calibrated form. The SDSS data reduction has been extensively described (see e.g. Strauss et al. 2002; Abazajian et al. 2009). The LAS data have been reduced using the WFCAM-specific pipeline developed and maintained by the Cambridge Astronomical Survey Unit (CASU).[3]

The GAMA photometric catalogue is constructed from an independent reanalysis of these imaging data. The data and the GAMA reanalysis of them are described fully by Hill et al. (2011) and Kelvin et al. (2011). We summarize the most salient aspects of the GAMA photometric pipeline below. As described in Hill et al. (2011), the data in each band are normalized and combined into three astrometrically matched gigapixel-scale mosaics (one for each of the G09, G12 and G15 fields), each with a scale of 0.4 arcsec pixel^{-1}. In the process of the mosaicking, individual frames are degraded to a common seeing of 2 arcsec full width at half-maximum (FWHM).

Photometry is done on these point spread function (PSF)-matched images using SExtractor (Bertin & Arnouts 1996) in dual image mode, using the r-band image as the detection image. For this work, we construct multi-colour SEDs using SExtractor's `auto` photometry. This is a flexible, elliptical aperture whose size is determined from the observed light distribution within a quasi-isophotal region (see Bertin & Arnouts 1996; Kron et al. 1980, for further explanation) of the r-band detection image. This provides seeing- and aperture-matched photometry in all bands.

In addition to the matched-aperture photometry, the GAMA catalogue also contains r-band Sérsic-fit structural parameters, including total magnitudes, effective radii and Sérsic indices (Kelvin et al. 2011). These values have been derived using GALFIT3 (Peng et al. 2002) applied to (undegraded) mosaics constructed in the same manner as those described above. These fits incorporate a model of the PSF for each image, and so should be understood to be seeing corrected. In estimating total magnitudes, the Sérsic models have been truncated at 10 R_e; this typically corresponds to a surface brightness of $\mu_r \sim 30$ mag arcsec^{-2}. Hill et al. (2011) present a series of detailed comparisons between the different GAMA and SDSS/UKIDDS photometric measures. Additional comparisons between the GAMA and SDSS optical photometry are presented in Appendix B. In this work, we use these r-band `sersic` magnitudes to estimate galaxies' total luminosities, since these measurements (attempt to) account for flux missed by the finite `auto` apertures.

For each galaxy, we construct multi-colour SEDs using the SExtractor `auto` aperture photometry. Formally, when fitting to these SEDs, we are deriving SP parameters integrated or averaged over the projected `auto` aperture. In order to get an estimate of a galaxy's total stellar mass, it is therefore necessary to scale the inferred mass up, so as to account for flux/mass lying beyond the (finite) `auto` aperture. We do this by simply scaling each of the `auto` fluxes by the amount required to match the r-band `auto` aperture flux to the `sersic` measure of total flux; i.e. using the scalar aperture correction factor $f_{\rm ap} = 10^{-0.4(r_{\texttt{auto}} - r_{\texttt{sersic}})}$.

Note that we elect not to use the NIR data to derive stellar mass estimates for the current generation of the GAMA stellar mass catalogue. Our reasons for this decision are the subject of Section 4.

[1] http://das.sdss.org/

[2] http://surveys.roe.ac.uk/wsa/

[3] Online documentation available via http://casu.ast.cam.ac.uk/surveys-projects/wfcam.

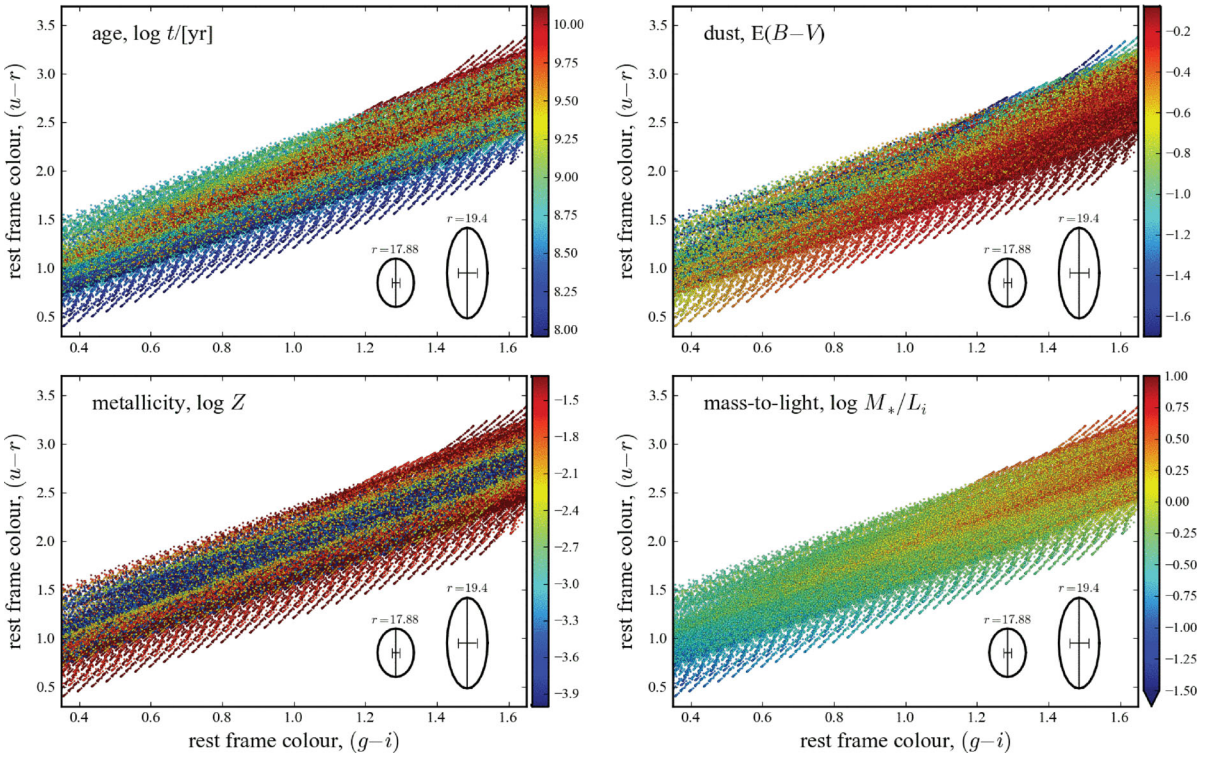

Figure 1. Illustrating the basic idea behind SPS modelling. In each panel, we plot the restframe $(u - r)$ and $(g - i)$ colours of the models in our library, colour-coded by an important basic property: CSP age, t, dust obscuration, E_{B-V}, stellar metallicity, Z, and mass-to-light ratio, M_*/L_i. In the simplest terms possible, given a galaxy's restframe (*ugri*) photometry, the process of SP parameter estimation can be thought of as just 'reading off' the value of each parameter. For comparison, the median 1σ uncertainty in the observer's frame *ugri* colours for GAMA galaxies at the SDSS and GAMA spectroscopic selection limits ($m_r = 17.88$ and 19.4, respectively) are shown in each panel. Note that as is standard practice, we impose an error floor of 0.05 mag in the photometry in each band; the ellipses show the effective uncertainties with the inclusion of this error floor. With the exception of the *u*-band, the catalogued error is almost always less than 0.05 mag; these errors are shown as the error bars within each ellipse. We are limited not by random noise, but by the systematic errors in the relative or cross-calibration of the photometry in the different bands. In each panel, areas where one colour dominates show where a given parameter can be well constrained using restframe *ugri* photometry. Conversely, where models with similar *ugri* colours have a wide range of parameter values, this parameter cannot be well constrained due to degeneracies among the CSP models. Thus, it can be seen that even though t, E_{B-V} and particularly Z are generally not well constrained from an optical SED, M_*/L can still be relatively robustly estimated.

3 STELLAR POPULATION SYNTHESIS MODELLING AND STELLAR MASS ESTIMATION

The essential idea behind SPS modelling is to determine the characteristics of the SPs that best reproduce the observed properties (in our case, the broad-band SED) of the galaxy in question. As an illustrative introduction to the problem, Fig. 1 shows the distribution of our SPS model templates in restframe $(u - r)$–$(g - i)$ colour–colour space. In each panel of this figure, we colour-code each model according to a different SP parameter.

Imagine for a moment that instead of using the observed *ugriz* SEDs, we were to first transform those SEDs into restframe *ugri* photometry, and then use this as the basis of the SPS fitting. In the simplest possible terms, the fitting procedure could then be thought of as 'reading off' the parameters of the model(s) found in the region of the *ugri* colour–colour space inhabited by the galaxy.

In this figure, regions that are dominated by a single colour show where a parameter can be tightly constrained on the basis of a (rest-frame) *ugri* SED.[4] Conversely, regions where the different colours are well mixed show where models with a wide range of parameter values provide equally good descriptions of a given *ugri* SED shape; that is, where there are strong degeneracies between model parameters.

In general terms, then, Fig. 1 demonstrates that it is difficult to derive strong constraints on t or Z; this is the well known age–metallicity degeneracy.[5] Even where such strong degeneracies exist, however, note that the value of M_*/L is considerably better constrained than any of the parameters that are used to define each model.

3.1 Synthetic stellar population models

The fiducial GAMA stellar mass estimates are based on the BC03 synthetic SP model library, which consists of spectra for single-aged or SSPs, parametrized by their age, t, and metallicity, Z; i.e. $f_{\rm SSP}(\lambda; t, Z)$. Given these SSP spectra and an assumed SFH, $\psi_*(t)$,

[4] When constructing each panel in Fig. 1, we have deliberately plotted the models in a random order, rather than, say, ranked by age or metallicity. This ensures that the mix of colour-coded points fairly represents the mix of model properties in any given region of colour–colour space.

[5] In principle, and to foreshadow the results shown in Section 5.1, these degeneracies can be broken by incorporating additional information. For example, if different models that have similar $(g - i)$ and $(u - r)$ colours have very different optical-minus-NIR colours, then the inclusion of NIR data can, at least in principle, lead to much tighter constraints on the model parameters.

spectra for CSPs can be constructed, as a linear combination of different simple SSP spectra, i.e.

$$f_{\rm CSP}(\lambda; Z, t, E_{B-V}) = k(\lambda; E_{B-V}) \int_{t'=0}^{t} {\rm d}t' \psi_*(t') \times f_{\rm SSP}(\lambda; Z, t'). \quad (1)$$

Here, $k(\lambda; E_{B-V})$ is a single-screen dust attenuation law, where the degree of attenuation is characterized by the selective extinction between the B- and V-bands, E_{B-V}. Note that this formalism works for any quantity that is additive; e.g. flux in a given band, stellar mass (including sub-luminous stars, and accounting for mass loss as a function of SSP age), the mass contained in stellar remnants (including white dwarfs, black holes), etc.

When using this equation to construct the CSP models that comprise our SPL, we make three simplifying assumptions. We consider only smooth, exponentially declining SFHs, which are parametrized by the e-folding time-scale, τ, i.e. $\psi_*(t) \propto {\rm e}^{-t/\tau}$.[6] We make the common assumption that each CSP has a single, uniform stellar metallicity, Z. We also make the (equally common) assumption that a single dust obscuration correction can be used for the entire CSP.

For our fiducial mass estimates, we use a Calzetti et al. (2000) dust attenuation 'law'. In this context, we highlight the work of Wijesinghe et al. (2011), who look at the consistency of different dust obscuration laws in the optical and ultraviolet. They conclude that the Fischera & Dopita (2005) dust curve is best able to describe the optical-to-ultraviolet SED shapes of GAMA galaxies. In the optical, the shapes of the Fischera & Dopita (2005) and Calzetti et al. (2000) curves are quite similar. Using the Fischera & Dopita (2005) curve does not significantly alter our results.

The models in our SPL are thus characterized by four key parameters: age, t; e-folding time, τ; metallicity, Z; and dust obscuration, E_{B-V}. In an attempt to cover the full range of possible SPs found in real galaxies, we construct a library of CSP model spectra spanning a semi-uniform grid in each parameter. The age grid spans the range $\log t/[{\rm yr}] = 8$–8.9 in steps of 0.1 dex, then from $\log t/[{\rm yr}] = 9$–10.10 in steps of 0.05 dex, and then with a final value of 10.13 ($\approx$13.4 Gyr). The grid of e-folding times spans the range $\log \tau/[{\rm yr}] = 7.5$–$8.9$ in steps of 0.2 dex, and then from $\log \tau/[{\rm yr}] = 9$–10 in steps of 0.1 dex. The dust grid covers the range $E_{B-V} = 0.0$–0.8 in steps of 0.02 mag. We use the native metallicity grid for the BC03 models: $Z = (0.0001, 0.0004, 0.004, 0.008, 0.02, 0.05)$. The fiducial model grid thus includes $34 \times 19 \times 43 \times 6 = 166\,668$ models for each of 66 redshifts between $z = 0.00$ and 0.65, for a total of just over 11 million individual sets of nine-band synthetic photometry.

3.2 SED fitting

Synthetic broad-band photometry is derived using the CSP spectra and a model for the total instrumental response for each of the *ugriz*- and *YJHK*-bands. The optical and NIR filter response functions are taken from Doi et al. (2010) and from Hewett et al. (2006), respectively. These curves account for atmospheric transmission (assuming an airmass of 1.3), filter transmission, mirror reflectance, and detector efficiency, all as a function of wavelength. For a given template spectrum $f_{\rm CSP}$, placed at redshift z, the template flux in the (observers' frame) X-band, $T_{\rm X}$, is then given by

$$T_{\rm X}({\rm CSP}; z) = (1+z) \frac{\int {\rm d}\lambda r_{\rm X}(\lambda) \lambda f_{\rm CSP}\left(\frac{\lambda}{1+z}\right)}{\int {\rm d}\lambda r_{\rm X}(\lambda) \lambda}. \quad (2)$$

Here, $r_{\rm X}$ is filter response function, and the prefactor of $(1 + z)$ accounts for the redshift stretching of the bandpass interval. Also note that the factor of λ in both integrals is required to account for the fact that broad-band detectors count *photons*, not *energy* (see e.g. Hogg et al. 2002; Brammer, van Dokkum & Coppi 2008): $T_{\rm X}$ thus has units of counts m^{-2} s^{-1}.

By construction, each of the template spectra in our library is normalized to a total, time-integrated SFH (cf. instantaneous mass) of 1 $M_\odot$ observed from a distance of 10 pc. A normalization factor, A_T, is thus required to scale the apparent flux of the base template to match the data, accounting for both the total stellar mass/luminosity and distance-dependent dimming. It is thus through determining the value of A_T that we arrive at our estimate for M_* (for a specific trial template, T, and given the observed photometry, F); viz.:

$$M_*(T; F) = A_T M_{*,{\rm T}}(t) \left(\frac{D_{\rm L}(z_{\rm dist})}{[10\ {\rm pc}]} \right)^2. \quad (3)$$

Here, $M_{*,{\rm T}}(t)$ is the (age-dependent) stellar mass of the template T (including the mass locked up in stellar remnants, but not including gas recycled back into the ISM), and $D_{\rm L}(z_{\rm dist})$ is the luminosity distance, computed using the flow-corrected redshift, $z_{\rm dist}$.

Given the (heliocentric) redshift of a particular galaxy, we compare the observed fluxes, F, to the synthetic fluxes for the model templates in our SPL, T, placed at the same (heliocentric) redshift. The goodness of fit for any particular template spectrum is simply given by

$$\chi^2_T = \sum_{\rm X} \left(\frac{A_T T_{\rm X} - F_{\rm X}}{\Delta F_{\rm X}} \right)^2, \quad (4)$$

where $\Delta F_{\rm X}$ is the uncertainty associated with the observed X-band flux, $F_{\rm X}$.

Following standard practice, we impose an error floor in all bands by adding 0.05 mag in quadrature to the uncertainties found in the photometric catalogue. This is intended to allow for differential systematic errors in the photometry between the different bands (e.g. photometric calibration, PSF- and aperture-matching, etc.) as well as minor mismatches between the SPs of real galaxies and those in our SPL.

It is worth stressing that in almost all cases, the formal photometric uncertainties found in the photometric catalogues are considerably less than 0.05 mag (see Fig. 1). This implies that, even with the current SDSS and UKIDSS imaging, we are *not* limited by random noise, but by systematic errors and uncertainties in the relative- or cross-calibration of the different photometric bands. This imposed error floor is thus the single most significant factor in limiting the formal accuracy of our stellar mass estimates.

3.3 Bayesian parameter estimation

For a given F and T, we fix the value of the normalization factor A_T that appears in equation (4) by minimizing χ^2_T. This can be done analytically. We contrast this approach with, for example, simply scaling the model SED to match the observed flux in a particular band (e.g. Brinchmann & Ellis 2000; Kauffmann et al. 2003a). Our

[6] Whereas the integral in equation (1) is continuous in time, each set of the SSP libraries that we consider contain SP parameters for a set of discrete ages, t_i. In practice, we compute the integral in equation (1) numerically, using a trapezoidal integration scheme to determine the number of stars formed in the time interval Δt_i associated with the time t_i. This effectively assumes that the spectral evolution at fixed λ and Z is approximately linear between values of t_i. Note that this is something that is not optimally implemented in the standard GALAXEV package described by BC03.

approach has the advantage that the overall normalization is set with the combined signal-to-noise ratio of all bands.[7]

With the value of A_T fixed, the (minimized) value of χ^2_T can be used to associate a probability to every object–model comparison,[8] viz., the probability of measuring the observed fluxes, *assuming* that a given model provides the 'true' description of a galaxy's SP, $\Pr(F|T) \propto \mathrm{e}^{-\chi^2_T}$. But this is not (necessarily) what we are interested in – rather, we want to find the probability that a particular template provides an accurate description of the galaxy *given the observed SED*; i.e. $\Pr(T|F)$. These two probabilities are related using Bayes' theorem, viz. $\Pr(T|F) = \Pr(T) \times \Pr(F|T)$, where $\Pr(T)$ is the a priori probability of finding a real galaxy with the same SP as the template T.

The Bayesian formulation thus requires us to explicitly specify an a priori probability for each CSP. But it is important to realize that *all fitting algorithms include priors*; the difference with Bayesian statistics is only that this prior is made *explicit*. For example, if we were to simply use the best-fitting model from our library, the parameter-space distribution of SPL templates represents an *implicit* prior assumption on the distribution of SP parameters. In the absence of clearly better alternatives, we make the simplest possible assumptions: namely, we assume a flat distribution of models in all of t, τ, $\log Z$ and E_{B-V}. That is, we have chosen not to privilege or penalize any particular set of SP parameter values. The only exception to this rule is that, as is typical, we exclude solutions with formation times less than 0.5 Gyr after the big bang.

The power of the Bayesian approach is that it provides the means to construct the posterior probability density function (PDF) for any quantity, Q, given the observations; i.e. $\mathrm{P}(Q = Q_T|F)$, where Q_T is the value of Q associated with the specific template T. The *most likely* value of Q is then given by a probability-weighted integral over the full range of possibilities;[9] i.e.

$$\langle Q \rangle = \int \mathrm{d}T\, Q(T) \Pr(T|F) = \int \mathrm{d}T\, Q(T) \Pr(T) \exp\left[-\chi^2_T(F)\right]. \quad (5)$$

In the parlance of Bayesian statistics, this is referred to as 'marginalizing over the posterior probability distribution for Q'.[10] Similarly, it is possible to quantify the uncertainty associated with $\langle Q \rangle$ as:

$$\Delta Q = \sqrt{\langle Q^2 \rangle - \langle Q \rangle^2}. \quad (6)$$

3.4 The importance of being Bayesian

Before moving on, in this section we present a selection of diagnostic plots. Our motivation for presenting these plots is twofold. First, the figures presented in this section illustrate the distribution of derived parameter values for all $0.02 < z < 0.65$ GAMA galaxies with `nQ` ≥ 3 and `SURVEY_CLASS` ≥ 4 (defined in Section 2.1). The different panels in each figure show the 2D-projected logarithmic data density in small cells; the same colour-scale is used for all panels in Figs 2–5. Note that by showing the logarithmic data density, we are visually emphasizing the more sparsely populated regions of parameter space.

Secondly, we use these figures to illustrate the differences between SP parameter estimates based on Bayesian statistics, and those derived using more traditional, frequentist statistics. As described above, Bayesian statistics focus on the most likely state of affairs given the observation, $P(Q|F)$. Bayesian estimators can be, both in principle and in practice, significantly different from frequentist estimators, which set out to identify the set of model parameters that is most easily able to explain the observations; i.e. to maximize $P(F|Q)$. To make plain the differences between these two parameter estimates, we will compare the Bayesian 'most likely' estimator as defined by equation (5) to a more traditional 'best-fitting' value derived via maximum likelihood. Note that when deriving the frequentist 'best-fitting' values, we have applied our priors through weighting of the value of χ^2 for each template; that is, the 'best-fitting' value is that associated with the template T which has the highest value of $\log \mathcal{L}(F|T) = \log \Pr(T) - \chi^2_T(F)$.

The distribution of these 'best-fitting' SP parameters is shown in Fig. 2, as a function of stellar mass, M_*, and SP age, t. It is immediately obvious from this figure how our use of a semi-regular grid of SP parameters to construct the SPL leads directly to strong quantization in the 'best-fitting' values of t, τ, Z and E_{B-V}. What is more worrying, however, is that there is also a mild discretization in the inferred values of M_*/L, seen in the bottom-left panel of Fig. 2 as a subtle striping. This is despite the fact that the SPL samples a much more nearly continuous range of M_*/Ls than ts, τs or Zs.

To explain the origin of this effect, let us return to Fig. 1. For a given galaxy, there will be a large number of templates that will be consistent with the observed *ugriz* photometry. To the extent that a small perturbation in the observed photometry can have a large impact on the inferred SP parameter values, there thus is a degree of randomness in the selection of the 'best-fitting' solution from within the error ellipse. This means that values of M_*/L, $(g-i)$, etc. that are 'over-represented' within the SPL will be more commonly selected as 'best fits'. Note that this problem of discretization in M_*/L_i is therefore *not* a sign of insufficiently fine sampling of the SPL parameter space: this problem arises where there very many, not very few, templates that are consistent with a given galaxy's observed colours.

Fig. 2 should be compared to Fig. 3, in which we show the distribution of the Bayesian 'most likely' parameter values. Consider again Fig. 1: whereas the 'best-fitting' value is the one nearest to the centre of the error ellipse for any given galaxy, the Bayesian value is found by taking a probability-weighted mean of all values around the observed data point. The process of Bayesian marginalization can thus be thought of as using the SPL templates to discretely

[7] In connection with the results of Section 4, this approach is also less sensitive to systematic offsets between the observed and fit photometry, including absolute and relative calibration errors in any given band, which would produce a bias in the total inferred luminosity in a given band or bands.

[8] This simply assumes that the measurement uncertainties in the SED ΔF_X are all Gaussian and independent. Note that this does not necessarily gel well with the imposition of an error floor intended to allow for systematics.

[9] Here, the integral should be understood to be across the full parameter space spanned by our template library, and the assumption that our template library covers the full range of possibilities leads to the integral constraint $\int \mathrm{d}T\ \Pr(T|F) = 1$.

[10] Note that in practice we do not actually integrate over values of the normalization parameter, A_T, that appears in equation (4). Instead, for a given T and F, we fix the value of A_T via χ^2 minimization. But because $\chi^2(A_T)$ is symmetric about the best-fitting value of A_T, this will only cause problems for galaxies with very low total signal-to-noise ratio across all bands, where values of $A_T < 0$ may have some formal significance. Since essentially all the objects in the GAMA catalogue have signal-to-noise ratio of roughly 30 or more in all of the *gri*-bands, we consider that this is unlikely to be an important issue.

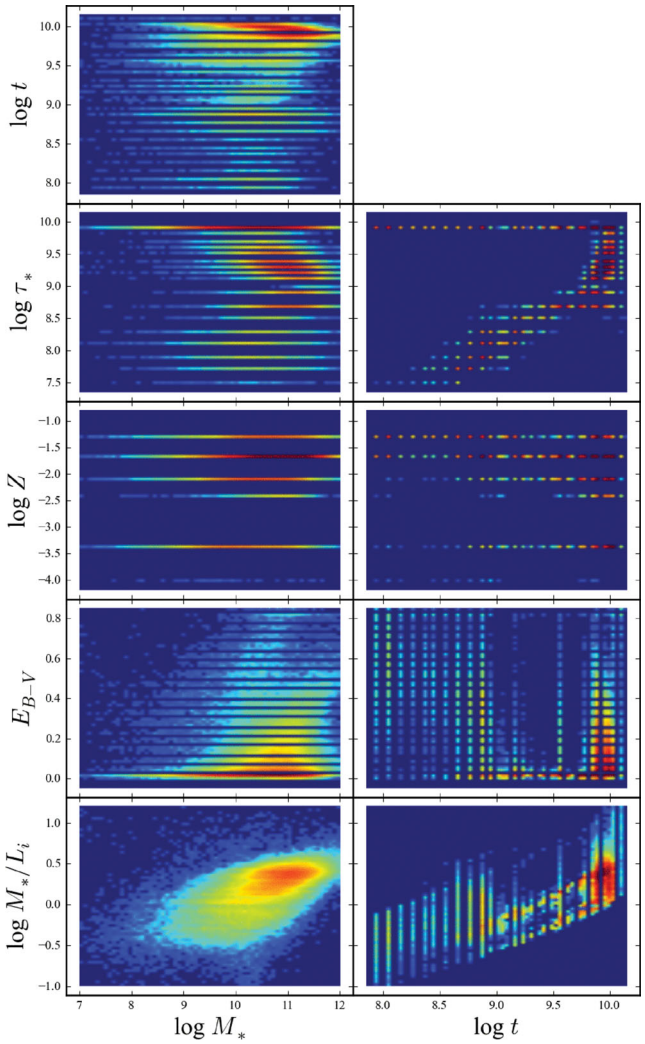

Figure 2. Why 'best fit' is not the best parameter estimator. This figure shows the distribution of parameter values corresponding to the single 'best-fitting' (i.e. maximum likelihood) template. The distributions shown in this figure should be compared to the distributions of Bayesian estimators in Fig. 3. It is immediately obvious how the use of a semi-regular grid of SP parameter values within our SPL produces strong discretization in t, τ, Z, and E_{B-V}. In the lower-left panel, however, it can be seen that there is some quantization in M_*/L, even though the distribution of M_*/Ls in the SPL is more nearly continuous. As described in Section 3.4, this form of discretization arises where there are strong degeneracies in the SPS fit, which cannot be properly accounted for using a frequentist 'best-fitting' approach.

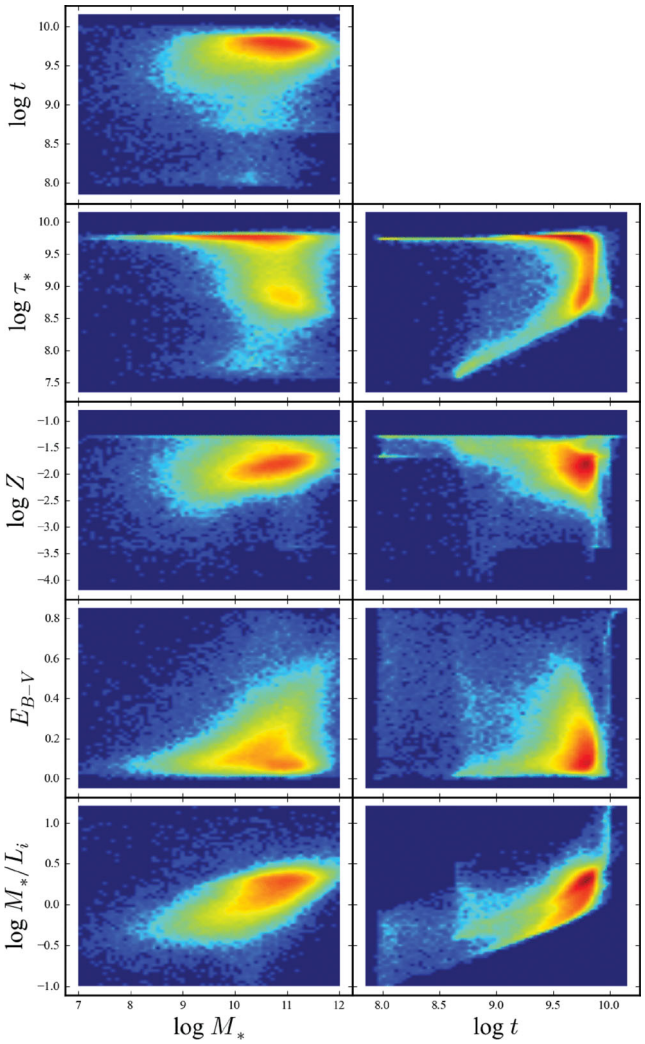

Figure 3. Illustrating the inferred distribution of SP parameters for GAMA galaxies. In this figure, we show the interrelationships between several important SP parameters for GAMA galaxies. Note that the SPL covers the full range of t, τ and E_{B-V} shown. The observed relations between these parameters show that information about the process of galaxy formation and evolution can be extracted from galaxies' SEDs. From an algorithmic point of view, the most important point to take from this plot is that by using a Bayesian approach, we are able for the most part to avoid 'discretization' errors (i.e. preferred parameter values) associated with the use of a discrete grid of parameter values (cf. Fig. 2). Further, note that particularly for t, τ, and Z, these distributions are qualitatively different from those in Fig. 2.

sample a continuous parameter distribution, after effectively smoothing on a scale commensurate with the observational uncertainties. This largely mitigates the discretization in t, τ and Z – as well as in M_*/L – that comes from using a fixed grid of parameter values to define the SPL.

That said, this only works where several different parameter combinations provide an acceptable description of the data. If one particular template is strongly preferred – if the observational uncertainties in a galaxy's SED are comparable to or less than the differences between the SEDs of different templates – then our approach reverts to a 'best fit', and we will again suffer from artificial quantization in the fit parameters. For the same reasons, the formal uncertainty on the SP parameters will be artificially small in this case. Note that, somewhat perversely, this problem will become *worse* with increasing signal-to-noise ratio. (See also Gallazzi & Bell 2009, but note, too, that the inclusion of a moderate 'systematic' uncertainty in the observed SEDs works to protect against such 'single template' fits.) In this sense, and in contrast to the quantization in the 'best-fitting' values discussed above, quantization in the Bayesian 'most likely' values *does* indicate inadequately fine sampling of the SPL parameter space. We have chosen our parameter grids with this limitation in mind; in particular, we have found that a rather fine sampling in the E_{B-V} dimension is required to avoid strong quantization.

Although our SPL templates span a semi-regular grid in each of t, τ, Z and E_{B-V}, the observed distribution in these parameters is anything but uniform. There is nothing in the calculation to preclude solutions with, for example, young ages and low metallicities.

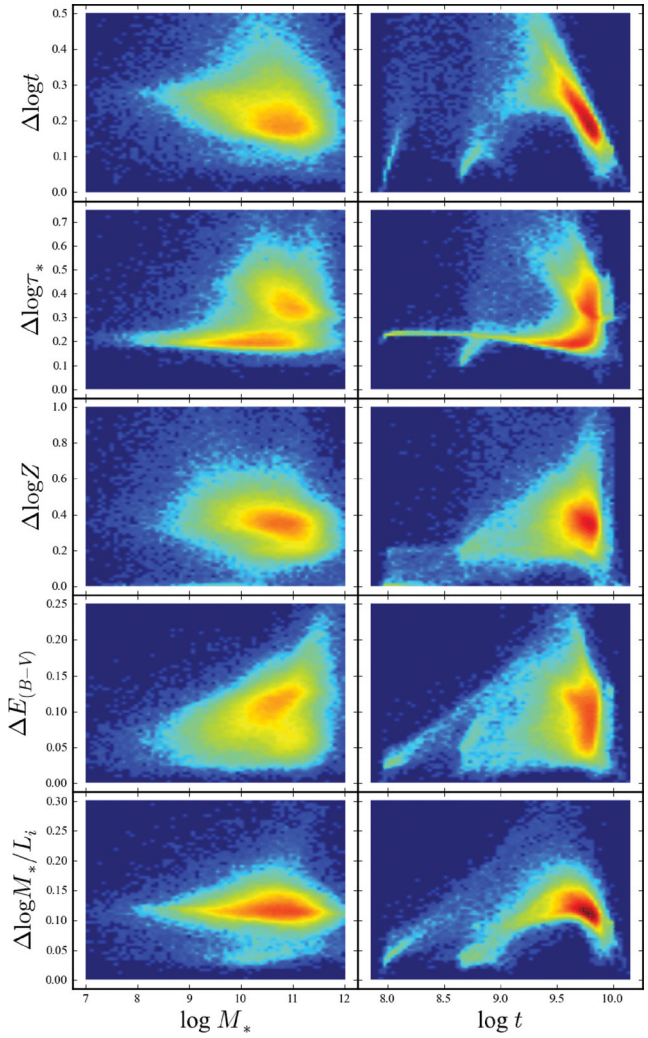

Figure 4. Illustrating the distribution of parameter uncertainties. In this figure, we show the formal uncertainties for several important parameters. The structure that is apparent in the different panels of this plot shows that our ability to constrain t, τ, and Z is different for different SPs. The crucial point to be made from this figure, however, is that the formal uncertainty in M_*/L_i is ≈0.1 dex for the vast majority of galaxies, with essentially no dependence on the uncertainties in other parameter values.

The fact that these regions of parameter space are sparsely or unpopulated shows that there are few or no galaxies with optical SEDs that are consistent with these properties. Fig. 3 thus illustrates the mundane or crucial (depending on one's perspective) fact that the derived SP parameters do indeed encode information about the formation and evolution of galaxies. It is particularly striking that there appears to be a rather tight and 'bimodal' relation between t and τ: there is a population of galaxies that are best fit by very long and nearly continuous SFHs ($\tau \approx 10$ Gyr), and another with $t/\tau \approx 3$–10. Curiously, there are virtually no galaxies inferred to have $t < \tau$.

The inferred distribution of parameter values is significant in terms of our assumed priors: it is clear that the derived parameter distributions do not follow our assumed priors (see also Fig. 12). But this is not to say that the precise values are not more subtly affected by our particular choice of priors. In particular, the local slope of the priors on the scale of the formally derived uncertainties might act to skew the posterior PDF (see also Appendix A). In principle, it would be possible to use the observed parameter distributions to derive new, astrophysically motivated priors. Then, if this were to significantly alter the observed parameter distribution, the process could be iterated until convergence. Such an exercise is beyond the scope of this work.

Next, in Fig. 4, we show the distribution of inferred uncertainties in each of the parameters shown in Fig. 3. As in Fig. 3, there is some structure apparent in these distributions: the uncertainties in some derived properties are different for galaxies with different kinds of SPs. As a simple example, galaxies with $t \gg \tau$ have considerably larger uncertainties in τ, as information about the SFH is washed out with the deaths of shorter-lived stars. In connection to the discretization problem, the very young galaxies (seen in Fig. 3 to suffer from discretization in the values of Z) also have low formal values for $\Delta\log Z$ and/or $\Delta\log t$. But it is worth noting that in comparison to the uncertainties in other SP parameters, $\Delta\log M_*/L_i$ is more nearly constant across the population (this is perhaps more clearly apparent in Fig. 5, described immediately below).

Our last task for this section is to directly compare the frequentist 'best-fitting' and Bayesian 'most likely' SP values; this comparison is shown in Fig. 5. In each panel of this figure, the 'Δ' plotted on the y-axis should be understood as being the 'best-fitting' minus 'most likely' value; these are plotted as a function of the Bayesian estimator. Within each panel, the dashed white curves show the median $\pm 3\sigma$ uncertainty in the y-axis quantity, derived in the Bayesian way, and computed in narrow bins of the x-axis quantity. These curves can thus be taken to indicate the formal consistency between the best-fitting and most likely parameter values.

In practice, there is an appreciable systematic difference between the frequentist and Bayesian parameter estimates. In general, we find that traditional, frequentist estimates are slightly older (by ≈0.14 dex), less dusty (by ≈0.07 mag) and more massive (by 0.09 dex) than the Bayesian values. In comparison to the formal uncertainties, these systematic differences are at the 0.5–0.7σ level; this is despite the fact that the 'best-fitting' value is within 1.5σ of the 'most likely' value for 99 per cent of objects. Again, we stress that, formally, the Bayesian estimator is the correct value to use.

As a final aside for this section, we note that the importance of Bayesian analysis has been recognized in the context of photometric redshift evaluation (a problem which is very closely linked to SPS fitting) by a number of authors, including Benitez (2000) and Brammer et al. (2008). While most of the SPS fitting results for SDSS (e.g. Kauffmann et al. 2003b; Brinchmann et al. 2004; Gallazzi et al. 2005) have been based on a Bayesian approach, it is still common practice to derive SPS parameter estimates using simple χ^2 minimization (Walcher et al. 2011, and references therein). This is particularly true for high-redshift studies (but see Pozetti et al. 2007; Walcher et al. 2008).

3.5 Detection/selection limits and $1/V_{\rm max}$ corrections

GAMA is a flux-limited survey. For a number of science applications – most obviously measurement of the mass or luminosity functions – it is important to know the redshift range over which an individual galaxy would be selected as a spectroscopic target. To this end, we have used the SP fits described above to determine the maximum redshift, $z_{\rm max}$, at which each galaxy in the GAMA catalogue would satisfy the main GAMA target selection criterion of $r_{\tt petro} < 19.4$, or, for the G12 field, $r_{\tt petro} < 19.8$. (Recall that the target selection is done on the basis of the SDSS, rather than the GAMA, `petro` magnitude.)

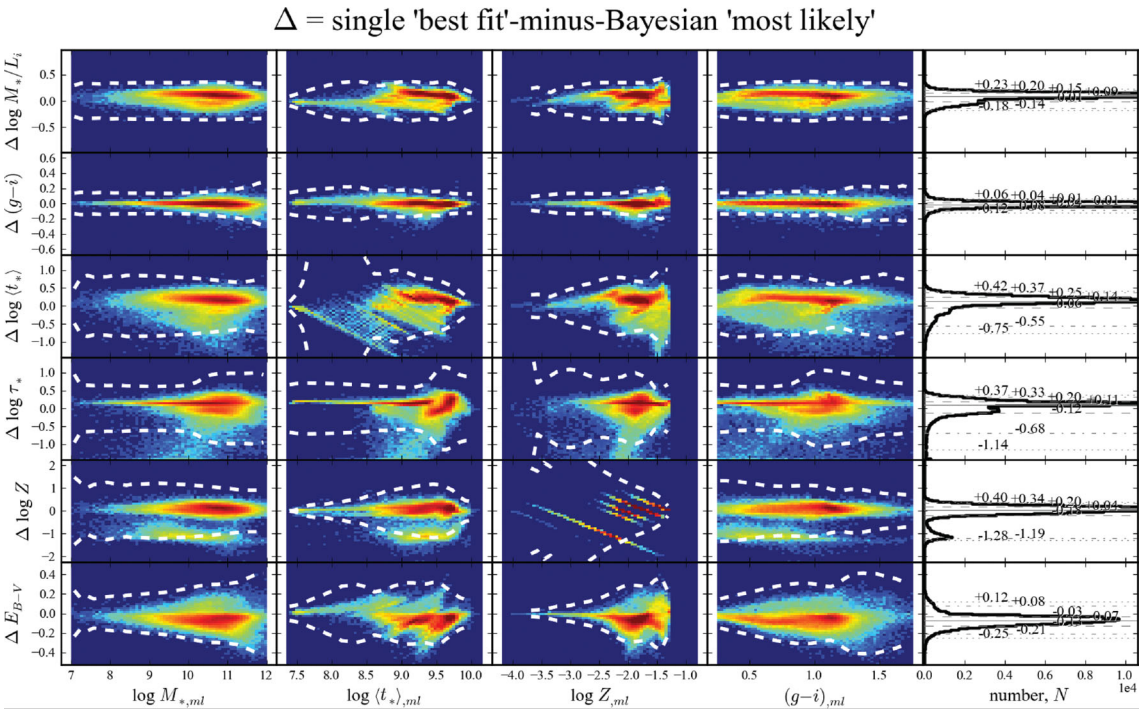

Figure 5. Using a frequentist 'best-fitting' estimator leads to significant biases in the inferred SP parameter values. In this figure, we show the difference between the 'best-fitting' (i.e. maximum-likelihood) value, and the Bayesian 'most likely' value of a number of key parameters. The 'Δ' plotted on the *y*-axis should be understood as being the 'best-fitting' minus 'most likely' value. Strong quantization in the 'best-fitting' values can be clearly seen for $\langle t_* \rangle$ and particularly Z. Further, in the right-hand panels of this figure, we look at the random and systematic differences between these two parameter estimates; the numbers in each panel show the equivalent of the 0, ±1, ±2 and ±3σ percentiles for each distribution. In particular, note that the 'best-fitting' (which again we stress is not the correct estimator to use) value of M_*/L is systematically higher than the 'most likely' value by 0.09 dex.

This has been done for each galaxy using the best-fitting template spectrum.[11] Knowing the best-fitting template, including the normalization factor, A_T, we consider how the observers' frame *r*-band flux of the template declines with redshift. Knowing that galaxy's observed $r_{\rm petro}$, it is then straightforward to determine the redshift at which the observers' frame *r*-band flux drops to the appropriate limiting magnitude. The only complication here is accounting for both the cosmological redshift and the Doppler redshift due to peculiar velocities. This is done by recognizing that $(1 + z_{\rm helio}) = (1 + z_{\rm dist})(1 + z_{\rm pec})$; the values of $z_{\rm max}$ should be taken as pertaining to $z_{\rm dist}$.

In Fig. 6, we use the value of $z_{\rm max}$, so derived, to show GAMA's stellar mass completeness limit expressed as a function of redshift and restframe colour. This figure shows the twofold power of GAMA in relation to SDSS. First, for dwarf galaxies, GAMA is ≈95 per cent complete for $M_* \approx 10^8$ M$_\odot$ and $z \approx 0.05$; at these masses, SDSS completeness is $\lesssim$80 per cent even for $z < 0.02$. GAMA thus provides the first census of $10^{7.5} < M_* < 10^{8.5}$ M$_\odot$ galaxies. Further, for massive galaxies, GAMA probes considerably higher redshifts: for $M_* \sim 10^{10.5}$ (10^{11}) M$_\odot$, where SDSS is limited to $z \lesssim 0.1$ (0.15), GAMA can probe out to $z \approx 0.25$ (0.3). Said another way, GAMA probes roughly twice the range of lookback times of SDSS. GAMA thus opens a new window on the recent evolution of the massive galaxy population.

In the right-hand panel of Fig. 6, we show these same results in a complementary way. The solid lines in this figure show the mean value of $z_{\rm max}$ as a function of M_* and restframe $(g - i)$. These values are for the main $r_{\rm petro} < 19.4$ selection only; for the G12 field, these limits should be shifted down in mass by 0.16 dex.

In this panel, for comparison, we also show the incompleteness-corrected bivariate colour-mass distribution for $z < 0.12$ galaxies, i.e. individual galaxies have been weighted by $1/V_{\rm max}$, where $V_{\rm max}$ is the survey volume implied by $z_{\rm max}$. Note that in the construction of this plot, we have only included galaxies with a relative weight <30 (i.e. $z_{\rm max} > 0.0375$); in effect, this means that we have not fully accounted for incompleteness for $M_* \lesssim 10^8$ M$_\odot$. Again, we see that GAMA probes the bulk of the massive galaxy population ($M_* \gtrsim 10^{10.5}$ M$_\odot$) out to $z \approx 0.25$.

Before moving on, we make two further observations. First, it is clear that the red sequence galaxy population extends well below the 'threshold mass' of $10^{10.5}$ M$_\odot$ suggested by Kauffmann et al. (2003b). Secondly, it appears that we are seeing the low-mass end of the red sequence population: the apparent dearth of galaxies with $(g - i) \gtrsim 0.8$ and $10^{8.5} \lesssim M_*/{\rm M}_\odot \lesssim 9.5$ is not a product of incompleteness. We will investigate these results further in a future work.

4 HOW MUCH DOES NIR DATA HELP (OR HURT)?

Conventional wisdom says that using NIR data leads to a better estimate of stellar mass. The principal justification for this belief is that,

[11] We have argued in Section 3.3 that the best-fitting template is not appropriate as a basis for deriving SP parameters. For the same reasons, formally, we should also marginalize over the posterior probability distribution for $z_{\rm max}(T)$. We have checked, and the value of $z_{\rm max}$ derived from the best-fitting template typically matches the Bayesian value to within $\Delta z_{\rm max} \sim 0.001$. Given this, and the fact that using the best-fitting value is vastly computationally simpler, we have opted to use the best-fitting template.

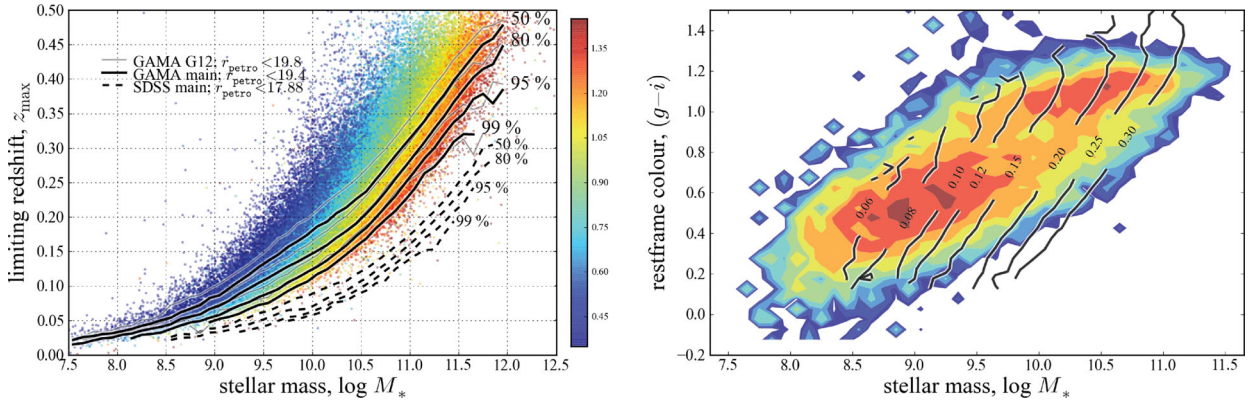

Figure 6. The GAMA stellar mass completeness limits as a function of redshift and restframe colour. Both panels of this plot use the derived values of z_{max} (i.e. the maximum redshift at which any individual galaxy would satisfy the *r*-band selection limit) to show the redshift-dependent GAMA completeness limit as a function of stellar mass and restframe colour. In the left-hand panel, we show the stellar mass for which GAMA is 50/80/95/99 per cent complete, computed in narrow bins of z_{max}. The heavier solid lines show the completeness for the main $r_{petro} < 19.4$ GAMA selection limit; the lighter solid lines show that for the deeper $r_{petro} < 19.8$ limit for the G12 field; the dashed lines show the completeness for the SDSS $r_{petro} < 17.88$ main galaxy sample selection limit. In this panel, individual plots are colour-coded according to their restframe $(g - i)$ colour; only galaxies from the main $r_{petro} < 19.4$ sample are shown. In the right-hand panel, the black contours show the mean value of z_{max}, again for the main $r_{petro} < 19.4$ sample, projected on to the colour–stellar mass diagram. For comparison, the filled, coloured contours in this panel show the incompleteness-corrected bivariate colour–stellar mass distribution of $z < 0.12$ galaxies; these contours are logarithmically spaced by factors of 2. In constructing this plot, individual galaxies have been weighted by $w = V(z = 0.12)/V(z_{max})$. We have only counted galaxies with a relative weighting $w < 30$. In effect, this means that we have not fully corrected for incompleteness for $z_{max} < 0.04$ or $M_* \lesssim 10^{8.5}$ $M_\odot$.

in comparison to optical wavelengths, and all else being equal, NIR luminosities (1) vary less with time, (2) depend less on the precise SFH and (3) are less affected by dust extinction/obscuration. Further, whereas old SPs can have very similar optical SED shapes to younger and dustier ones (see Fig. 1), the optical–NIR SED shapes of these two populations are rather different. The inclusion of NIR data can thus break the degeneracy between these two qualitatively different situations, and so provide tighter constraints on each of age, dust and metallicity – and hence, it is argued, a better estimate of M_*/L.

There are, however, several reasons to be suspicious of this belief. First, while stellar evolution models have been well tested in the optical regime, there is still some controversy over their applicability in the NIR. This has been most widely studied and discussed recently in connection with TP-AGBs stars in the models of BC03 and M05 (e.g. Maraston et al. 2006; Bruzual 2007; Kriek et al. 2010). The different models have been shown to yield stellar mass estimates that vary by as much as ∼0.15 dex for some individual galaxies (e.g. Kannappan & Gawiser 2007; Muzzin et al. 2009; Wuyts et al. 2009), but only if restframe NIR data are used in the fits.

Separately from the question as to the accuracy of SP models in the NIR, there are a number of empirical arguments suggesting that optical data alone can be used to obtain a robust and reliable stellar mass estimate. A number of authors have found that there is a remarkably tight relation between optical colour and stellar mass-to-light ratio (Bell & de Jong 2001; Bell et al. 2003; Zibetti, Charlot & Rix 2009; Taylor et al. 2010a). As described in Section 1.2, Gallazzi & Bell (2009) have argued that a stellar mass estimate based on a single colour is nearly as reliable and robust as one based on a full optical-to-NIR SED fit, or even one based on spectral diagnostics. Further, using their NMF-based KCORRECT algorithm that eliminates the need to assume parametric SFHs, Blanton & Roweis (2007) have shown that they are able to use optical SEDs to *predict* galaxies' NIR fluxes. Each of these results implies that the NIR SED does not, in practice, contain qualitatively 'new' information not found in the optical.

With this as background, our goal in this section is to examine how the inclusion of NIR data affects our stellar mass estimates. We will take an empirical approach to the problem, looking at how both the quality of the fits and the quantitative results themselves depend on the models and photometric bands used. We will argue that, at least at the present time, the NIR data cannot be satisfactorily incorporated into our SPS fitting. We very briefly explore the possible causes of our problems in dealing with the NIR SEDs in Section 4.4. In the next section, we will then look at whether and how our decision to ignore the NIR data affects the quality of our stellar mass and SP parameter estimates.

4.1 How well do the models describe the optical-to-NIR SEDs of GAMA galaxies?

In Fig. 7, we show the residuals from the SED fits as a function of restframe wavelength, i.e. $m_{X,fit} - m_{X,obs}$ as a function of $\lambda_X/(1 + z)$.[12] Fig. 7 should be compared to Fig. A1 in Appendix A. This Appendix describes how we have applied our SPS fitting algorithm to mock galaxy photometry, which we have constructed from the fits to the actual *ugriz* SEDs of GAMA galaxies. In this way, as in Gallazzi & Bell (2009), we have tested our ability to fit galaxy SEDs in the case that the SPL provides perfect descriptions of the SPs of 'real' galaxies, and that the data are perfectly calibrated (i.e. no systematics in the photometric cross-calibration). Inasmuch as they can inform our expectations for the real data, the results of

[12] The values for the 'fit' photometry are obtained in the same way as the other SP parameters; viz., via Bayesian marginalization over the PDF, à la equation (5). They should thus be thought of as estimates of the most likely value of the 'true' observers' frame photometry, given the overall SED shape.

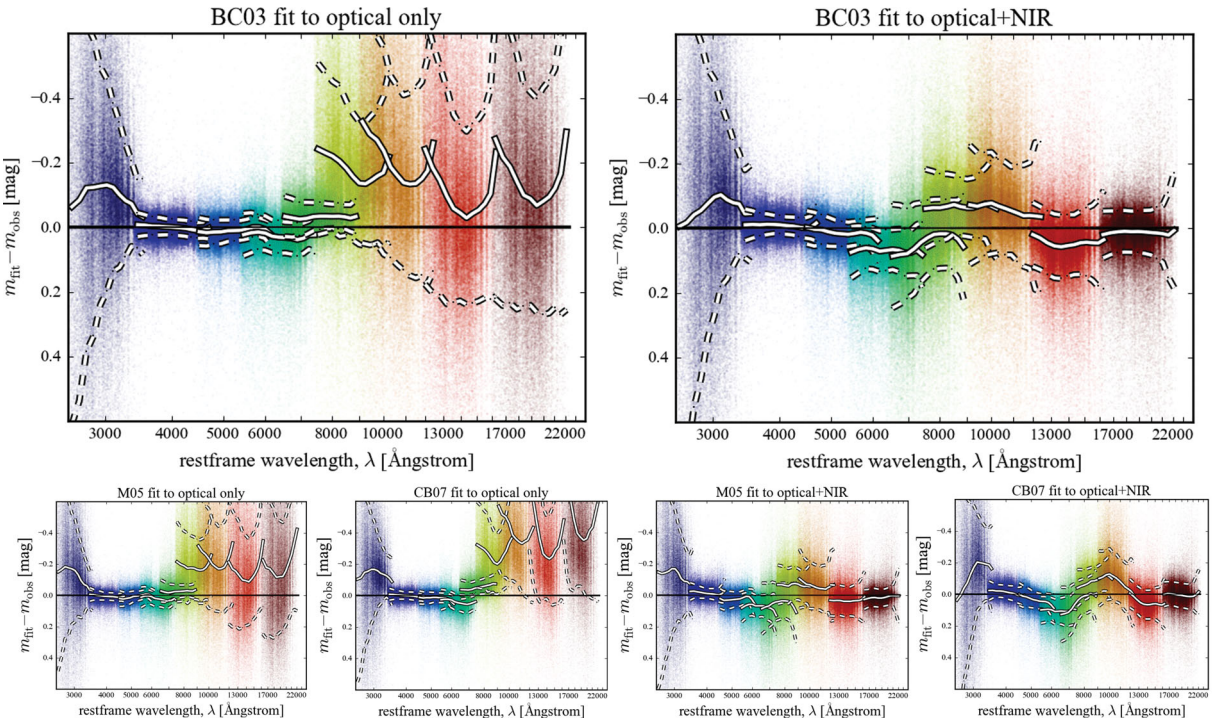

Figure 7. Illustrating how well the models describe the observed photometry of real galaxies. Each panel of this figure shows the residuals when fitting to either the optical *ugriz* (left panels) or the full *ugrizYJHK* (right-hand panels) SEDs. The main upper panels are for fits based on the BC03 stellar evolution models; the lower panels show the same using the M05 or CB07 models. Within each panel, the different colours refer to the different observed bands. For each band the white lines show the median (solid lines) and 16/84 percentile (dashed lines) residual in each band as a function of restframe wavelength or, equivalently, redshift. This figure should be compared to Fig. A1. From the left-hand panels, it is clear that all three of these SPS models provide an acceptable description of the optical SEDs, with relatively small residuals as a function of restframe wavelength. That said, these optical-only fits overpredict the NIR fluxes by $\sim$0.2 mag. In the right-hand panels, it can be seen that including the NIR data significantly degrades the quality of the optical fits, particularly in the *i*- and *z*-bands. Each of the three sets of models show qualitatively and quantitatively similar residuals: while each set of models yield similarly good fits to the optical data alone, none of these models provides a good description of the optical-to-NIR SEDs of GAMA galaxies. Based on our experiences with mock galaxy photometry in Appendix A, these results strongly suggest inconsistencies between the observed optical-minus-NIR colours of real galaxies and those contained within our SPL.

these numerical experiments, shown in Fig. A1, can help interpret the offsets seen in Fig. 7.

In Fig. 7, as in Fig. A1, the left-hand panels show the residuals when only the optical data are used for the fit. The NIR points in these panels are thus *predictions* for the observers' frame NIR photometry derived from the optical SED. The right-hand panels of both Figs 7 and A1 show the residuals for fits to the full nine-band optical-to-NIR SED. In Fig. 7, we show the residuals when using several different sets of SSP models to construct our SPL. In this figure, the larger upper panels are for the fits based on the BC03 SSP models; the panels below show the same using the SSP models of M05 and CB07 for comparison.

Looking first at the left-hand panels of Fig. 7, we see that our SPS fits provide a reasonably good description of the observed *ugriz* SEDs of real GAMA galaxies. The fit residuals are qualitatively and quantitatively similar when using each of the three different SSP models to construct the SPL. The median offset in each of the (*ugriz*) bands is $\approx (-0.10, -0.00, +0.01, +0.02, -0.03)$ mag. In terms of the formal uncertainties from the fits, the median offsets are at the level of $\approx (-0.3, -0.0, +0.2, +0.5, -0.5)\sigma$. The systematic biases in the fit photometry are thus weakly significant, but, at least for the *griz*-bands, well within the imposed error floor of 0.05 mag.

How does this compare to what is seen for the mocks in Figs A1? We find qualitatively similar offsets when fitting to the mock *ugriz* photometry. More specifically, we see a similar 'curvature' in the residuals, with slight excesses in the fit values for the *u*- and *z*-band photometry, and the *gri*-band photometry being very slightly too faint. It is true that, quantitatively, the offsets seen in Fig. 7 are about twice as large as we might expect based on our numerical experiments ($\lesssim 0.5\sigma$ for the real data, as opposed to $\lesssim 0.2\sigma$ for the mocks). But even so, the fact that we see similar residuals when fitting to the mocks shows that such residuals are to be expected, even in the ideal case where both the SPL and photometry are perfect. We do not, therefore, consider the mild systematic offsets between the fit and observed photometry as evidence for major problems in the *ugriz* fits.

Unlike Blanton & Roweis (2007), we seem unable to use the optical SEDs to satisfactorily predict NIR photometry. The fits to the *ugriz* data predict *YJHK* photometry that is considerably brighter (by up to $\sim$0.2 mag) than what is observed. The systematic differences between the predicted and observed fluxes for the BC03 models are -3.3σ -2.8σ, -1.6σ and -2.5σ in *YJHK*, respectively. For the M05 models, the residuals are slightly larger (-3.3σ, -3.0σ, -2.3σ and -2.8σ), and larger again for the CB07 models (-4.7σ, -5.6σ, -6.0σ and -8.2σ).

The fits to the mock galaxies' optical SEDs also overpredict the 'true' NIR fluxes, but, as can be seen in Fig. A1, in a qualitatively different way to what we see for real galaxies. In the case of the mock galaxies, the offset between the predicted and actual NIR fluxes is a much smoother function of restframe wavelength, as might be

expected from simple extrapolation errors. This is in contrast to the sharp discontinuity in the residuals seen in Fig. 7 between the optical and NIR bands.

Looking now at the right-hand panels of Fig. 7, we see that none of the three SP libraries are able to satisfactorily reproduce the optical–NIR SED shapes of GAMA galaxies without significant systematic biases. Each of the models shows a significant excess of flux for 7000 Å $\lesssim \lambda \lesssim$ 12 000 Å. The significance of the offsets in the *i*-, *Y*- and *J*-bands are $\sim+1.8\sigma$, -1.6σ and -1.4σ, respectively. Based on our numerical experiments, there is no reason to suspect that we should be unable to reproduce the observed optical-to-NIR SED shapes of real galaxies. As can be seen in Fig. A1, the fits to the mock *ugrizYJHK* SEDs are near perfect.

Each of the issues highlighted above points to inconsistencies between the optical-to-NIR colours of our SPL models on the one hand, and of real galaxies on the other. Further, the fact that the models fail to satisfactorily describe the NIR data immediately calls into question the reliability of parameter estimates derived from fits to the full optical-to-NIR photometry. The rest of this section is devoted to exploring the nature of this problem.

4.2 How including NIR data changes the parameter estimates

Fig. 8 shows the difference between SP parameters derived from the *ugriz* and the *ugrizYJHK* photometry, and using the BC03 models to construct our SPL as per Section 3.2. In this figure, the 'Δ's plotted on the *y*-axis should be understood as the nine-band minus five-band-derived value; these offsets are plotted as a function of the five-band-derived value.

In the simplest possible terms, the nine-band fits yield systematically lower values for all of M_*, M_*/L_i, E_{B-V}, $\langle t_* \rangle$ and $(g-i)$ than the five-band fits. Again, based on our experiences with the mock catalogues described in Appendix A, we have no reasons to expect these sort of discrepancies: for the mocks, we are able to recover the input SP parameters with virtually no systematic bias using either the optical-only or optical-plus-NIR SEDs (see Fig. A2).

In each case, based on the formal uncertainties from the five-band fits, the median significance of the offset in the SP parameter estimates is $\gtrsim 1.5\sigma$. For each of these quantities, the nine-band-derived value is formally inconsistent with the five-band-derived value at the $>3\sigma$ level for $\approx$25 per cent of galaxies. (Using the M05 models, we find a similar fraction; using the CB07 models, this fraction goes up to 30–40 per cent.) This shows that the residuals seen in Fig. 7 are more than merely a cosmetic problem – they are symptomatic of inconsistencies between the fits with and without the inclusion of the NIR.

To make plain the importance of these systematic offsets, consider the fact that there are large and statistically significant differences in the $(g-i)$ colours inferred from the nine- and five-band fits. The median values inferred from the fits with the NIR included are 0.10 mag bluer than those based on the optical alone. In comparison to the formal uncertainties in the five-band derived values of $(g-i)$, this amounts to an inconsistency at the $\sim 2.5\sigma$ level. This is despite the fact that the NIR data *by definition* contain no information

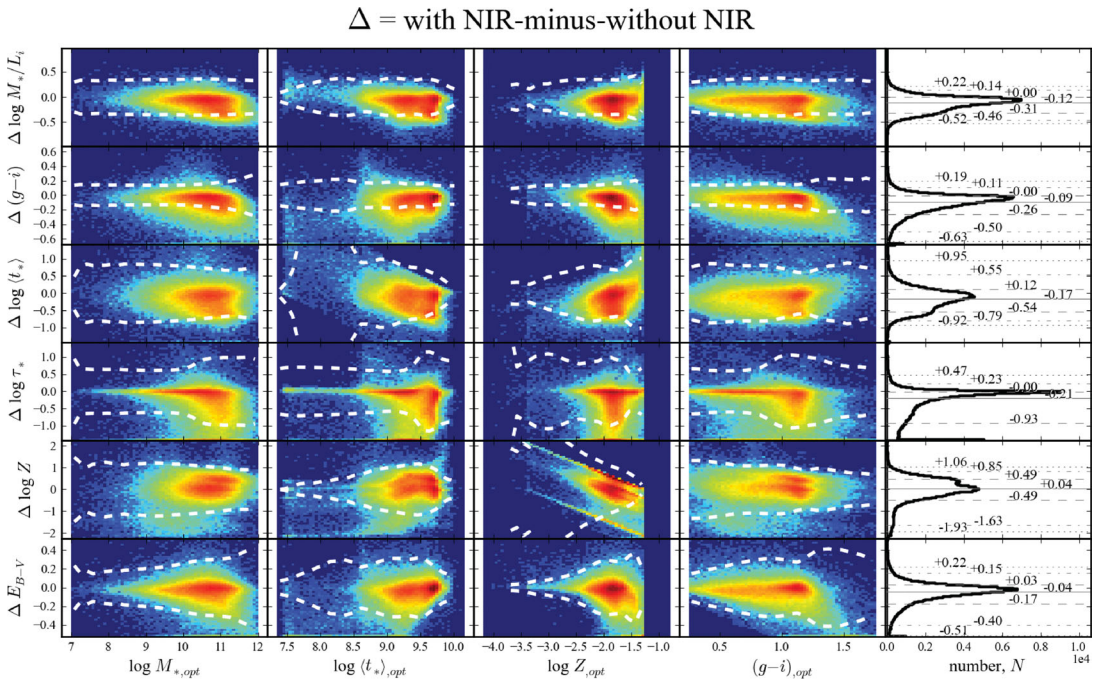

Figure 8. The effect of including the NIR data on the inferred SP parameters. In each panel of this figure, we show the difference between the SP parameters derived using only the *ugriz* photometry, and those derived using the full *ugrizYJHK* SEDs. In all cases, the 'Δ' should be understood as 'optical-plus-NIR-derived' minus 'optical-only-derived'. As in Fig. 5, the histograms in the right-hand panels show the distribution of 'Δs' and the 1/2.5/15/50/85/97.5/99 percentiles. In the other panels, the 'Δ' is plotted as a function of the 'optical-only-derived' value; the colour-scale shows the logarithmic data density for the full GAMA sample. In these panels, the dashed lines show the $\pm 3\sigma$ uncertainties as derived from the fits to the five optical bands. The median effect of including the NIR data is to systematically reduce the inferred value of M_* by $\approx$0.1 dex. It is important to note these offsets NIR-derived values are formally inconsistent with the optical-only-derived uncertainties at the $\gtrsim 2.5\sigma$ level. This is particularly significant in the case of the restframe $(g-i)$ colour [median $\Delta(g-i) = 0.1$ mag], which should be independent of the NIR data. Coupled with the fact that the models do not provide a satisfactory description of the observed SEDs (see Fig. 7), we are thus obliged to consider the NIR-derived SP parameter estimates as suspect.

about $(g - i)$. Looking at Fig. 7, it is clear that the five-band fits are a more reliable means of inferring a restframe $(g - i)$ colour: for the nine-band fits, the differential offset between the g- and i-bands is $\approx$0.10 mag; for the five-band fits, the differential offset is $\lesssim$0.03 mag.

Said another way, because the nine-band fits have the wrong SED shape, they cannot be used to infer a restframe colour. But the same is true of any other derived property – simply put, *if the models cannot fit the data, they cannot be used to interpret them.*

4.3 The sensitivity of different SSP models to the inclusion/exclusion of NIR data

One possible explanation for the large residuals seen in Fig. 8 is problems with the BC03 SSP models. In particular, one might worry that these are related to the NIR contributions of TP-AGB stars. In this context, let us begin by noting that if this were to be the source of the problems that we are seeing, then we would expect the optical-only fits to underpredict the 'true' NIR fluxes, particularly for the BC03 models. But this is not what we see: the optical-only fits *over*predict galaxies' NIR fluxes using both the BC03 and the M05 models, and by similar amounts in both cases.

In Fig. 9, we show the comparison between the M05- and BC03-derived SP parameter values, based on fits to the full *ugrizYJHK* SEDs. It is clear from Fig. 9 that there are systematic differences between the models, particularly (and as expected) for $\langle t_* \rangle \sim 10^{8.5}$–$10^{9.5}$ Gyr.

Taking an empirical perspective on the problem, we can consider these differences as an indication of the degree of uncertainty tied to uncertainties in the stellar evolution tracks that underpin the SSP spectra. Using only the optical data, the *systematic* differences between any of the SP parameter values derived using the different models is small: for M_*/L_i, the median offset is 0.01 dex. That is, when using optical data only, these famously 'disagreeing' models yield completely consistent results. This is in marked contrast to a number of results emphasizing the importance of differences in the modelling of TP-AGB stars in the BC03 and M05 models when NIR data are used (e.g. Cimatti et al. 2008; Wuyts et al. 2009). In terms of 'random' differences, the inferred values of M_* based on the two sets of models agree to within $\pm$0.3 dex (a factor of 2) for 99 per cent of galaxies. We can treat the 15/85 percentile points of the distribution of the 'Δ's as indicative of the 1σ random 'error' associated with the choice of SSP model. For M_*/L, this 'error' is $\lesssim$0.10 dex. That is, when using only optical data, the SP parameter estimates are not significantly model dependent.

When we include the NIR data in the fits, the agreement between the SP values inferred using the two different sets of SSP models is not as good. The inferred values of M_* using the BC03 or M05 models agree to within $\pm$0.5 dex (a factor of 3) for 99 per cent of galaxies; the 1σ random 'error' in M_* is $\approx$0.12 dex. While the inferred values of M_*/L agree reasonably well, the differences in the other inferred SP parameters – E_{B-V}, Z and especially $\langle t_* \rangle$ – are larger. For $\langle t_* \rangle$, the 1σ 'error' is $\approx$0.3 dex; this should be compared to the formal uncertainty in $\langle t_* \rangle$ of $\sim$0.2 dex. Thus, we see that the 'error' in SP parameter estimates associated with the choice of model becomes comparable to the formal uncertainties when, and only when, NIR data are included in the fit.

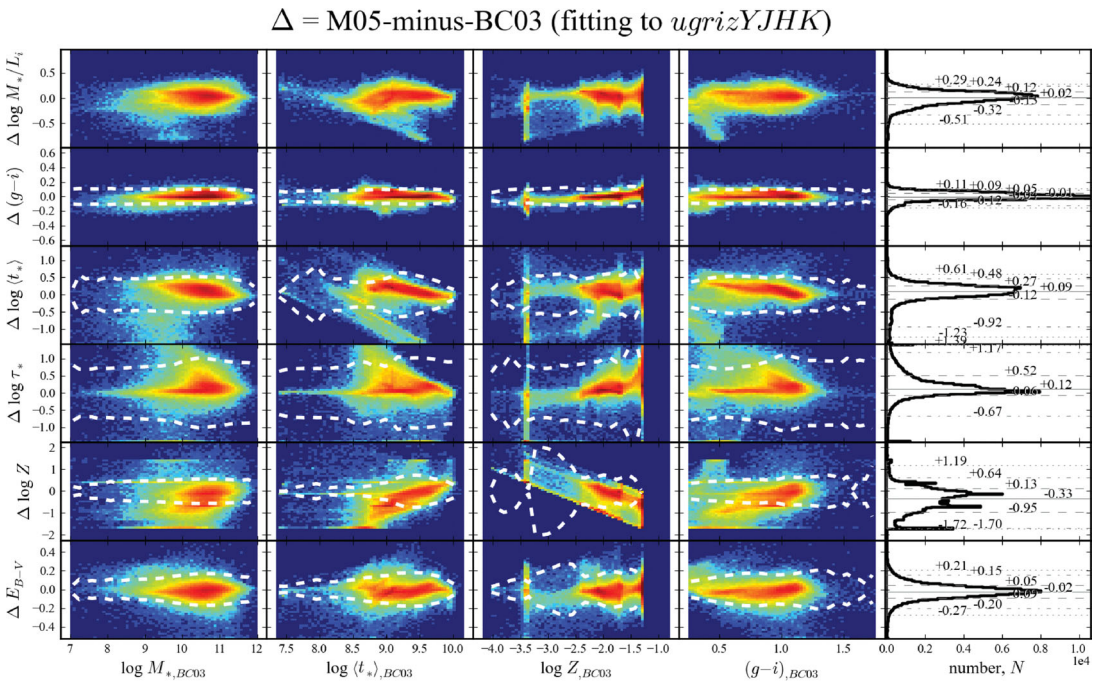

Figure 9. Comparison between M05- and BC03-based parameter estimates, derived from fits to the *ugrizYJHK* SEDs. The 'Δ's in this figure should be understood as the M05-based-minus-BC03-based parameter values; all symbols and their meanings are analogous to Fig. 8. While, as expected, there are some systematics in the inferred values of M_* as a function of $\langle t_* \rangle$, the global agreement is very good. In comparison to Fig. 8, the systematic differences between parameters derived on the basis of the different stellar evolution models (but the same *ugrizYJHK* data) are considerably larger than the differences between the values inferred with or without the inclusion of the NIR data (but the same stellar evolution models). This suggests that our apparent inability to adequately fit the observed optical-to-NIR SED shapes of GAMA galaxies is not a product of errors in the stellar evolution models. At the same time, however, the 'random' differences between the M05- and BC03-based SP parameter estimates are larger than the formal uncertainties when the NIR data are included. This is not true when using only the optical data. That is, the model dependence of the SP parameter estimates becomes significant if, and only if, the NIR data are included.

4.4 What is the problem with the NIR?

What can have possibly gone wrong in the fits to the NIR data? There are (at least) three potential explanations for our inability to obtain a good description of the optical–NIR SED shapes of GAMA galaxies using the models in our SPL. The first is problems in the data. The second is problems in the stellar evolution models used to derive the SSP spectra that form the basis of our template library. The third is problems in how we have used these SSP spectra to construct the CSPs that comprise our SPL.

4.4.1 Is the problem in the data? Maybe.

We cannot unambiguously exclude the possibility of errors in, for example, the basic photometric calibration of the NIR imaging data. In this context, we highlight the qualitative difference in our ability to use optical data to predict NIR fluxes for the real GAMA galaxies on the one hand, and for mock galaxies on the other hand. In particular, the sharp discontinuity in the residuals between the z- and Y-bands for the real galaxies would seem to suggest a large inconsistency between these two bands at the level of $\sim$0.1–0.2 mag.

As described in Section 2.2, GAMA has received the NIR data fully reduced and calibrated. In order to ensure that there are not problems in our NIR photometric methods (which are not different from those in the optical), we have verified that there are no large systematic offsets between our photometry and that produced by CASU. This would suggest that any inconsistencies would really have to be in the imaging data themselves.

The accuracy of the UKIRT WFCAM data calibration has been investigated by Hodgkin et al. (2009) through comparison to sources from the 2MASS point source catalogue (Cutri et al. 2003; Skrutskie et al. 2006): they argue that the absolute calibrations of the Y- and JHK-band are good to $\sim$2 and $\sim$1.5 per cent, respectively. (See also Dye et al. 2006 and Schombert 2011.) Taken at face value, this argues against there being such large inconsistencies in the photometry.

In light of the fact that we have not been directly involved in the reduction or calibration of these data, and with the anticipated availability of the considerably deeper VISTA-VIKING NIR imaging in the near future, we will not investigate this further here.

4.4.2 Is the problem in the SSP models? Probably not.

From what we have already seen, we can exclude errors in the SSP models as a likely candidate. We have shown in Fig. 7 that *none* of the BC03, M05 or CB07 models provides a good description of the full optical-to-NIR SEDs of real galaxies – these models all show qualitatively and quantitatively similar fit residuals. Taken together, the results in Figs 8 and 9 show that (for the same data) the SP parameters derived using different models show small systematic differences, while at the same time (for any given set of SSP models) there is a large systematic difference between the values derived with or without the NIR data. This is not to say that the models are perfect, but the offsets seen in Fig. 7 would appear to be larger than can be explained by uncertainties inherent in the SSP models themselves.

4.4.3 Is the problem in the construction of the SPL? Probably.

This leaves the third possibility that the assumptions that we have made in constructing our SPL are overly simplistic, in the sense that they do not faithfully describe or encapsulate the true mix of SPs found in real galaxies. We defer the discussion of this possibility to Section 6.2. For now, however, we stress that the present SPL *does* seem to be capable of describing the optical SED shapes of real galaxies.

4.5 Summary – why the NIR (currently) does more harm than good

We have now outlined three reasons to suspect that, at least in our case, SP parameter estimates based only on optical photometry are more robust than if we were to include the NIR data.

(i) Regardless of which set of SSP models we use, we see much larger than expected residuals in the SED fits when the NIR data are included. If the models do not provide a good description of the data, then we cannot confidently use them to infer galaxies' SP properties.

(ii) The consistency between the SP parameter estimates derived with or without the inclusion of the NIR data is poor. For a sizeable fraction of GAMA galaxies ($\gtrsim$25 per cent), the SP parameter values inferred from fits to the optical-plus-NIR SEDs are statistically inconsistent (at the 3σ level) with those based on the optical alone.

(iii) When using different models to construct the SPL templates, the agreement between the derived SP parameters is very good when the NIR data are excluded, but considerably worse when the NIR data are included. That is, the fit results become significantly model-dependent when, and only when, we try to include the NIR data.

For these reasons, and for the time being, we choose not to use the NIR data when deriving the stellar mass estimates. This begs the question as to how accurately M_*/L can be constrained based on optical data alone, which is the subject of the next section.

5 THE THEORETICAL AND EMPIRICAL RELATIONS BETWEEN M_*/L AND COLOUR

As we have said at the beginning of Section 4, conventional wisdom says that NIR data provide a better estimate of stellar mass. Our conclusion in Section 4, however, is that we are unable to satisfactorily incorporate the NIR data into the SPS calculation. With this as our motivation, we will now look at how well M_*/L can be constrained on the basis of optical data alone. In particular, we want to know whether or to what extent the accuracy of our stellar mass estimates is compromised by our decision to ignore the NIR data.

5.1 Variations in M_*/L at different wavelengths

Part of the rationale behind the idea that the NIR provides a better estimate of M_*/L is that galaxies show less variation in their NIR M_*/Ls than they do in the optical. We address this issue in Fig. 10; this figure merits some discussion. Each panel of Fig. 10 shows a subsample of the models in our SPL. Within each panel, models are colour-coded according to their metallicity (from the lowest metallicity in blue to the highest metallicity in red). For each metallicity, the slightly heavier line shows how the single burst (i.e. $\tau \rightarrow 0$) track evolves with time, t; the other single-colour lines then connect models with the same age (but different τs) or the same SFH e-folding time (but different ages). Finally, the colour-graded lines connect models with the same t and τ, but different metallicities. In this way, each panel shows a 2D projection of the 3D (t, τ, Z) grid of SPL templates. Note that we only show zero-dust models in this figure; the dust-extinction vector is shown in the lower-right corner of each panel.

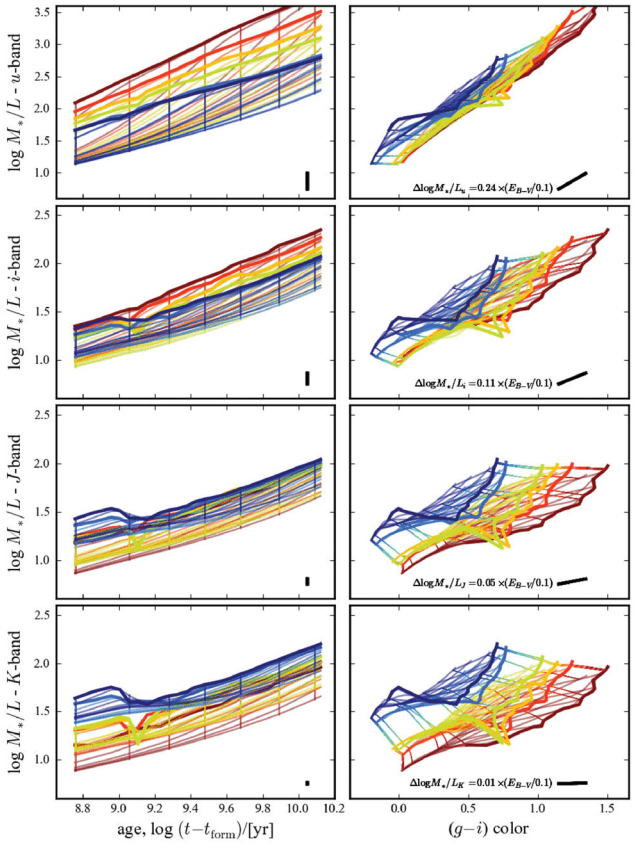

Figure 10. Variations in M_*/L as a function of age and colour for models in our SPL. This figure is discussed at length in Sections 5.1 and 5.2. Each panel of this figure shows a projection of our SP model grid. Individual models are colour-coded by their metallicity. The lines connect models that differ in only one of age, e-folding time or metallicity. We only show zero-dust models; the dust vector is given in the lower-right corner of each panel. From top to bottom, the different rows show the spread of M_*/Ls in the u-, i-, J- and K-bands within the models; these values are plotted as a function of SP age (left-hand panels), and restframe $(g-i)$ colour (right-hand panels). The results shown in this panel imply that u-, i-, J- or K-band fluxes on their own can be used to infer stellar masses to within a factor of 22, 5.5, 4.0 and 4.5, respectively. That is, on its own, L_i is almost as good an indicator of M_* as L_J or L_K. At the same time, the variation in M_*/L_i *at fixed* $(g-i)$ is considerably smaller: M_*/L_i can in principle be predicted to within a factor of 2 using $(g-i)$ colour alone.

Each row of Fig. 10 shows the mass-to-light ratio in different bands (*uiJK*, from top to bottom). Let us look first at the first column, in which we plot each of these M_*/Ls as a function of age. For fixed Z and τ, and particularly for $t \gtrsim 2$ Gyr, it is true that the NIR M_*/L varies less with t than does the optical M_*/L – but not by all that much. For the SSP models, the total variation in M_*/L between 2 and 10 Gyr is $\lesssim$1.2 dex in the u-band, compared to $\lesssim$0.7 dex in the i-band, and $\approx$0.6 dex in the J- and K-bands. Similarly, it is also true that at fixed t and Z, the spread in M_*/Ls for different τs is slightly smaller for longer wavelengths: the total variation goes from $\lesssim$1.2 dex in the g-band to $\lesssim$0.4 dex in the i-band, to $\lesssim$0.3 dex in the J- and K-bands. Considering variations in M_*/L with all of t, τ and Z, the full range of M_*/Ls becomes 2.7, 1.4, 1.2 and 1.3 dex in the *uiJK*-bands, respectively; these values imply mass accuracy on the order of factors of 22, 5.5, 4.0 and 4.5.

While it is thus true that galaxies tend to show less variation in their values of M_*/L towards redder wavelengths (see also Bell & de Jong 2001), it seems that the most important thing is to use a band that is redder than the 4000 Å and Balmer breaks – the range in M_*/L_i is not all that much greater than that in M_*/L_K or M_*/L_J.

5.2 The generic relation between M_*/L and restframe colour

Let us turn now to the second column of Fig. 10, where we show the relation between M_*/L and restframe $(g-i)$ colour (cf.. e.g. fig. 2 of Bell & de Jong 2001; fig. 1 of Zibetti et al. 2009). The principal point to be made here is that, *at fixed* $(g-i)$, the range M_*/L_i is $\lesssim$0.5 dex, whereas, and particularly for blue galaxies, the spread in the NIR M_*/L is more like 0.65–1.0 dex. That is, by the same argument we have used above, using only g- and i-band photometry, it is possible to derive stellar mass estimates that are accurate to within a factor of $\lesssim$2.

5.2.1 *The effects of dust*

In what we have said so far in this section, we have completely ignored dust. This may have seemed like a very important oversight, so let us now address this issue. The dust vector in $(g-i)$–M_*/L_i space is $(\Delta(g-i), \Delta(\log M_*/L_i)) = (0.19, 0.11) \times E_{B-V}/0.1$. Compare this to the empirical $(g-i)$–M_*/L_i relation for GAMA galaxies, which, as we show in Section 5.3, has a slope of 0.73. Because these two vectors are roughly aligned, the first order effect of dust obscuration is merely to shift galaxies along the $(g-i)$–M_*/L_i relation (see also Bell & de Jong 2001; Nicol et al. 2011). This means that the accuracy of $(g-i)$-derived estimates of M_*/L_i is not sensitive to a galaxy's precise dust content. Said another way, although there may be large uncertainties in E_{B-V}, this does not necessarily imply that there will also be large uncertainties in M_*/L_i.

To see this clearly, imagine that we were only to use zero-dust models in our SPL, and take the example of a galaxy that in reality has $E_{B-V} = 0.1$ mag. In comparison to the zero-dust SPL model with the same t, τ, and Z, this dusty galaxy's $(g-i)$ colour becomes 0.19 mag redder, and its absolute luminosity drops by 0.11 dex; the effective M_*/L_i is thus increased by the same amount. (Recall that L_i denotes the effective absolute luminosity *without* correction for internal dust obscuration, rather than the intrinsic luminosity produced by all stars.) Now, using the slope of the $(g-i)$–M_*/L_i relation, the inferred value of M_*/L_i for the $E_{B-V} = 0.1$ mag galaxy will be $0.70 \times 0.19 = 0.13$ dex higher than it would be for the same galaxy with no dust. That is, in this simple thought experiment, the error in the value of the effective M_*/L_i implied by $(g-i)$ would be $0.02 \times (E_{B-V}/0.1)$ dex, even though we would be using completely the wrong kind of SPS model to 'fit' the observed galaxy.

Note that this argument holds only to the extent that dust can be accurately modelled using a single dust vector, i.e. a single screen approximation. Using the Fischera & Dopita (2005) attenuation curve, which is a single screen approximation to a fractal dust distribution, does not produce a large change in the derived values of M_*/L. Using the model of Tuffs et al. (2004) and Popescu et al. (2000), Driver et al. (2007) show how variations in both viewing angle and bulge-to-disc ratio can produce a spread in the colour–M_*/L dust vectors. These results suggest that in some cases, dust geometry may have a significant effect on the colour-inferred value of M_*/L, at the level of $\Delta M_*/L_V \sim 0.1 E_{B-V}$. One avenue for further investigation of the effects of dust geometry is through detailed radiative transfer modelling for galaxies whose geometries can be accurately constrained. While this is clearly impractical for large galaxy samples, an alternative would be to construct spatially

resolved mass maps (see e.g. Conti et al. 2003; Lanyon-Foster, Conselice & Merrifield 2007; Welikala et al. 2008; Zibetti et al. 2009), using a single-screen approximation for each pixel individually.

5.2.2 *Dependence on t, τ and Z*

Just as $(g-i)$ can be used to estimate M_*/L_i without being strongly sensitive to dust, variations in each of age, SFH and metallicity do not have a large impact on $(g-i)$-inferred estimates of M_*/L_i. This is demonstrated in Fig. 11, in which we use our SPL models to show how variations in any one of t, τ, or Z shift galaxies in the $(g-i)$–M_*/L_i plane. We do this as follows: for an individual model, we ask how great a change in any one of t, τ, or Z (while holding the other two parameters fixed) is required to change $(g-i)$ by 0.05 mag; we then look at the corresponding change in M_*/L_i that comes with this variation. In other words, we are looking at how uncertainties in each of t, τ, and Z affect the accuracy of $(g-i)$-inferred estimates of M_*/L_i. These are shown as the red, yellow, and blue vectors, respectively.

Focusing on each set of vectors individually, it can be seen that for the bulk of the models, the effect of independent variations in any of t, τ, or Z is to move the model point more or less parallel to the main cloud. Note, too, that closer to the centre of the main cloud, the three separate vectors tend to come into closer alignment.

To the first order, then, variations in any one of these quantities simply shift galaxies along the main $(g-i)$–M_*/L_i relation. By the same argument presented above with regard to dust, this implies that $(g-i)$ can be used to infer M_*/L_i to high accuracy, even if the 'best-fitting' model of the same $(g-i)$ colour has completely the

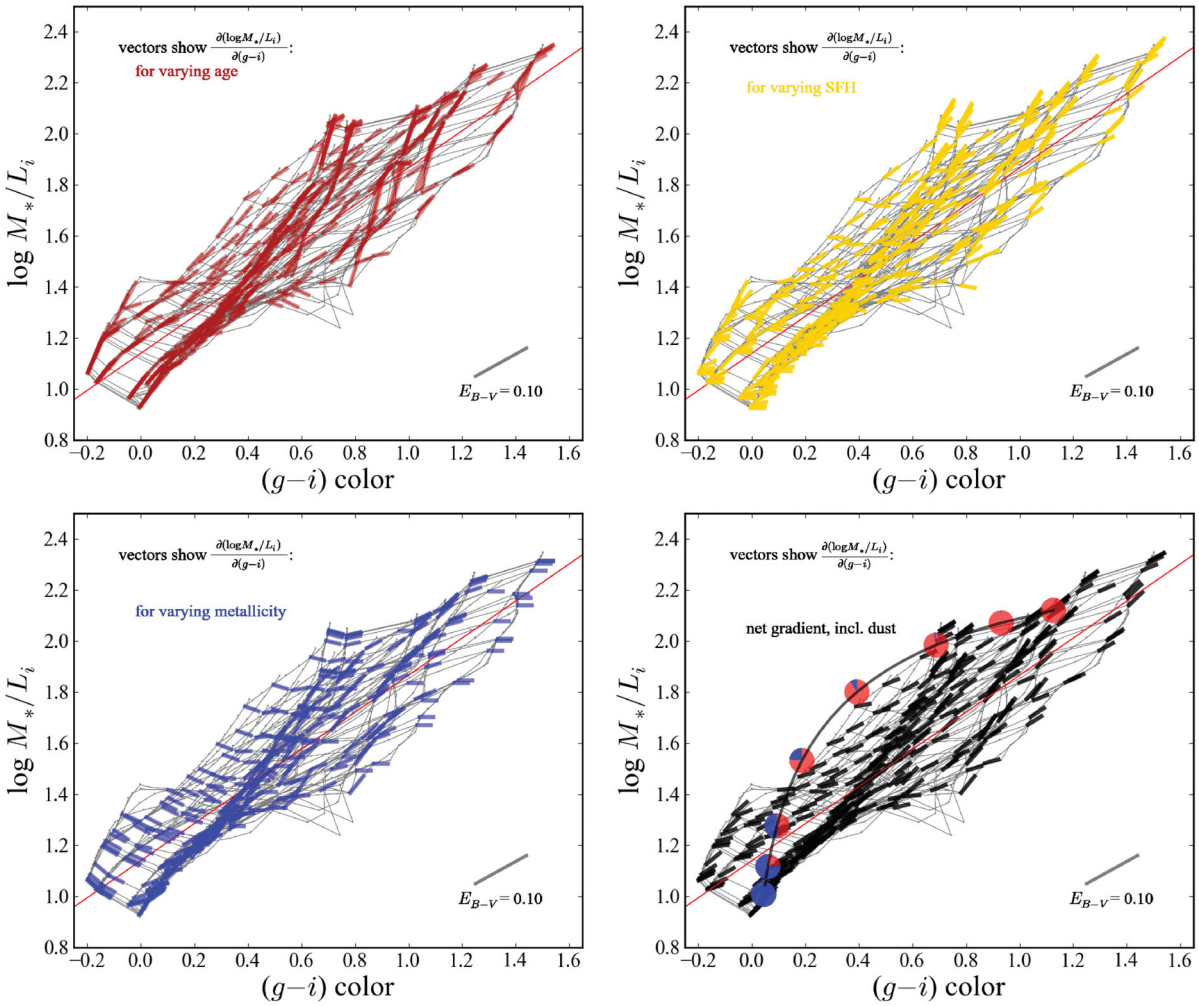

Figure 11. The generic relation between restframe $(g-i)$ colour and M_*/L_i for the models in our SPL. The first three panels of this figure show the movement of the models in our SPL in the $(g-i)$–M_*/L_i plane with variations age, SFH, and metallicity, respectively. In each of these panels, the vectors show the age, SFH, or metallicity analogues of the dust vector for $\Delta(g-i)=0.05$; that is, the change in M_*/L_i that is associated with a change in t, τ, or Z such that the restframe $(g-i)$ colour changes by 0.05 mag. In the fourth panel, the black vectors show the net variation in $\Delta M_*/L_i$ with a 0.05 mag change in $(g-i)$, obtained by marginalizing over the t, τ, and Z priors. The fact that each of these vectors – both individually and *en masse* – is roughly aligned with one another means that variations in any of these parameters largely preserves both the slope of and scatter around the relation between $(g-i)$ and M_*/L_i (see Section 5.2). Further, in the final panel, we provide a qualitative illustration of how multi-component SPs affect the $(g-i)$–M_*/L_i relation by combining an old and passive SP with a young, star-forming one. These are shown as the large circles connected by the smooth black curve. The relative young:old mass ratio is indicated by the relative area of the blue and red regions within each circle for young mass fractions of approximately (right to left) 0, 1, 3, 9, 24, 50, 76 and 100 per cent. Even for this rather extreme example of multi-component SPs, it remains true that $(g-i)$ colour can, in principle, be used to estimate M_*/L_i to within a factor of ∼2 (0.3 dex).

wrong values of t, τ, or Z. Fig. 11 thus shows that uncertainties in any of t, τ, and Z do not produce large errors in the value of M_*/L_i inferred from the $(g-i)$ colour.

5.2.3 *The net covariance between M_*/L_i and $(g-i)$*

Considering the combined effect of variations in all three of t, τ, and Z, the robustness of $(g-i)$-derived estimates of M_*/L_i is even greater. The black vectors in this plot show the net variation in M_*/L_i allowing for the uncertainties in all of t, τ, and Z that come with an observational uncertainty of $\Delta(g-i)=0.05$. Notice how closely aligned these vectors are with the empirical $(g-i)$–M_*/L_i relation for real galaxies.

This shows that while there may well be a relatively large range of models with different values of t, τ, and/or Z that are consistent with the observed value of $(g-i)$ for any given galaxy, because all of these models will follow more or less the same relation between $(g-i)$ and M_*/L_i, the spread of M_*/L_is among these models will still be relatively low. That is, through a coincidence of dust and SP evolution physics, *the dust–age–metallicity degeneracy actually helps in the estimate of M_*/L_i* (see also e.g. Bell & de Jong 2001; Nicol et al. 2011). Furthermore, as a corollary to this statement, because the estimated value of M_*/L_i does not depend strongly on the accuracy of the inferred values of t, τ, Z, or E_{B-V}, it is not necessary to model these aspects of the SPL models exactly.

5.2.4 *Multi-component stellar populations*

The last commonly cited bugbear of stellar mass estimation is the effect of 'secondary' populations in general, and of bursts in particular, on the inferred value of M_*/L. To explore this issue, consider the case of a combination of two SPs with $(t,\ \tau,\ Z) = (10\ \mathrm{Gyr},\ 0.5\ \mathrm{Gyr},\ Z_\odot)$ and $(0.5\ \mathrm{Gyr},\ 30\ \mathrm{Myr},\ Z_\odot)$, i.e. an old and passive SP and a very young and star-forming SP. These two individual SPs are highlighted in the fourth panel of Fig. 11. Now let us combine these two SPs in varying amounts. The track connecting these two points shows where the combined SP would lie in the M_*/L_i–$(g-i)$ plane. The large points highlight the cases where the mass of the burst component is $10^{-2}, 10^{-1.5}, \ldots, 10^{0.5}$ times the mass of the old component.

We again see that the M_*/L_i–$(g-i)$ relation is largely preserved. In particular, the effect of small bursts ($f_{\mathrm{young}} \lesssim 0.05$) on the M_*/L_i–$(g-i)$ colour relation is very slight. At least for the specific case that we have chosen to illustrate, we see that if a very old galaxy were to experience a modest burst ($0.05 \lesssim f_{\mathrm{young}} \lesssim 25$ per cent), then this will shift the galaxy along the edge of the main cloud. The greatest concern is a largely star-forming galaxy with a sizeable underlying population of very old stars ($0.25 \lesssim f_{\mathrm{old}} > \lesssim 0.75$). In this case, M_*/L_i can shift by up to 0.5 dex with only a small change in colour; $\Delta(g-i) \lesssim 0.2$.

It is thus clear from this panel that secondary SPs in general, and those with $0.25 \lesssim f_{\mathrm{young}} \lesssim 0.75$ in particular, are better able to shift galaxies away from the main M_*/L_i–$(g-i)$ relation than are variations in any or all of t, τ, Z, or E_{B-V} within one of our smooth and exponential CSPs. That said, we stress this specific example represents something of an extreme case: the two separate SPs we have chosen are at opposite ends of the SP values that we find for real galaxies, and the problem is only significant where the two populations are comparable in mass. Furthermore, even for this extreme example, note that the combined SP still lies within the main cloud of SPs within our SPL. The claim that M_*/L_i can be estimated to within a factor of $\lesssim 2$ based on the $(g-i)$ colour alone is true even for galaxies with relatively complex SFHs.

5.3 The empirical relation between $(g-i)$ and M_*/L_i

So far in this section, our discussion has been restricted to the range of M_*/Ls and colours spanned by the models in our SPL, and has thus focused on the theoretical relation between $(g-i)$ and M_*/L_i. In this sense, our conversation has been completely generic – at least in so far as the SP models we have used provide an accurate description of the stellar content of real galaxies.

Let us now turn to Fig. 12, and consider how well $(g-i)$ can be used to estimate M_*/L_i in practice. In this figure, the grey-scale contours show the prior-weighted distribution on M_*/L_i for the models, again in bins of $(g-i)$: the darkest line shows the median prior-weighted value; the contours show the equivalent of the ± 0.5, 1.0, ..., 3.0σ percentiles. This figure also shows the empirical relation between $(g-i)$ and M_*/L_i that we infer for real GAMA galaxies, based on our *ugriz* SPS fits. The data themselves are shown as the blue points.

Consider for a moment what would happen if we were to have only (restframe) g- and i-band photometry for a real galaxy. The inferred value of M_*/L_i would just be the mean value of all models in our SPL with a similar colour (weighted by both the consistency between the observed and model photometry, and the prior probability of that model). Further, for a given $(g-i)$, the inferred uncertainty in M_*/L_i would simply reflect the prior-weighted range of values spanned by models of the same colour. That is, we would expect to 'recover' the prior-weighted distribution shown as the grey contours in Fig. 12.

This is not what we see for the real galaxies: there are clear differences between the form of and scatter around the relations between $(g-i)$ and M_*/L_i for the models on the one hand, and for the data on the other hand. Particularly for intermediate colours, the median value of M_*/L_i is considerably lower than the probability-weighted mean of the models. This demonstrates that the u-, r- and z-band data do provide additional information concerning M_*/L_i that cannot be gleaned from $(g-i)$ alone.[13]

Further, the effect of this additional information is to significantly *reduce* the observed scatter in the relation between $(g-i)$ and M_*/L_i. The red points in Fig. 12 show the median values of M_*/L_i for GAMA galaxies in narrow bins of $(g-i)$. The error bars on these points show the mean values of the formal 1σ upper and lower limit on M_*/L_i in each bin; these error bars thus show the intrinsic, astrophysical scatter in the relation convolved with the formal, observational uncertainties. Even considering the formal uncertainties for individual galaxies, the scatter around the mean colour–M_*/L_i relation is considerably lower than what would be expected from the models alone: quantitatively, the scatter in M_*/L_i is constrained to being $\lesssim 0.1$ dex for all values of $(g-i)$. This shows that *the apparent tightness of the relation between $(g-i)$ and M_*/L_i is not a mere consequence of the central limit theorem*.

In other words, the precise form of the empirical relation between $(g-i)$ and M_*/L_i encodes information about the distributions of SPs among real galaxies. Both the linearity and tightness of the

[13] This point is significant in terms of our assumed priors: if the *urz*-band photometry did not provide additional SP information, then the observed relation would be strongly dependent on the specific priors used; particularly the assumed prior on τ.

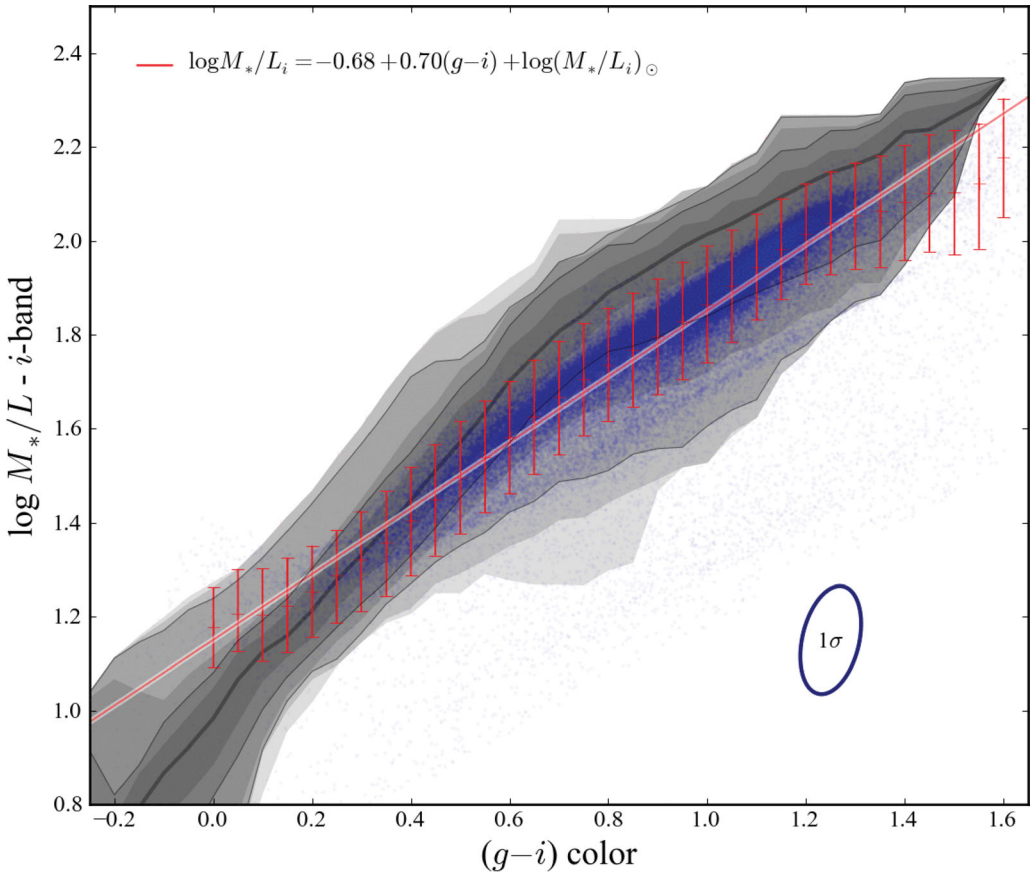

Figure 12. The empirical relation between restframe $(g - i)$ colour and M_*/L_i. The points show the inferred values of $(g - i)$ and M_*/L_i for galaxies in the GAMA catalogue. The red points show the median value of M_*/L_i in narrow bins of $(g - i)$; the error bars on these points reflect the median $\pm 1\sigma$ upper and lower limits on M_*/L_i in each bin. These error bars thus reflect the combination of the (small) intrinsic scatter in the $(g - i)$–M_*/L_i relation and the (larger) formal uncertainties in M_*/L_i at fixed $(g - i)$. The solid red line shows the best fit to the empirical relation between $(g - i)$ and M_*/L_i, with the form as given at top left. In fitting this relation, we have fully accounted for the covariant errors in $(g - i)$ and M_*/L_i; the median error ellipse is shown at bottom right. For comparison, the underlaid grey-scale contours show the prior-weighted distribution of M_*/L_is for the models in our SPL, computed in narrow bins of $(g - i)$. The heavy central line shows the prior-weighted median, and the contours are spaced at the equivalent of the ± 0.5, 1.0, ..., 3.0 σ percentiles of the prior-weighted distribution. The observed relation for real galaxies is both more nearly linear and tighter than might be expected from the models alone. This implies both that the full *ugriz* SED contains additional information concerning a galaxy's SP not embodied in the $(g - i)$ colour alone, and that the precise form of and scatter around the $(g - i)$–M_*/L_i relation is a product of galaxies' formation and evolutionary histories. In this sense, we have calibrated the $(g - i)$–M_*/L_i relation such that, modulo uncertainties in the SP models used to derive these values, the $(g - i)$ colour can be used to predict M_*/L_i to a 1σ accuracy of $\approx$0.10 dex.

observed relation are therefore fortuitous coincidences of the physics of galaxy formation and evolution.

Fitting the empirical relation for GAMA galaxies, we find

$$\log M_*/L_i = -0.68 + 0.70(g - i). \quad (7)$$

(To convert M_*/L_i from our preferred AB-centric units to solar units, note that the absolute AB magnitude of the Sun in the i-band is $M_{i,\odot} = 4.58$.) This fit is shown in Fig. 12 as the solid red line. In the fitting, we have fully accounted for the covariant errors in the derived values of $(g - i)$ and M_*/L_i; the mean error ellipse is shown in the lower-right corner of this panel. Rearranging equation (7) to put all observables to one side, we have in effect calibrated the empirical relation between $(g - i)$ colour, i-band luminosity and stellar mass as

$$\log M_*/[M_\odot] = 1.15 + 0.70(g - i) - 0.4M_i, \quad (8)$$

where M_i is the absolute magnitude in the restframe i-band, expressed in the AB system. *This relation can be used to estimate M_*/L_i to a 1σ accuracy of $\sim$0.10 dex using (restframe) g- and i-band photometry alone.*

5.4 Comparison with other recent works

In Fig. 13, we compare our empirically calibrated M_*/L_i–$(g - i)$ relation to two other recent works. From the outset, let us stress that these relations are *not* directly comparable, in the sense that they have been derived in very different ways, and therefore should be interpreted as having rather different meanings.

First, the dashed blue line shows the relation given by Bell et al. (2003), which has been derived from least-squares SED fitting to *ugriz* SEDs for galaxies from the SDSS Early Data Release (EDR; Stoughton et al. 2002) coupled with K-band photometry from 2MASS (Cutri et al. 2003; Skrutskie et al. 2006), and using Pégase (Le Borgne & Rocca-Volmerange 2002) SSP models as the basis of the SPL. We have scaled the Bell et al. (2003) relation down by 0.093 dex to account for their use of a 'diet Salpeter' rather than Chabrier (2003) IMF. Most importantly, Bell et al. (2003) explicitly attempt to account for evolution between the epoch of observation and the present day by running forward the implied SFH to $z = 0$. With that caveat, the Bell et al. (2003) relation is derived from fits

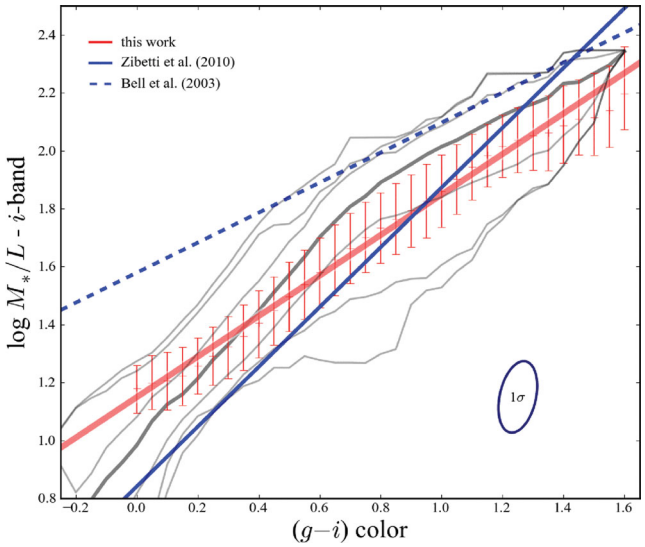

Figure 13. Comparison between our empirical M_*/L_i–$(g-i)$ relation and other recent works. The dashed and solid blue lines in this figure show the relations between M_*/L_i and $(g-i)$ presented by Bell et al. (2003) and Zibetti et al. (2009), respectively; all other symbols are as in Fig. 12. The Bell et al. (2003) relation has been derived for galaxies from the SDSS EDR, and should thus be compared to our empirical relation. Note, however, that the Bell et al. (2003) relation should be understood to include evolution corrections. The Zibetti et al. (2009) relation has been obtained by marginalizing over the models in their SPL in bins of $(g-i)$. This relation thus cannot be considered to be 'empirical', and should be compared to the prior-weighted median for our SPL, shown as the heavier grey line. The significant systematic differences between these relations underscore the importance of ensuring that any cross-survey comparisons are based on a comparable mass scale.

to the observed relation between M_*/L and colour for real galaxies in a similar way as in this work, and so can be compared to our relation, shown in Fig. 13 as the solid red line.

Secondly, the solid blue line shows the relation derived by Zibetti et al. (2009), which is based on a Monte Carlo realized SPL modelled after Kauffmann et al. (2003a) (i.e. including secondary SF bursts), with a sophisticated treatment of dust extinction using the formalism of Charlot & Fall (2000). The relation shown has been derived by marginalizing over all SPL models in bins of $(g-i)$. The Zibetti et al. (2009) relation should therefore be compared to the heavier grey line in Fig. 13, which shows the prior-weighted median value of M_*/L_i, computed in bins of $(g-i)$, for our SPL. That said, there is still one important caveat: Zibetti et al. (2009) have marginalized over their dust priors, whereas the grey line in Fig. 13 is based only on the zero-dust models in our SPL. Note that the precise form of the Zibetti et al. (2009) line is determined almost entirely by their assumed priors (i.e. the relative weighting given to the different models in their SPL); no observational data have been used to derive this relation.

The reader may be forgiven for being startled by the apparently poor agreement between these relations in the first instance, and then equally by the subtleties in their meanings. The point to take from this comparison is simply that there are important systematic differences between each of these mass determinations. (Although, again, we stress that we have shown our M_*/L_i estimates to be in excellent agreement with the well-tested and widely used SDSS values.) It is clear from Fig. 13 that comparing results based on different mass determination methods would not be fair, or at best, would be misleading. The utility of these relations is therefore primarily that they provide a means for simply and transparently reproducing the results of more sophisticated calculations, 'warts and all', i.e. including any and all systematics. The derived relation between $(g-i)$ and M_*/L_i thus provides a solid basis for comparison between results from GAMA (and, by extension, SDSS), and from other survey projects.

6 DISCUSSION – WHERE TO FROM HERE?

In this penultimate section, we look at how our SP parameter estimates might be improved for future GAMA catalogues. First, in Section 6.1, we look at what might be gained by successfully integrating NIR data into our SPS calculations. Then, in light of our present difficulties in incorporating the available NIR data, in Section 6.2, we explore potential avenues for improving on the present SP parameter estimates. In particular, we argue that any future improvements in our SPS calculations will require a new conceptual framework.

6.1 The value of NIR data

Let us now consider what additional information may be provided by the inclusion of NIR data, or, conversely, what we have sacrificed by excluding the available NIR data for the present catalogue of stellar masses and SP parameters. Our discussion of this question is based on Fig. 14. As in Fig. 10, these panels show the variation in M_*/L at different wavelengths for our SPL. The left-hand panels show M_*/L as a function of $(g-i)$ colour; the right-hand panels show the same as a function of $(i-K)$ colour. Using this figure, then, we can compare the information encoded in optical-minus-optical and optical-minus-NIR colours.

Fig. 14 shows that most of the additional information encoded within optical-to-NIR colours is concerning metallicity: the fact that each of the single-metallicity surfaces are well separated in the right-hand panels shows that the different metallicity models can be easily distinguished by their $(i-K)$ colours. While the single-age metallicity surfaces are well-separated, however, the fact that each of these surfaces spans a narrower range of $(i-K)$ colours than $(g-i)$ colours shows that both t and τ are better constrained by $(g-i)$. That is, the inclusion of NIR data will not necessarily lead to tighter constraints on galaxies' individual SFHs. Further, by the same argument that we have used in Sections 5.1 and 5.2, it is immediately clear from Fig. 14 that the $(i-K)$ colour encodes virtually *no* information directly pertaining to M_*/L: the range of M_*/L within our SPL is nearly constant as a function of $(i-K)$. To be sure, optical-to-NIR SED shape is a powerful means of breaking degeneracies associated with metallicity, but *this has very little bearing on the inferred value of* M_*/L_i.

In this way, Fig. 14 offers a means of understanding the results of the numerical experiments presented in Appendix A. In this Appendix, we find that the principal gain that comes with the inclusion of the NIR is in our ability to recover the known values of Z for the mock galaxies. Although the inclusion of NIR data has little to no effect on our ability to recover t or τ individually, our ability to recover $\langle t_* \rangle$ is improved (from ∼80 to ∼55 per cent) with the inclusion of the NIR. That is, while NIR data do help to break the degeneracy between metallicity and luminosity-weighted mean stellar age, it does not help to constrain galaxies' precise SFHs. We also find that including the NIR data has little effect on our ability to recover the known values of M_*/L for synthetic galaxies: we are able to recover the known values of M_*/L to within ≈0.05 and ≈0.06 dex with and without the inclusion of NIR data, respectively.

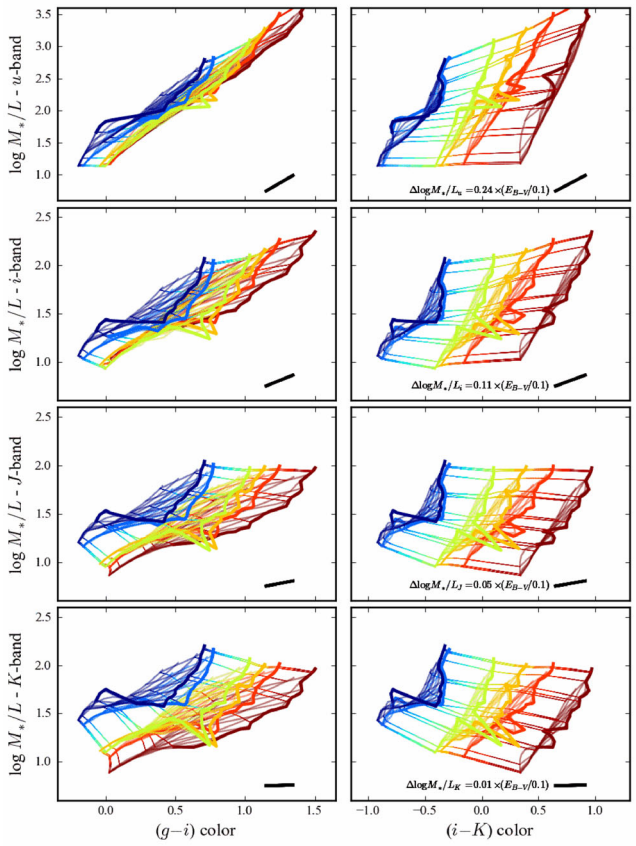

Figure 14. Variations in M_*/L as a function of restframe $(g - i)$ and $(i - K)$ colour for models in our SPL. All symbols and their meanings are as in the directly comparable Fig. 10. In contrast to $(g - i)$, optical-minus-NIR colours contain virtually no information directly pertaining to M/L, or to age. Instead, the optical-to-NIR colour is sensitive primarily to variations in dust and metallicity. While the inclusion of NIR data into the SPS fitting calculation may in principle lead to tighter constraints on t, τ, Z, and E_{B-V}, it will have little to no impact on the accuracy of our M_*/L estimates.

We therefore conclude that the robustness and reliability of our stellar mass estimates will not necessarily be improved simply by folding the NIR data into the SPS calculations – or, said another way, our decision to exclude the NIR data for the current catalogue does not necessarily have a large adverse effect on the quality of our stellar mass estimates.

6.2 Building a better synthetic stellar population library

In Section 4.4, we have suggested that our problems in satisfactorily incorporating the available NIR data into the SPS calculation may reflect that our present SPL is inadequate to the task of describing the full optical-to-NIR SED shapes of real galaxies. In this section, with an eye towards the availability of the much deeper VST-KIDS and VISTA-VIKING optical and NIR imaging in the near future, we discuss possible avenues for deriving improved SP parameter constraints. In particular, we are interested in the first instance in what kinds of expansions of our SPL are likely to have the greatest impact on our SPS calculation; secondarily to this, we want to know whether and what modifications to our SPS algorithm will be required to fully exploit these high-quality data.

Our discussion is based on Fig. 15, in which we show colour–colour diagrams for two heavily populated redshift intervals in the GAMA sample. The coloured lines in Fig. 15 show the evolutionary tracks for models in our SPL with different values of τ and Z. Each track is colour-coded according to its metallicity. For clarity, we only show the models with zero dust; the $E_{B-V} = 0.1$ dust vector is shown at the bottom right of each panel. These tracks should be compared to the actual observations, which are shown as the black points. Based on this figure, let us now consider how our ability to fit the optical-to-NIR SEDs of real galaxies might change with an expanded SPL template set.

6.2.1 *Expanding the metallicity grid*

The upper panels of Fig. 15 show $(g - i)$ versus $(r - i)$. Note that in the optical, the different uniform metallicity models in our SPL almost completely overlap. But as you go further towards the NIR (lower panels), the distance between the different metallicity tracks steadily grows. Looking at the bottom panels, it is clear that the relatively coarse grid of Z values used for our present SPL only sparsely samples the *giK* colour space of real galaxies. Particularly for the gap between $\log Z = -3.4$ and -2.4, the distance between the distinct metallicity tracks in $(i - K)$ becomes comparable to the imposed error floor of 0.05 mag (see Section 3.2). This explains the origin of the most striking feature of Fig. 9: the rather strong quantization in Z. Galaxies with colours that lie between the distinct metallicity tracks can only be fit by adopting the too-blue, lower metallicity model, with the addition of some dust to compensate.

The implication, then, is that a finer grid of metallicities is required when working with NIR data than when working with optical data alone. (This is a direct corollary to the fact that optical-minus-NIR colours are sensitive to metallicity in a way that optical colours are not.) The problem here is twofold. The first problem is a mundane, practical one: the size of our current SPL is already about as big as we can deal with. With the current architecture of our code, we cannot easily expand the grid in any one dimension without reducing its size in some other dimension to compensate.

The bigger problem is that the BC03 (like the M05 and CB07) SSP models cover only a relatively coarse grid in stellar metallicities. In principle, it is trivial to generate models with arbitrary metallicity by interpolating between the SSP models provided by BC03, M05, or whomever. However, at a fixed age, the Z-dependence of both flux and SP properties is complex. For this reason, we consider it unwise to blindly interpolate between models of different metallicities.[14]

To ensure that our coarse metallicity grid is not responsible for the problems we are seeing with the NIR data, however, we have tried re-fitting the galaxies in our main sample with $z < 0.12$ galaxies (i.e. we have reduced the size of our redshift grid by a factor of $\sim$5) using a finer Z grid for the SPL. This grid, which we have generating by interpolating between the different metallicity SSP models at fixed age and wavelength, spans the same range as the native BC03 SSP grid in 24 logarithmically spaced steps.

Using a finer metallicity grid makes no appreciable difference to the quality of the fits to the optical-plus-NIR data. The biggest difference between the two fits is that, with the finer Z grid, the

[14] While some authors have used interpolation to generate models of arbitrary metallicity, our suggestion would be that it might be more appropriate to interpret these models as being linear combinations of the different metallicities, that is, mixed metallicity SPs, rather than intermediate-metallicity SPs. This issue will be addressed in more detail by Robotham et al. (in preparation).

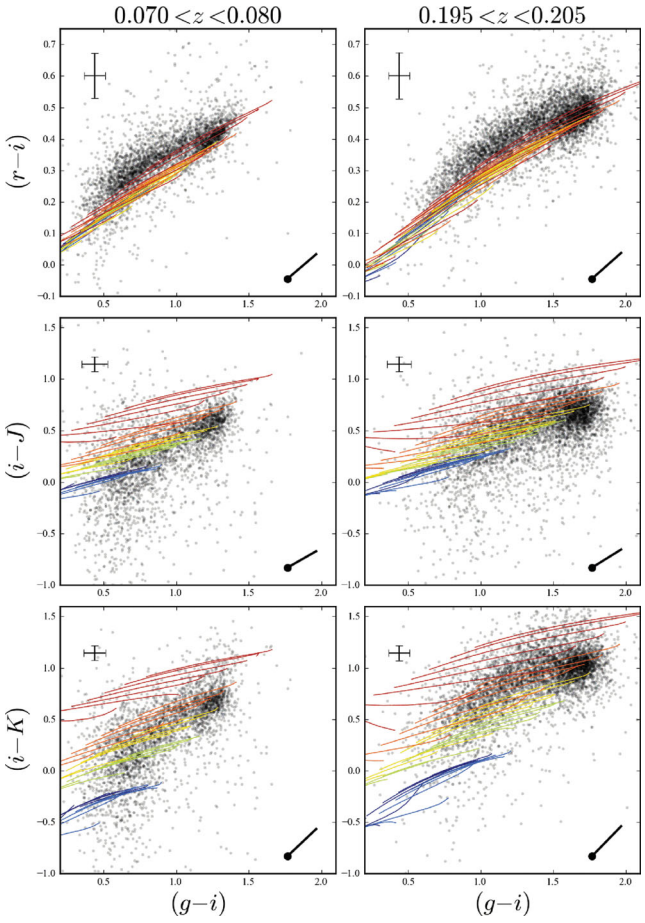

Figure 15. Comparing the model and observed optical and NIR colours for galaxies in two narrow redshift intervals. Each panel of this figure shows a (observers' frame) colour–colour diagram for these two redshift intervals: from top to bottom, we plot $(r - i)$, $(i - J)$, and $(i - K)$ against $(g - i)$. The grey points show the observed colours of GAMA galaxies. We have deliberately selected two well-populated spikes in the GAMA redshift distribution. The coloured tracks show models from our SPL, colour-coded by their metallicity. The $E_{B-V} = 0.1$ dust obscuration vector is shown in the lower-right corner of each panel. The point to be made from this figure is that the single metallicity SPs in our library only sparsely cover the observed optical–NIR colour–colour space of real galaxies. A finer metallicity grid in the stellar evolution models is required for adequate SPS modelling using NIR data.

inferred values of Z for galaxies with $-3.5 \lesssim \log Z \lesssim -2.5$ are systematically higher by $\approx$0.3 dex. But even so, compared to the optical-plus-NIR fits using the native BC03 metallicity grid, the change in the inferred value of M_*/L_i is less than 0.06 dex for 99 per cent of galaxies; the median change is <0.01 dex. We therefore conclude that simply expanding our metallicity grid does not fix our current problems with incorporating the NIR data into the SPS fits, nor does it significantly improve the accuracy of our stellar mass estimates.

In principle, it is easy to accommodate more sophisticated treatments of mixed metallicities by generalizing equation (1) so that the SFR is an explicit function of Z as well as t. In practice, however, the principal disadvantage to doing so is that we would want to specify or parametrize the relations between $\psi_*(t)$ and $Z(t)$, either explicitly, or in terms of appropriate priors. (Further, this does not address the issue of whether and how one can safely generate SSP models of arbitrary metallicity.) One simple way to accomplish this would be to assume an exponentially declining gas accretion rate with a characteristic time-scale $\tau_{\rm gas}$, coupled with assumptions about stellar gas recycling back into the ISM (as done by e.g. Pégase; Le Borgne & Rocca-Volmerange 2002). Again, the apparent insensitivity of our M_*/L estimates argues against this having a large impact on our stellar mass estimates; it may, however, lead to improvements in our estimates of both Z and $\langle t_* \rangle$.

6.2.2 *Allowing for secondary stellar population components*

For the present work, we have limited ourselves to considering only smooth, exponentially declining SFHs. A number of authors have attempted to incorporate or allow for more complicated SFHs in their SPS calculations. One approach has been to increase the dimensionality of the SPL parameter space by introducing additional SP components as short bursts (e.g. Kauffmann et al. 2003a; Brinchmann et al. 2004; Gallazzi et al. 2005).

We can also use Fig. 15 to explore what impact the inclusion of more complicated SFHs in our SPL might have. Consider what happens to any of the models in Fig. 15 with the addition of a secondary burst of star formation. If any two of the models shown in Fig. 15 are combined in any proportion, the evolutionary track of the resultant SP must necessarily lie between the individual tracks of the two distinct SP components. If you were to combine any two SPs with the same dust and metallicity, but different SFHs, the result will necessarily still lie trapped within the region of colour space spanned by the smooth models. That is, so long as any secondary SP has the same dust and metallicity, it will not be easily distinguishable from any of our existing smooth models.

This insight is significant in terms of the results of Gallazzi & Bell (2009). These authors find that SFH-related degeneracies mean that the inclusion of bursty SFHs among the SPL model templates does little to reduce this bias for bursty galaxies. Further, there is the potential that the inclusion of too many bursty SPL models can lead to biases in *non*-bursting galaxies. In other words, because these scenarios cannot be distinguished on the basis of their SEDs, a bias in M_*/L is inevitable, whether that be a small bias for the many 'smooth SFH' galaxies, or a larger bias for the fewer bursty galaxies. Note, too, that in this picture, the degree of the bias is strongly dependent on the assumed priors.

The implication from the above, then, is that the inclusion of models with mixed metallicities and/or multi-component SFHs will improve our SP parameter estimates only to the extent that they expand the high-dimensional colour space spanned by the full ensemble of SPL models. Then, multi-component SFHs will only expand the SPL colour space if and only if the different components are allowed to have different amounts of dust and/or metals.

In order to meaningfully incorporate dual-component SPs thus requires the addition of at least five parameters to describe the secondary SP: the equivalent of a 'formation time'; some characteristic time-scale for the secondary SFH (i.e. an e-folding time, or some equivalent); its mass relative to the primary; and then both its metallicity and its dust content. With the current architecture of our SPS code, such an expansion of parameter space is completely impractical.

6.2.3 *The need for a new conceptual framework*

We would therefore appear to have reached the practical limits of complexity that can be covered by discrete grid-search-like fitting algorithms using a static SPL. Independently of the question of NIR

data issues, any future expansion of the model parameter space will have to be accompanied by a change in the conceptual framework that underpins our SPS modelling procedure.

Alternative approaches apply standard dimensionality-reducing techniques, developed in the context of data compression, to the problem. One example is the MOPED algorithm (Heavens, Jiminez & Lahov 2000; Panter, Heavens & Jiminez 2003), which uses a variant of principal component analysis (PCA) to efficiently perform a 23-component SPS fit to full SDSS spectra, including a generalized 10-bin SFH (see also VESPA; Tojeiro et al. 2008). Another example is KCORRECT (Blanton & Roweis 2007), which uses the technique of non-negative matrix factorization (NMF). The idea here is to determine the basis set of template spectra that optimally describes the observed SEDs of real galaxies. The NMF basis set is constructed as a combination of SP template spectra; this means that the basis templates constructed using the NMF algorithm can be considered as SPS template spectra with realistic, multi-component, non-parametric SFHs. The principal motivation for and advantage of these approaches is that they can eliminate entirely the need to assume parametric forms for the SFH. In the context of the above discussion, the operational advantage of such approaches can be thought of as shifting from sampling a static and semi-regular grid of parameter values to a dynamic sampling of an expanded but continuous parameter space.

The main point to take from the above discussion is that proper modelling of the optical-to-NIR SED shapes of galaxies is considerably more challenging than modelling just the optical SED. Part of the reason for this is that, for a fixed optical colour, a galaxy's optical–NIR colour is sensitive to both Z and $\langle t_* \rangle$. Said another way, it is precisely because a galaxy's optical–NIR SED can break metallicity-related degeneracies that it becomes necessary to model each of these quantities in more detail – indeed, in more detail than is practical within the present architecture of our code. On the other hand, the relatively strong degeneracies between a galaxy's SP properties and its optical SED shape means that SPS fitting of optical SEDs can be done using a relatively crude SPL.

7 SUMMARY

The primary purpose of this work has been to present and describe the 'first generation' estimates of stellar mass and other ancillary SP parameters for galaxies in the GAMA survey. We have deliberately set out to use widely used and accepted techniques to derive these values, partially in order to allow for the fairest comparison between results from GAMA and other high- and low-redshift galaxy surveys. Our stellar mass estimates are based on the synthetic SP models of BC03, assuming a Chabrier (2003) IMF and a Calzetti et al. (2000) dust law (Section 3.1). In constructing the SPL that forms the backbone of the calculation, we have used the standard assumptions of a single metallicity and a continuous, exponentially declining SFH for all SPs, with dust modelled as a single, uniform screen (Section 3.2).

The most significant 'non-standard' element of the calculation is that we use a Bayesian approach when determining the fiducial values of all parameters and their associated uncertainties (Section 3.3). As we show in Fig. 5, this decision has an important *systematic* effect on the parameter estimates: averaged over the full GAMA sample, the *most likely* (in a Bayesian sense) values of M_*/L_i are $\sim$0.10 dex higher than those taken from the single *best-fitting* (i.e. maximum-likelihood) SP template. While the Max-Planck-Institut für Astrophysik – Johns Hopkins University (MPA-JHU) mass estimates for SDSS used a Bayesian approach, this is not (yet) generally done in high-redshift studies.

7.1 Comparisons between GAMA and SDSS

Through comparison between the GAMA- and SDSS-derived values of M_*/L_i and M_* (Appendix B), we highlight two important issues with the SDSS `model` photometry. First, we show that as a measure of total flux, the SDSS `model` photometry has serious systematics as a function of (true) Sérsic index (Fig. B1). For galaxies best fit by an exponential `model` profile, the differential bias between $n \sim 0.5$ and $n \sim 1.5$ is $\gtrsim 0.2$ mag ($\sim$20 per cent); for those best fit by a de Vaucouleurs `model` profile, the differential bias between $n \sim 2$ and $n \sim 8$ is $\approx$0.7 mag (a factor of 2). These systematic biases in total luminosity translate directly to biases in total stellar mass: this may be the single largest source of error in the SDSS mass estimates based on `model` photometry.

Secondly, if we apply our algorithm to the SDSS `model` SEDs, we see very large differences between our derived values and those from the MPA-JHU catalogues (Fig. B3). These differences are directly tied to strong systematic differences between the SDSS `model` and GAMA `auto` colours (Section B1.2), such that the net systematic offset in $(u-z)$ is as large as 0.2 mag (Fig. B2). We therefore suggest that it may be more appropriate to use `petro`, rather than `model`, SEDs when analysing data from the SDSS photometry catalogues.

Despite these differences in the SDSS and GAMA photometry, the fiducial GAMA values of M_*/L_i are in excellent agreement with those found in the latest generation MPA-JHU catalogue for SDSS DR7 (Section B), which have been shown to be well consistent with dynamical mass estimates (Taylor et al. 2010b). (We investigate the consistency between GAMA-derived stellar and dynamical mass estimates in a companion paper.) As we argue in Section B4, the inclusion of a dust prior in the MPA-JHU stellar mass estimation algorithm may have effectively circumvented the potential bias in SP parameters based on the SDSS `model` photometry; using the GAMA `auto` photometry, we find no need for such a prior.

7.2 NIR data (currently) do more harm than good

For the present generation of stellar mass estimates, we have elected *not* to include the available *YJHK* NIR photometry in the SED-fitting; the SP parameters presented here are based on fits to the optical *ugriz* SEDs only.

As summarized in Section 4.4, there are three reasons for this decision. First, none of the commonly used SP models (BC03; M05; CB07) provides good fits to the full optical-to-NIR SEDs (Fig. 7). Secondly, while the inclusion of the NIR data does have an impact on the derived values – the median value of M_* goes down by 0.15 dex when the NIR data are included – the values derived with the NIR are formally inconsistent with those derived from just the optical data for a large fraction of galaxies. Both of these facts suggest inconsistencies between the optical-to-NIR SED shapes of real galaxies and those of the models in our SPL. The third reason is that we find that the 'random' differences in inferred SP parameters – particularly E_{B-V}, Z and $\langle t_* \rangle$ – using different SSP models are larger than the formal uncertainties once the NIR data are included. That is, our SP parameter estimates become significantly model dependent when, and only when, the NIR data are used.

That said, the *systematic* differences in the inferred SP parameters based on different SSP models are small: for M_*/L, the median difference in the value of M_*/L using the BC03 and M05 SSP models is just 0.02 dex. We therefore consider it unlikely that the

failure of the models to adequately accommodate the NIR data is due to differences between (or uncertainties in) the stellar evolution models themselves.

This leaves two possibilities: there may be problems in the NIR data, and/or the SPL that we have used is insufficient to describe the full range of SPs that exist in the local Universe. These issues will have to be addressed – both through additional data validation and verification and through expansion of our SPL to include additional metallicities and possibly more sophisticated SFHs – in the construction of future generations of the GAMA stellar mass catalogues. We have discussed possible avenues for expanding our SPL in Section 6.2, and conclude that any future expansion to our SPL parameter space will have to be accompanied by a change in the conceptual framework of our SPS fitting procedure. We would appear to have reached the practical limit of complexity for a simple grid-search-like approach using a static SPL.

Note that future catalogues will make use of considerably deeper VST optical imaging from KIDS and VISTA NIR imaging from the VIKING survey. In this context, it is highly significant that, even with the present photometry, the accuracy of our SP parameter estimates is not currently limited by photometric signal-to-noise, but by systematics. With the exception of the *u*-band, the photometric errors are smaller than the error floor of 0.05 mag that we have imposed for the fits (see Section 3.2). The extent to which the deeper data will improve on the present SPS fitting results will depend crucially on how well the data can be self-consistency cross-calibrated, including biases due to PSF- and aperture-matching, colour gradients, and background subtraction, as well as the basic photometric calibration. As a corollary to this, it will be incumbent upon us to ensure that the model photometry in any future SPL can be considered accurate to the same level as the real data, i.e. $\lesssim$0.05 mag.

7.3 The robustness and reliability of our optical-derived stellar mass estimates

In light of our decision to ignore the presently available NIR data, we have reexamined the commonly held belief that NIR data are crucial to deriving a robust and reliable estimate of stellar mass (Section 5). We use generic properties of the SP models to demonstrate that on its own, the *i*-band flux is nearly as good a representation of the total SP as is the NIR flux (Section 5.1). More quantitatively, assuming a constant M_*/L_i or M_*/L_K, it is possible to use L_i or L_K to estimate M_* to within a factor of 5.5 or 4.5, respectively.

Using a similar argument, we show that the variation in M_*/L_i *at fixed* $(g-i)$ is $\lesssim$0.5 dex (Fig. 10). The effect of dust is largely to shift galaxies along the $(g-i)$–M_*/L_i relation. Dust thus does not significantly affect one's ability to estimate M_*/L_i using $(g-i)$. Similarly, we show that, for a given model, variations in age, SFH, and metallicity act to largely preserve the relation between M_*/L_i and $(g-i)$ colour (Fig. 11). Further, we show that multi-component SPs (e.g. a burst superposed over an old and passive SP) fall within the same region of $(g-i)$–M_*/L_i space as the exponentially declining SFHs that comprise our SPL. In this way, based on generic properties of stellar evolution models, we show that $(g-i)$ colour can be used to estimate M_* to within a factor of $\lesssim$2, even considering the well-known dust–age–metallicity degeneracy, and even for multi-component SPs (Section 5.2).

Finally, we consider the empirical relation between M_*/L_i and $(g-i)$ for GAMA galaxies. It is significant that the observed relation between M_*/L_i and $(g-i)$ is both more linear and considerably tighter (at fixed colour, the scatter in M_*/L_i is $\lesssim$0.1 dex) than we might expect by simply taking the prior-weighted average of the models in our SPL (Fig. 12). This implies that the full *ugriz* SED shape contains additional information not found in the $(g-i)$ colour, and, further, that this information is sufficient to exclude a significant range of the models in our library. The tightness of the $(g-i)$–M_*/L_i relation is not merely a consequence of the central limit theorem.

In other words, there are two completely separate reasons why $(g-i)$ is an excellent predictor of M_*/L_i, both of which are entirely fortuitous. First, variations in age, SFH, dust and metallicity – independently and *en masse* – largely preserve the $(g-i)$–M_*/L_i relation. This is a coincidence produced by the physics of stellar evolution. Secondly, the SPs of real galaxies produce a $(g-i)$–M_*/L_i relation that is both tighter and more nearly linear than might be expected from SP models alone. This is a coincidence produced by the physics of galaxy formation and evolution.

In this sense, presuming that both our derived values and their associated uncertainties are reasonable, we have effectively 'calibrated' the $(g-i)$–M_*/L_i relation to a precision of $\lesssim$0.1 dex (1σ). The derived relation offers a reliable and robust means for observers to derive stellar masses based on minimal information. Similarly, under the (non-trivial) assumption that the relation does not evolve strongly with redshift, it offers a simple and transparent basis for fair comparison between results derived from GAMA and other low- and high-redshift surveys. As an important caveat on the use of this relation, however, any and all systematic errors or uncertainties in the SPL itself – including, e.g., the IMF and errors in the treatment of the *optical* stellar evolution tracks – are not included in the quoted uncertainty of 0.1 dex. On the other hand, the relation given does offer a solid means for other surveys to compare their stellar mass-centric measures to those from GAMA under the identical assumptions.

7.4 Concluding remarks

The stellar mass estimates we have described have been or will be used for a wide variety of recent and ongoing studies by the GAMA collaboration. These include studies of variability in the stellar IMF (Gunawardhana et al. 2011), measurement of the $z \approx 0$ mass function (Baldry et al. 2011), the properties of galaxies at the lowest end of the Hα luminosity function (Brough et al. 2011) and studies of galaxy demographics in the field (Taylor et al., in preparation), in groups (Prescott et al. 2011), and in filaments (Pimbblett et al., in preparation). Further, they provide an important benchmark for any and all future GAMA stellar mass and SP parameter estimates.

In line with the legacy goals of the GAMA survey, these stellar mass estimates are also being made publicly available for use by the wider astronomical community as part of GAMA DR2 (scheduled for mid-2011). GAMA's unique combination of depth and survey area has been deliberately chosen to bridge the gap between large-scale local Universe surveys like 6dFGS, SDSS and 2dFGRS, and deep surveys of the high-redshift Universe like VVDS, DEEP-2 and zCOSMOS. Particularly in combination with these other major surveys, the GAMA catalogues are intended to provide a valuable laboratory for studies of galaxy formation and evolution.

ACKNOWLEDGMENTS

GAMA (www.gama-survey.org) is a joint European–Australasian project being undertaken using the Anglo-Australian Telescope. GAMA is funded by the STFC (UK), the ARC (Australia), the AAO, and the participating academic institutions. The GAMA input and photometric catalogues rely on data taken as part of both the Sloan Digital Sky Survey (SDSS; www.sdss.org) and the UKIRT

Infrared Deep Sky Survey (UKIDSS; www.ukidss.org). Funding for the SDSS has been provided by the Alfred P. Sloan Foundation, the US Department of Energy, the National Aeronautics and Space Administration (NASA), the Japanese Monbukakusho, the Max Planck Society, the Higher Education Funding Council for England, and other participating institutions. SDSS is managed by the Astrophysical Research Consortium for the participating institutions. Complementary imaging of the GAMA regions is being obtained by a number of independent survey programmes including *GALEX* MIS, VST KIDS, VISTA VIKING, WISE, *Herschel*-ATLAS, GMRT, and ASKAP, ultimately providing UV to radio coverage.

REFERENCES

Abazajian K. V. et al., 2009, ApJS, 182, 543
Adelman-McCarthy J. K. et al., 2008, ApJS, 175, 297
Baldry I. K., Balogh M. L., Bower R. G., Glazebrook K., Nichol R. C., Bamford S. P., Budavari T., 2006, MNRAS, 373, 469
Baldry I. K. et al., 2010, MNRAS, 404, 86
Baldry I. K. et al., 2011, MNRAS, submitted
Bell E. F., de Jong R. S., 2001, ApJ, 550, 212
Bell E. F., McIntosh D. H., Katz N., Weinberg M. D., 2003, ApJS, 149, 289
Benitez N., 2000, AJ, 536, 571
Bertin E., Arnouts S., A&A, 117, 393
Blanton M. R., Roweis S., 2007, ApJ, 133, 734
Blanton M. R., Eisenstein D., Hogg D. W., Schlegel B. K., Brinchmann J., 2005, ApJ, 629, 143
Brammer G. B., Van Dokkum P. G., Coppi P., 2008, ApJ, 686, 1503
Brinchmann J., Ellis R. S., 2000, ApJ, 536, L77
Brinchmann J., Charlot S., White S. D. M., Tremonti C., Kauffmann G., Heckman T., Brinkmann J., 2004, MNRAS, 351, 1151
Brough S. et al., 2011, MNRAS, 413, 1236
Bruzual G., 1993, ApJ, 273, 105
Bruzual G., 2007, preprint (astro-ph/0703052)
Bruzual G., Charlot S., 2003, MNRAS, 344, 1000
Calzetti D., Armus L., Bohlin R. C., Kinney A. L., Koorneef J., Storchi-Bergmann T., 2000, ApJ, 533, 682
Chabrier G., 2003, ApJ, 586, L133
Charlot S., Fall S. M., 2000, ApJ, 539, 718
Cimatti A. et al., 2008, A&A, 481, 21
Cole S., Norberg P., Baugh C. M., Frenk C. S., 2001, MNRAS, 326, 255
Cole S., Percival W. J., Peacock J. A., Norberg P., Baugh C. M., Frenk C. S., 2005, MNRAS, 362, 505
Colless M. et al., 2001, MNRAS, 328, 1039
Colless M. et al., 2003, preprint (arXiv:astro-ph/0306581)
Conroy C., White M., 2010, ApJ, 712, 833
Conroy C., Gunn J. E., White M., 2009, ApJ, 699, 486
Conti A. et al., 2003, AJ, 126, 2330
Cutri R. M. et al., 2003, Explanatory Supplement to the 2MASS All Sky Data Release and Extended Mission Products. NASA/IPAC Infrared Science Archive, http://www.ipac.caltech.edu/2mass/releases/allsky/doc/
Davis M. et al., 2003, in Guhathakurta P., ed., Proc. SPIE Vol. 4834, Discoveries and Research Prospects from 6- to 10-m class Telescopes II. SPIE, Bellingham, p. 161
Djorgovsky S., Davis M., 1987, ApJ, 313, 59
Doi M. et al., 2010, AJ, 139, 1628
Dressler A., 1980, ApJ, 313, 42
Dressler A., Lynden Bell D., Burstein D., Davies R. L., Faber S. M., Terlevich R., Wegner G., 1987, ApJ, 313, 42
Driver S. P., Liske J., Cross N. J. G., De Propris R., Allen P. D., 2005, MNRAS, 360, 81
Driver S. P., Popescu C. C., Tuffs R. J., Liske J., Graham A. W., Allen P. D., de Propris R., 2007, MNRAS, 379, 1022
Driver S. P., Norberg P., Baldry I. K., Bamford S. P., Hopkins A. M., Liske J., Loveday J., Peacock J. A., 2009, A&G, 50, 5.12
Driver S. P. et al., 2011, MNRAS, 413, 971
Dye S. et al., 2006, MNRAS, 372, 1227
Eales S. et al., 2010, PASP, 122, 499
Faber S. M., Jackson R. E., 1976, ApJ, 204, 668
Fischera J., Dopita M., 2005, ApJ, 619, 340
Gallazzi A., Bell E. F., 2009, ApJS, 185, 253
Gallazzi A., Charlot S., Brinchmann J., White S. D. M., Tremonti C. A., 2005, MNRAS, 362, 41
Gallazzi A., Charlot S., Brinchmann J., White S. D. M., 2006, MNRAS, 370, 1106
Gunawardhana M. et al., 2011, MNRAS, 415, 1647
Guo Y. et al., 2009, MNRAS, 398, 1129
Hambly N. C. et al., 2008, MNRAS, 384, 637
Heavens A., Jiminez R., Lahov O., 2000, MNRAS, 317, 965
Hewett P. C., Warren S. J., Leggett S. K., Hodgkin S. T., 2006, MNRAS, 367, 454
Hill D. T. et al., 2011, MNRAS, 412, 765
Hodgkin S. T., Irwin M. J., Hewett P. C., Warren S. J., 2009, MNRAS, 394, 675
Hogg D. W., Baldry I. K., Blanton M. R., Eisenstein D. J., 2002, preprint (astro-ph/0210394v1)
Jones D. H. et al., 2004, MNRAS, 355, 747
Jones D. H. et al., 2009, MNRAS, 399, 683
Kannappan S. J., Gawiser E., 2007, ApJ, 657, L5
Kauffmann G. et al., 2003a, MNRAS, 341, 33
Kauffmann G. et al., 2003b, MNRAS, 341, 54
Kauffmann G., White S. D. M., Heckman T. M., Ménard B., Brinchmann J., Charlot S., Tremonti C., Brinkmann J., 2004, MNRAS, 353, 713
Kelvin L. et al., 2011, MNRAS, submitted
Kriek M. et al., 2010, ApJ, 722, L64
Kron R. G., 1980, ApJS, 43, 305
Lanyon-Foster M. M., Conselice C. J., Merrifield M. R., 2007, MNRAS, 380, 571
Lawrence A., Warren S. J., Almaini O., Edge A. C., Hambly N. C., Jameson R. F., Lucas P., Casali M., 2007, MNRAS, 379, 1599
Le Borgne D., Rocca-Volmerange B., 2002, A&A, 386, 466
Le Fèvre O. et al., 2005, A&A, 439, 845
Leitherer C. et al., 1999, ApJS, 123, 3
Lilly S. J. et al., 2007, ApJS, 172, 70
Liske J., Lemon D. J., Driver S. P., Cross N. J. G., Couch W. J., 2003, MNRAS, 344, 307
Loveday J. et al., 2011, MNRAS, in press (arXiv:1111.0166v1, doi:10.1111/j.1365-2966.2011.20111.x)
Maraston C., 2005, MNRAS, 362, 799
Maraston C., Daddi E., Renzini A., Cimatti A., Dickinson M., Papovich C., Pasquali A., Pirzkal N., 2006, ApJ, 652, 85
Martin D. C. et al., 2005, ApJ, 619, L1
Minkowski R., 1962, in McVittie G. C., ed., Proc. IAU Symp. 15, Problems of Extragalactic Research. Macmillan, New York
Morrissey P., Conrow T., Barlow T. A., Small T., Seibert M., Wyder T., Budavári T., 2007, ApJS, 173, 682
Muzzin A., Marchesini D., van Dokkum P. G., Labbé I., Kriek M., Franx M., 2009, ApJ, 701, 1839
Nicol M.-H., Meisenheimer K., Wolf C., Tapken C., 2011, ApJ, 727, 51
Panter B., Heavens A. F., Jimenez R., 2003, MNRAS, 343, 1145
Peng C. Y., Ho L. C., Impey C. D., Rix H.-W., 2002, AJ, 124, 266
Percival S. M., Salaris M., Cassisi S., Pietrinferni A., 2009, ApJ, 690, 427
Petrosian V., 1976, ApJ, 210, L53
Popescu C. C., Misiriotis A., Kylafis N. D., Tuffs R. J., Fischera J., 2000, A&A, 362, 138
Pozzetti L. et al., 2007, A&A, 474, 443
Prescott M. et al., 2011, MNRAS, 417, 1374
Robotham A. et al., 2010, Publ. Astron. Soc. Aust., 27, 76
Sandage A., Visvanathan N., 1978, AJ, 225, 742
Saunders W. et al., 2004, in Moorwood A. F. M., Masanori I., eds, Proc. SPIE Vol. 5492, Ground-based Instrumentation for Astronomy. SPIE, Bellingham, p. 389
Schombert J., 2011, arXiv:1107.1728v1
Scoville N. J. et al., 2007, ApJS, 172, 1

Sharp R. et al., 2006, in McLean I. S., Masanori I., eds, Proc. SPIE Vol. 6269, Ground-based and Airborne Instrumentation for Astronomy. SPIE, Bellingham, p. 14
Shen S., Mo H. J., White S. D. M., Blanton M. R., Kauffmann G., Voges W., Brinkmann J., Csabai J., 2003, MNRAS, 343, 978
Skrutskie M. F. et al., 2006, ApJ, 131, 1163
Stoughton C. et al., 2002, AJ, 123, 485
Strateva I. et al., 2001, AJ, 122, 1861
Strauss M. A. et al., 2002, AJ, 124, 1810
Taylor E. N. et al., 2009, ApJ, 694, 1171
Taylor E. N., Franx M., Glazebrook K., Brinchmann J., van der Wel A., van Dokkum P. G., 2010a, ApJ, 720, 723
Taylor E. N., Franx M., Brinchmann J., van der Wel A., van Dokkum P. G., 2010b, ApJ, 722, 1
Tinsley B. M., 1978, ApJ, 222, 14
Tinsley B. M., Gunn J. E., 1976, ApJ, 203, 52
Tojeiro R., Heavens A. F., Jiminez R., Panter B., 2007, MNRAS, 381, 1252
Tonry J. L., Blakeslee J. P., Ajhar E. A., Dressler A., 2000, ApJ, 530, 625
Tremonti C. A. et al., 2004, ApJ, 613, 898
Tuffs R. J., Popescu C. C., Völk H. J., Kylafis N. D., Dopita M. A., 2004, A&A, 419, 821
Tully R. B., Fisher J. R., 1977, A&A, 54, 66
van Dokkum P. G., 2008, ApJ, 74, 29
Walcher C. J. et al., 2008, A&A, 491, 713
Walcher C. J., Groves B., Budavári T., Dale D., 2011, Ap&SS, 331, 1
Welikala N., Connolly A. J., Hopkins A. M., Scranton R., Conti A., 2008, AJ, 677, 970
Wijesinghe D. et al., 2011, MNRAS, 410, 2291
Wilkins S. M., Hopkins A. M., Trentham N., Tojeiro R., 2008, MNRAS, 391, 363
Wolf C., Meisenheimer K., Rix H.-W., Borch A., Dye S., Kleinheinrich M., 2003, A&A, 401, 73
Wolf C. et al., 2004, A&A, 421, 913
Worthey G., 1994, ApJS, 95, 107
Wright E. L., Eisenhardt P. R. M., Mainzer A. K., Ressler M. E., 2010, AJ, 140, 1868
Wuyts S., Franx M., Cox T. J., Hernquist L., Hopkins P. F., Robertson B. E., van Dokkum P. G., 2009, ApJ, 696, 348
York D. G. et al., 2000, AJ, 120, 2131
Zibetti S., Charlot S., Rix H.-W., 2009, MNRAS, 400, 1181

APPENDIX A: NUMERICAL EXPERIMENTS – SPS FITTING OF MOCK GALAXY PHOTOMETRY

In this Appendix, we examine our ability to recover the known SP parameters of a set of mock galaxies with a realistic distribution of SP parameters. To this end, we have used the results of our 'live' SPS fits to the real GAMA *ugriz* data to construct a catalogue of mock galaxy photometry. Specifically, for each galaxy, we have taken the SPL template SED that most closely matches its 'most likely' SP values, added random perturbations commensurate with the actual observational uncertainties for the original galaxy and then fed that photometry back into the SPS fitting algorithm. Note that the distribution of SP parameters in this mock catalogue is, by construction, the same as what we observe for GAMA galaxies, i.e. it is quite different to our assumed priors.

In Section 4.1, we have argued that our seeming inability to satisfactorily fit the optical-to-NIR SEDs of GAMA galaxies calls into question the validity of SP parameter estimates inferred from such fits. We have also argued that our inability to predict NIR photometry based on just the optical SEDs – with the implication that the NIR contains additional information not found in the optical – does not imply that the optical cannot be used to reliably infer stellar mass-to-light ratios. In order to provide context for these arguments, we will first spend some time looking at the quality of the photometric fits to the mock photometry in Section A1. We will then go on to look at how accurately and precisely we can recover the known SP parameters of the mock galaxies in Section A2.

A1 Quality of fits

A1.1 How well can you fit the optical-to-NIR SEDs?

In Fig. A1, we show the analogue of Fig. 7 for this mock galaxy catalogue. Let us look first at the right-hand panel of this figure, in which we show the difference between the known, input photometry,

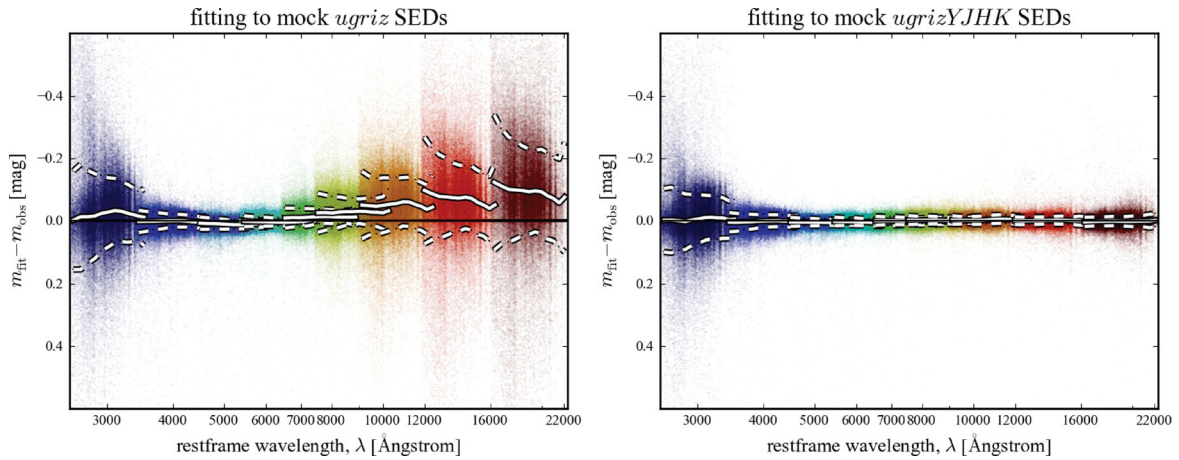

Figure A1. Quality of the SED fits for mock galaxy photometry. This figure shows the residuals from the SED fits to the mock galaxy photometry described in Appendix A. The left-hand panel shows the residuals when fitting only the optical *ugriz*-bands; the right-hand panel shows those for fits to the full *ugrizYJHK* SEDs. All symbols and their meanings are as in Fig. 7, to which these plots should be compared. As argued in Section A1, the fact that the optical-only fits tend to overpredict the 'true' NIR fluxes is possibly due to the mismatch between our assumed priors and the 'true' multi-variate distribution of SP parameters within the mock catalogue. At least qualitatively, the similar residuals seen in Fig. 7 for the real galaxies therefore do not suggest that the fits are necessarily 'bad'. Further, and in contrast to Fig. 7, we are able to reproduce or describe the full optical-to-NIR shapes of the mock galaxies. This strongly suggests that the large residuals seen in Fig. 7 are due to problems in the data, shortcomings in the SPL models, or both. In any case, the large systematics seen in the right-hand panels of Fig. 7 mean that the results of the optical-to-NIR SED fits must be treated with some suspicion.

and the recovered, output photometry, after fitting to the mock *ugrizYJHK* SEDs. The residuals are at the millimag level for all but the *u*-band; the median residual in the *u*-band is still just 0.02 mag. None of these residuals is significant at the 0.1σ level. Put simply, the quality of the fits is near perfect.

A1.2 How well can you predict NIR photometry based on optical SEDs?

Now consider the left-hand panel of Fig. A1, in which we show the residuals when fitting to the mock *ugriz* SEDs. Our primary interest here is in how well we are able to predict NIR photometry for the mock galaxies using their *ugriz* SEDs. In comparison to Fig. 7, there are three features of this plot that we find striking.

First, it is clear that, as in Fig. 7, the NIR photometry predicted from the mock optical SEDs is systematically too bright. Quantitatively, however, in comparison to Fig. 7, the size of the discrepancy is considerably smaller. For the mock galaxies, the residuals are $\lesssim$0.1 mag; roughly half that seen for real GAMA galaxies. Compared to the photometric errors, the median significance of these offsets is 0.5, 0.7, 1.3 and 1.7σ in the *Y JHK*-bands; again, roughly half that seen in Fig. 7.

Secondly, the residuals for the mock galaxies show a qualitatively different dependence on restframe wavelength/redshift than is seen in Fig. 7. Whereas for real galaxies, the offsets in each individual band appear to be the greatest at the highest and lowest redshifts, for the mock galaxies, the offsets grow rather smoothly for longer and longer wavelengths. That is, for the mock galaxies, our results suggest that one's ability to predict NIR photometry depends primarily on how far one is willing to extrapolate off the red end of the observed optical SED.

Thirdly, we note that, just as in Fig. 7, we do see some residuals in the optical bands. Quantitatively, the median residual in each of the *ugriz*-bands is -0.02, $+0.00$, $+0.01$, $+0.00$ and -0.01 mag, respectively; in all cases, this is insignificant at the level of $\lesssim 0.2\sigma$. In comparison to those seen in Fig. 7, these residuals are again roughly half the size as for real galaxies, but show a qualitatively similar 'curvature' with wavelength.

A1.3 Implications for SED fitting – the subtle role of priors

Given the above, what are we to make of the (very slight) residuals in the *ugriz* fits? Since we are fitting to the same *ugriz* photometry in both of the above numerical experiments, the additional information provided by the NIR photometry must exclude some of those models that are consistent with the optical data on its own. In other words, the models allowed by the five-band fits span a broader range of SP parameter values than those allowed by the nine-band fits; the set of SPL templates allowed by the five-band fits must be a superset of those allowed by the nine-band fits. (We will look at precisely how the SP parameter estimates change with the inclusion of the NIR data in a moment; for now, let us keep the discussion general.) The implication of this, as is well known, is that an optical SED simply does not encode sufficient information to fully constrain a galaxy's SP parameters.

Naturally, the models are distinguished by their SED shapes. From the fact that the *ugriz* fits tend to overpredict the 'true' NIR photometry of our mock galaxies, we know that the optical-only fits are consistent with a range of SPL models, and that these models are on average redder than the 'real' solution. Now, the fiducial parameter estimate is derived from marginalizing over the PDF à la equation (5). Again, for the optical-only fits, this includes a disproportionally large number of models with the 'wrong' SED shape, specifically models that are substantially too red in the NIR. But these models will also have (very) slightly different optical SED shapes. Hence the very slight offsets seen in the optical bands when the NIR data are excluded.

Consider what would happen if we were to significantly change the form of our assumed priors in such a way as to make these redder fits less likely – for example, by making higher dust extinctions or metallicities less likely than lower ones. Reducing the prior probability of these models directly reduces their contribution to the integral, which defines the Bayesian 'most likely' parameter value in equation (5). This implies that if we were to use more realistic priors, we might be able to do a substantially better job of predicting the NIR photometry based on the optical SEDs. (Parenthetically, this may be why KCORRECT is so successful at predicting NIR photometry from optical colours.)

In this context, it is significant that the *ugriz* residuals seen when fitting only to the optical bands disappear when the NIR data are included. This shows that our SPS algorithm is in fact able to near-perfectly match galaxies' SEDs given sufficient information, where we have also now shown that 'sufficient information' means both optical and NIR photometry. Furthermore, this is possible even despite the fact that the assumed priors are very different from the real distribution intrinsic to the data. These experiments thus suggest that the GAMA optical-plus-NIR data set can, in principle, be used to constrain galaxies' SP parameters to the extent that the quality of the fits is not overly sensitive to the assumed priors. Said another way (and more accurately), so long as NIR data are available, the way that the photometry uncertainties map on to SP parameter space means the allowed range of SP parameters is small enough that the assumption that the priors are *locally* flat is a good one.

As we have already pointed out in Section 7, there is an important corollary to the idea that we are, in principle, able to near-perfectly match the 'observed' SEDs in our mock catalogue. Once NIR data are included, the quality of the fits is no longer limited by the amount of information that is encoded in the data, but instead by how closely the SPs that comprise the SPL represent those found in the wild. This means that, to the extent that more complex SPs – including more complicated SFHs, a mix of stellar metallicities and patchy dust geometries – change the shape of a galaxies SEDs, these effects must be adequately folded into the construction of the SPL. In other words, precisely *because* NIR data provide the additional SP parameter information not found in the optical, robust and reliable fits to optical-plus-NIR SEDs require more sophisticated SPLs (see also Section 6.2).

A2 Parameter recovery

Whereas in the previous section we have focused on how well our SPS fitting algorithm is able to describe or reproduce the SED shapes of mock galaxies, we now turn to the question of how well galaxies' SP parameters can be constrained from their broad-band SED shapes.

A2.1 Reliability

In Fig. A2, we show how accurately we are able to recover the SP parameters associated with the mock galaxies based on either their optical-only (left-hand panels) or optical-to-NIR (right-hand

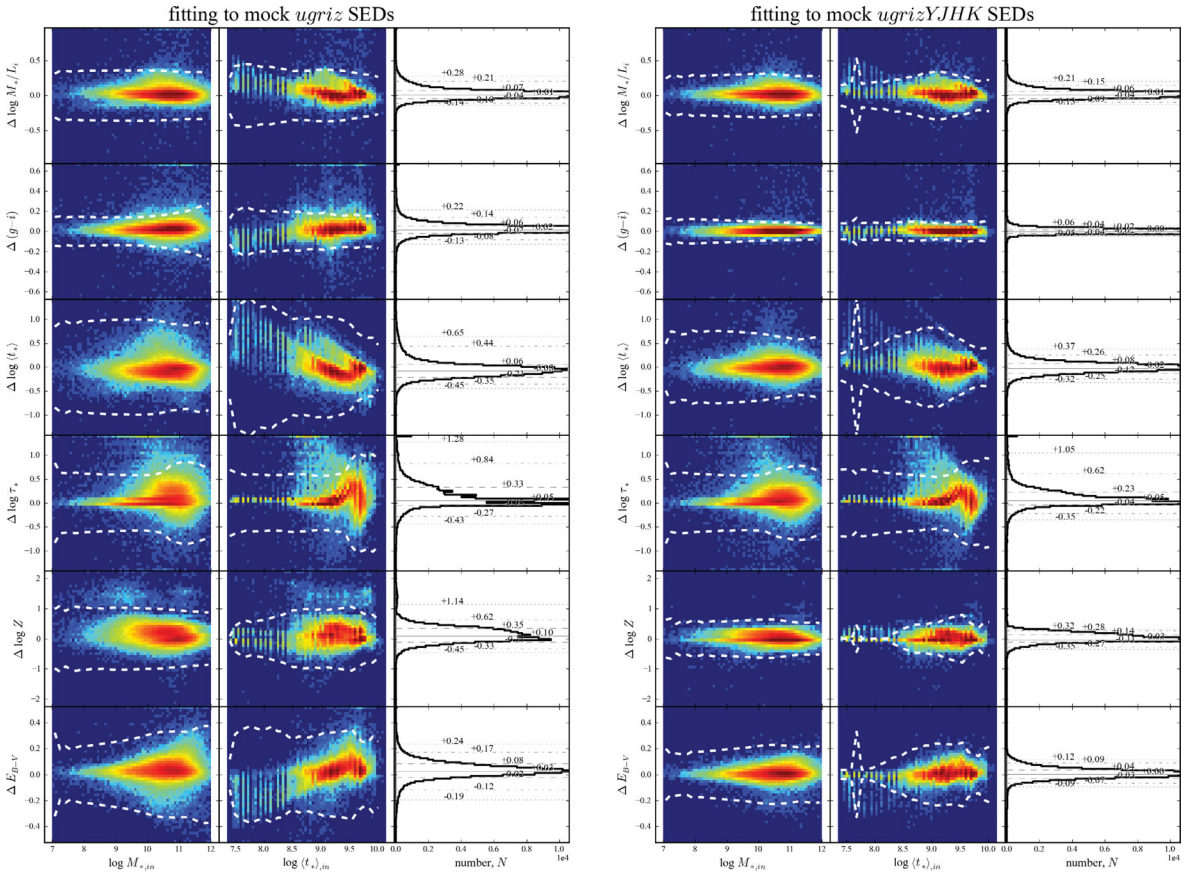

Figure A2. SP parameter recovery for mock galaxy photometry. These plots are based on the mock galaxy photometry described in Appendix A; each panel shows the difference between the 'known' parameter of a mock galaxy and that inferred from a fit to optical-only (left-hand panels) or optical-plus-NIR (right-hand panels) photometry. In all cases, the 'Δ's on the *y*-axes should be understood as 'recovered-minus-input'; the quantities on the *x*-axes relate to the 'known' value. As in Figs 8 and 9, the histograms show the distribution in the 'Δ's, with the percentile equivalents of the $\pm 0/1/2/3\sigma$ points as marked. In both cases, we are able to recover the SP parameters of the mock galaxies with little to no systematic bias. This is particularly true for M_*/L_i: the reliability of the optical-plus-NIR-derived estimates (median error ∼0.05 dex) is not significantly better than that based on only the optical (median error ∼0.06 dex).

panels) photometry, and in the face of realistic observational uncertainties. In all cases, the 'Δs' on the *y*-axis should be understood as being the 'output-minus-input' parameter value, plotted as a function of the 'known', input value from the mock catalogue. As in Figs 8 and 9, the colour-scale shows the logarithmic data density, with the percentile equivalents of the $\pm 0/1/2/3\sigma$ points of the distributions given with the histograms at right.

The first – and, in the context of our main argument, the most crucial – point to be made from these plots is that we are able to recover the M_*/L_is of the mock galaxies with no discernible bias based on the optical SEDs alone. Further, the M_*/L_i determinations derived from fits including NIR photometry are not all that much more reliable than those based only on the optical data: on the one hand, the 1σ 'errors' are $^{+0.07}_{-0.04}$ dex; on the other, they are $^{+0.06}_{-0.04}$ dex.

In line with the results of the previous section, where we have shown that our priors tend to over-weight models with redder SED shapes, the optical-only fits imply slightly too-red $(g-i)$ colours. Empirically, the error is $0.015^{+0.057}_{-0.020}$ mag; using the slope of the empirical $(g-i)$–M_*/L_i relation, this translates to an error of $0.010^{+0.040}_{-0.014}$ dex in M_*/L_i.

For the other SP parameters, as for M_*/L_i, the inclusion of NIR data does not appear to be crucial to obtaining reliable parameter estimates. The median offset between the known and the recovered SP parameter values for the optical-plus-NIR fits is not clearly less than for the optical-only fits. That said, the inclusion of NIR data clearly does reduce the 'random' error in the derived SP parameters – that is, the robustness – particularly in the case of Z and E_{B-V}, as well as τ for those 'passive' galaxies with $t/\tau \gg 1$.

A2.2 Robustness

The final question to be considered here is how precisely galaxies' SP parameters can be constrained based on SED fits with or without NIR photometry. We address this question with reference to Fig. A3, which shows the distribution of the formal uncertainties in SP parameter estimates derived from the mock photometric catalogues, based on fits to optical-only (left-hand panels) or optical-plus-NIR (right-hand panels) SEDs.

Looking at the global distribution of uncertainties for all galaxies in the mock catalogues, the greatest effect of the NIR is to reduce the uncertainties on Z and on $\langle t_* \rangle$. The median value of $\Delta \log Z$ goes from 0.35 to 0.25 dex with the inclusion of the NIR, while the median value of $\Delta \log \langle t_* \rangle$ goes from 0.26 to 0.19 dex. By comparison, the improvement in $\Delta \log E_{B-V}$ is relatively minor: the

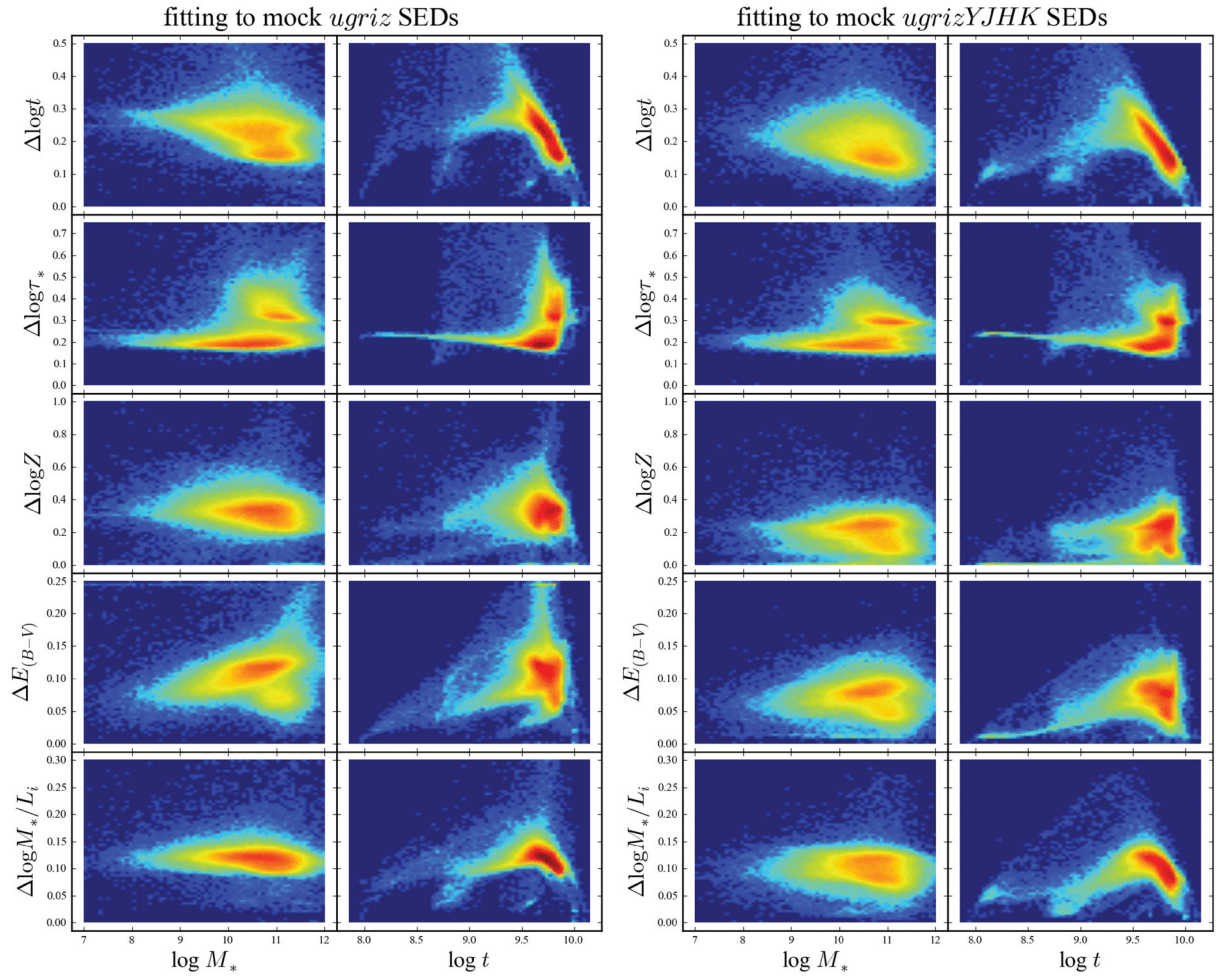

Figure A3. Precision of SP parameter estimates for mock galaxies. In analogy to Fig. 4, these plots show the distributions of the formal uncertainties in the inferred SP parameter values for the mock galaxies based either on the optical-only (left-hand panels) or on the optical-plus-NIR (right-hand panels) SED fits. If the NIR data are included, the formal uncertainties in the recovered values of all of t, τ, Z, and E_{B-V} are considerably smaller than if they are excluded. However, the formal uncertainties in M_*/L are virtually unchanged. By breaking the age–metallicity–dust degeneracies, NIR data provide a better estimate of the ancillary SP parameters, but this has little to no bearing on the precision with which M_*/L can be constrained.

median value goes from 0.10 dex to 0.07 mag. It is interesting to compare this improvement in $\Delta\log\langle t_*\rangle$ to that in $\Delta\log t$, which goes from 0.21 to 0.18 dex, and in $\Delta\log\tau$, which remains nearly unchanged at 0.21 dex. This suggests that while NIR photometry helps to break degeneracies between $\langle t_*\rangle$ and Z (and to a lesser extent E_{B-V}), and so helps provide a better constraint on instantaneous mean stellar age, it does not provide much additional information concerning the precise SFH.

But again, the NIR data do not lead to a substantial improvement in the accuracy with which M_*/L_i can be determined: the median value of $\Delta\log M_*/L_i$ goes from 0.11(4) dex (≈30 per cent) to 0.09(8) dex (≈25 per cent). The NIR encodes virtually no additional information concerning a galaxy's stellar mass that cannot be found in the optical.

This fact has one important implication for future stellar mass catalogues. In the previous section, we found that we were able to recover M_*/L_i for the mock galaxies with an empirical 1σ 'error' on the order of ±0.05 dex, both with and without the inclusion of NIR data, i.e. more precisely than might be expected from the formal uncertainties of ±0.10 dex. The reason for this is that, in generating the mock photometry, we have added random photometric errors commensurate with the random photometric errors; in the fitting, on the other hand, we include an error 'floor' of 0.05 mag. This error is intended to account for potential differential systematic errors between the different photometric bands. The implication is thus that the accuracy of our stellar mass determinations is not limited by signal-to-noise ratio (i.e. the random observational uncertainties in the photometry in each band), but instead by the relative accuracy of the photometry in the different bands with respect to one another (i.e. differential systematic errors between the different bands). This means that the extent to which the considerably deeper VST and VISTA photometry will improve our ability to constrain galaxies' stellar masses will depend crucially on how well we are able to control systematic photometric errors in the different bands, including the accuracy of the basic photometric calibrations.

APPENDIX B: COMPARISONS BETWEEN GAMA AND SDSS

In this Appendix, as a means of validating our stellar mass estimates, we compare them to the latest generation of stellar mass

estimates from the MPA-JHU catalogue for SDSS DR7.[15] The motivation for this comparison stems from the fact that the MPA-JHU mass-to-light ratios have been well tested; they thus provide a useful set of benchmark measurements. They are in excellent agreement with other frequently used MPA-JHU mass determinations; e.g. the Kauffmann et al. (2003a) DR4 catalogue.[16] That is, the (SED-derived) DR7 mass estimates are wholly consistent with values derived from spectra. Further, Taylor et al. (2010b) have compared the DR7 MPA-JHU stellar masses to dynamical mass estimates, derived using the Sérsic-fit structural parameters of Guo et al. (2009). Based on the consistency between these stellar mass estimates and dynamical mass estimates, Taylor et al. (2010b) have argued that any differential biases in the stellar-to-dynamical mass ratio as a function of SP parameters may be as low as $\lesssim$0.12 dex ($\sim$40 per cent).

There are two facets to this comparison: differences in SDSS and GAMA photometry from which the mass estimates are derived, and differences in the algorithms used to actually derive the mass estimates. We compare the GAMA and SDSS photometry in Section B1. After describing the key differences between the SDSS and GAMA algorithms in Section B2, we will then look at our ability to reproduce the SDSS stellar mass and stellar mass-to-light ratio values using first SDSS `model` and then the GAMA `auto` photometry in Sections B3 and B4, respectively. In this way, we hope to identify whether and how these differences affect the derived values for M_*/L and M_*. Before we begin, let us again stress that the rationale behind this comparison is that the SDSS mass-to-light ratios have been well tested; our main concern is thus our ability to reproduce the SDSS values for the galaxies that are common to both SDSS and GAMA.

B1 Comparing the GAMA and SDSS photometry

The basic SDSS catalogue contains two different photometric measures in each of the *ugriz*-bands. Following the recommendation of Stoughton et al. (2002), it is standard practice to use `model` photometry to construct multi-band SEDs. This photometry comes from fitting either an exponential or a de Vaucouleurs profile to the observed light distribution. The choice of profile shape and structural parameters (i.e. effective radius, ellipticity and position angle) is based on the *r*-band image. For the fits to the *ugiz*-bands these parameters are then held fixed, so that only overall normalization is allowed to vary; this is then the `model` flux. The MPA-JHU mass estimates are based on the `model` SEDs taken from the basic SDSS catalogue.

The second photometric measure is the `petro` magnitude, which is based on the idea of Petrosian (1976). This flux is measured within a flexible circular aperture, the size of which is based on the observed (radial) surface brightness profile. Again following the recommendations of Stoughton et al. (2002), it is standard practice to use the `petro` photometry as a measure of total flux. Accordingly, when we consider $\log M_*$ below, we will scale the MPA-JHU mass estimates by $-0.4(r_{\texttt{petro}} - r_{\texttt{model}})$ to obtain 'total' mass estimates. This is directly analogous to our use of SEDs based on matched-aperture `auto` photometry, scaled to match `sersic` total magnitudes.

[15] Available via http://www.mpa-garching.mpg.de/SDSS/

[16] The median offset is -0.01 dex, with a scatter on the order of 0.1 dex; see http://www.mpa-garching.mpg.de/SDSS/DR7/mass_comp.html

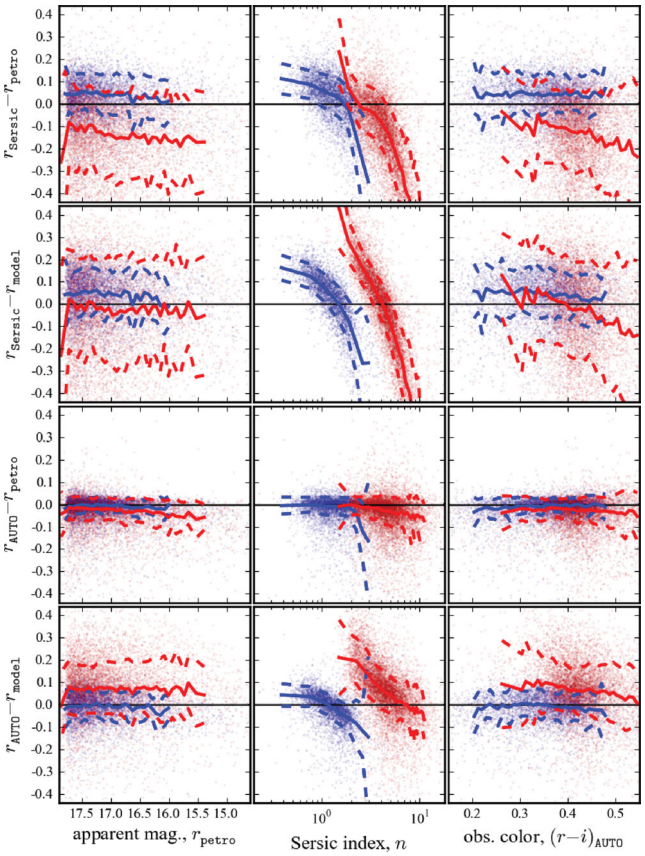

Figure B1. Comparison between GAMA and SDSS *r*-band magnitude measurements. Each panel of this figure shows the difference between a GAMA and an SDSS measure of *r*-band magnitude as a function of (left to right) apparent magnitude, GAMA-derived Sérsic index, *n*, or observed colour. Within each panel, we make the distinction between those objects that are fit using an exponential profile (blue) or a de Vaucouleurs profile (red) for the SDSS `model` photometry. For GAMA, we use `auto` magnitudes to construct multi-colour SEDs, and the *r*-band `sersic` magnitude to measure total flux; it is standard SDSS practice to use `model` magnitudes for SEDs, and the `petro` magnitude as a measure of total flux. As expected, the `petro` magnitude misses an increasingly large fraction of total flux for galaxies with higher values of *n*. It seems that the GAMA `sersic` magnitude may miss up to $\lesssim$ 10 per cent of flux for $n \lesssim 2$ galaxies. The SDSS `model` magnitudes (which assume either $n = 1$ or $n = 4$) have strong *n*-dependent systematics: where the assumed value of *n* in the `model` underestimates the 'true' value of *n*, the `model` flux overestimates the total magnitude by up to $\sim$0.3 mag. Between $n \sim 2.5$ and $n \sim 8$, the size of the differential effect for de Vaucouleurs-like galaxies is greater than a factor of 2.

B1.1 r-band magnitudes

In Fig. B1, we compare the different GAMA and SDSS photometric measures of *r*-band flux. This comparison is based on the $\sim$12 000 SDSS-targeted galaxies that appear in the GAMA catalogue. In this figure, we distinguish between those galaxies whose SDSS `model` photometry is based on an exponential (blue points) or a de Vaucouleurs (red points) profile.

In each case, it is clear that the relation between different photometric measures depends most strongly on profile shape (parametrized by the GAMA *r*-band derived Sérsic index, *n*). For $n \gtrsim 2$, the difference between the GAMA Sérsic-fit and SDSS `petro` fluxes is more or less as expected: the fraction of missed flux increases rapidly from $\approx$0 for $n \sim 2$ to $\approx$ 0.1 mag for $n \approx 4$ galaxies, to $\approx$0.5 mag for $n \approx 8$, and so on.

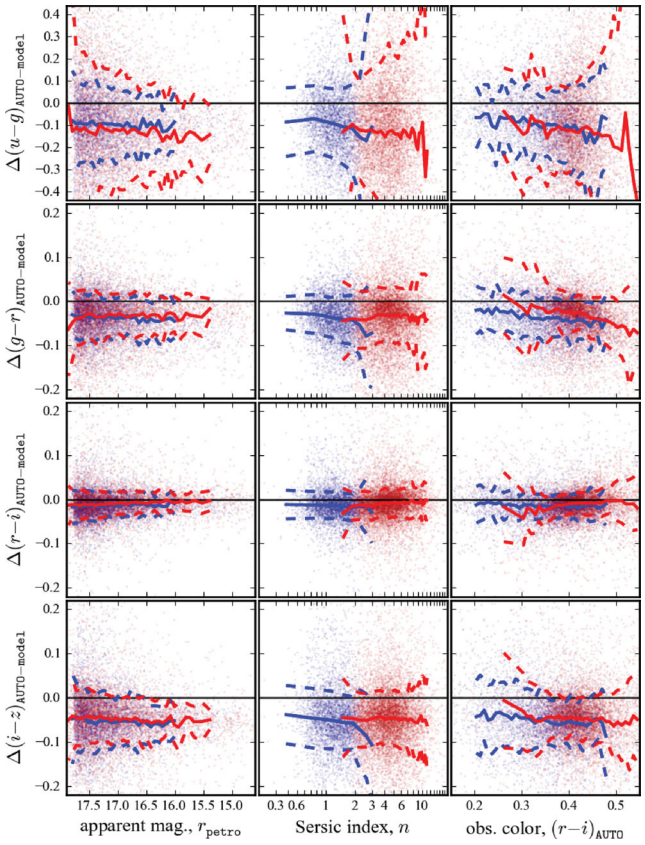

Figure B2. Comparison between GAMA `auto` and SDSS `model` colours. Each row shows the difference in the measured, observers' frame colours of galaxies as reported in the GAMA and SDSS catalogues; the 'Δ' should be understood as meaning GAMA-minus-SDSS. From left to right, the panels show the systematic differences in observed colour as a function of apparent magnitude, Sérsic index and $(r - i)$ colour. As in Fig. B1, we make the distinction between those objects that are fit using an exponential profile (blue) or a de Vaucouleurs profile (red) for the SDSS `model` photometry. The points show the data themselves; the lines show the binned biweight mean and scatter. The SDSS `model` SEDs are systematically redder than the GAMA `auto` ones: the cumulative difference in $(u - z)$ is 0.2 mag. Note that we find no such systematic differences between the GAMA `auto` and SDSS `petro` colours. This suggests that the SDSS data may be better analysed using `petro` rather than `model` SEDs.

The most striking feature of Fig. B1 is the large n-dependent differences between the SDSS `model` and GAMA `sersic` and `auto` photometry. The crucial assumption behind the SDSS `model` photometry is that galaxies can be well described by a Sérsic profile with either $n = 1$ or $n = 4$. For those galaxies with a GAMA-derived $n \approx 1$, the results in Fig. B1 suggest that the GAMA `sersic` photometry may miss $\lesssim$10 per cent ($\lesssim$0.04 dex) of the flux; for galaxies with $n \approx 4$, there is excellent agreement between the GAMA `sersic` and SDSS `model` photometry.

Away from these points, however, the `model` photometry has large systematic biases: for both exponential- and de Vaucouleurs-like galaxies, where the `model` Sérsic index ($n = 1$ or $n = 4$) is higher than the 'true' value, the `model` flux significantly overestimates the 'true' total flux. For exponential-like galaxies, the size of the differential effect is nearly 0.3 mag between $n \approx 0.5$ and $n \approx 2$; for de Vaucouleurs-like galaxies, the effect is greater than 0.7 mag (a factor of 2!) between $n \approx 2$ and $n \approx 8$. This is thus a major, if not the largest, source of error in the SDSS mass estimates.

B1.2 ugriz SEDs

In Fig. B2, we show a comparison between galaxies' optical colours as reported in the GAMA and SDSS catalogues. Although the current GAMA optical photometry is derived from the SDSS imaging data, there are systematic differences between the galaxy colours – as measured using the GAMA `auto` and SDSS `model` photometry – that are used as the basic inputs to the stellar mass estimation calculation.

In comparison to the GAMA `auto` photometry, the SDSS `model` SEDs are systematically redder across all bands. Quantitatively, the observed 'GAMA `auto`-minus-SDSS `model`' offsets are $\Delta(u - g) = -0.10$ mag, $\Delta(g - r) = -0.03$ mag, $\Delta(r - i) = -0.01$ mag and $\Delta(i - z) = -0.05$ mag; the cumulative offset between u and z is thus -0.2 mag. These offsets are not a strong function of apparent brightness. Particularly for the bluer bands, they may depend weakly on Sérsic index. Further, looking at the right-hand panels of this figure, there is the hint that the offsets vary systematically with observed colour: this immediately suggests that colour gradients may play a role in one or the other of these measurements.

Note that we find no such systematic offsets between the GAMA `auto` and SDSS `petro` colours. That is, whatever the cause of the discrepancies seen in Fig. B2, it is specific to the SDSS `model` photometry. We also note that the fact that the `model` photometry is so sensitive to n implies that `model`-derived SEDs may be badly biased by colour gradients: a small change in Sérsic index across different bands will produce a relatively large differential bias in the inferred fluxes. Taken together, these two points suggest that that when using SDSS photometry, even despite the fact that the `petro` photometry is not PSF-matched, it may provide a better basis for constructing multi-colour SEDs than `model` photometry.

B2 Differences between the MPA-JHU and GAMA mass estimation algorithms

Unlike previous MPA-JHU catalogues (e.g. Kauffmann et al. 2003a; Brinchmann et al. 2004; Gallazzi et al. 2005) that were based on the SDSS spectroscopy, the DR7 MPA-JHU stellar mass estimates are based on fits to the *ugriz* photometry. The first difference between the MPA-JHU and GAMA algorithms is that for the MPA-JHU mass estimates, the observed photometry has been corrected for contributions from emission lines [which are not included in the (BC03 models), under the assumption that the global emission line contribution is the same as in the spectroscopic fibre aperture.

Like the one described here, the MPA-JHU SPL is based on the BC03 SSP models, and assuming a Chabrier (2003) IMF. Whereas we use a Calzetti et al. (2000) dust law, however, the SDSS SPL spectra use the Charlot & Fall (2000) curve to account for dust obscuration. At least in terms of the values of M_*/L, as we shall show, this difference is not important.

The biggest structural difference between the GAMA and SDSS stellar mass calculations is that, whereas we have constructed our SPL by sampling a semi-regular grid in (t, τ, Z, E_{B-V}) parameter space, the MPA-JHU masses are based on a library made up of large number of Monte Carlo realizations of different SFHs. The priors in the MPA-JHU algorithm are applied in the Monte Carlo sampling of the allowed parameter space (see also Gallazzi et al. 2005). Specifically, the model ages are randomly sampled from a uniform distributions in both formation time (over the range $1.5 < t_{\rm form}/[{\rm Gyr}] < 13.5$) and in the exponential decay rate ($0 < \gamma/[{\rm Gyr}^{-1}] < 1$; here,

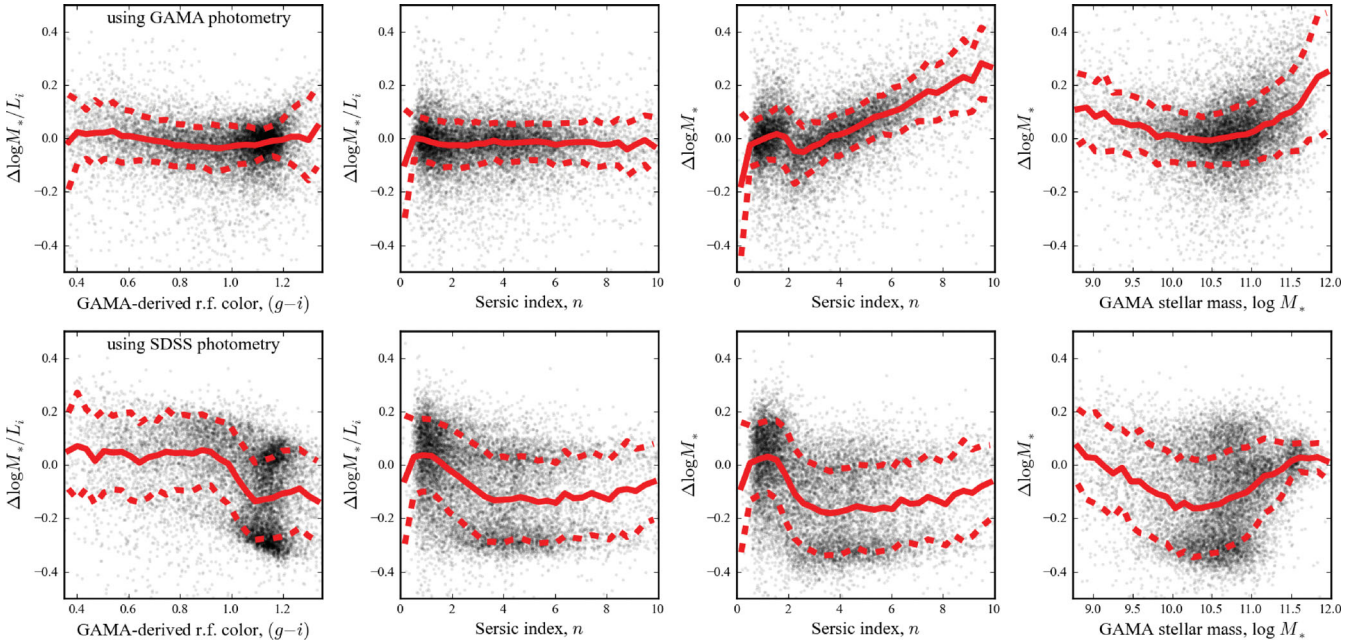

Figure B3. Stellar mass-to-light ratios and stellar masses inferred from SDSS `model` and GAMA `auto` photometry. In the lower panels, the 'GAMA-derived' values are based on SEDs constructed from the SDSS `model` photometry; in the upper panels, the 'GAMA' values are derived from the GAMA `auto` SEDs. In each case, the 'Δ's should be understood as GAMA-minus-SDSS. Using the SDSS `model` photometry, we do not do a particularly good job at reproducing the (well-tested) SDSS-derived values of M_*/L; using the GAMA `auto` photometry, the agreement is very good (the reasons for this are discussed at greater length in Sections B1.2 and B4). While the fiducial GAMA M_*/Ls agree very well with those from SDSS, the GAMA masses are systematically larger than the SDSS values. This can only be explained by missed flux in the SDSS `model` photometry. For the highest values of n and M_*, GAMA finds $\gtrsim$0.15 dex more light/mass than SDSS (see also Section B1.1 and Fig. B1).

γ can be thought of as $1/\tau$). The models also include a number of secondary bursts of star formation. The burst probabilities are normalized such that 10 per cent of galaxies experience a burst in the last 2 Gyr, with the burst times uniformly distributed between $t_{\rm form}$ and the time of observation. Individual bursts are treated as constant star formation rate events lasting for $10^{7.5}$ to $10^{8.5}$ yr. The strength of each burst is parametrized by the mass relative to the 'underlying' population, which is logarithmically distributed between $0.03 < f_{M_*,\rm burst} < 0.4$. Finally, the assumed metallicity prior is logarithmic for super-solar metallicities, with lower metallicities downweighted through an assumed prior distribution of the form $(\log Z)^{1/3}$ for $0.02 < Z < 0.2$. The prior distribution of dust extinctions is derived from the SDSS Hα/Hβ ratios (Jarle Brinchmann, private communication; 2009 September 24). In terms of their SPLs, the major differences between the MPA-JHU and GAMA calculations are thus the inclusion of bursts, and the different form of the metallicity distribution prior.

The decision to randomly sample parameter space, rather than to use a (semi-)regular grid, has two consequences. First, it makes it possible to accommodate bursts in the SPL (as described above); this would not be computationally practical to include into an SPL grid like ours, since it would expand the parameter space by (at least) an additional three dimensions. Secondly, the nominal SDSS parameter values given in the MPA-JHU catalogues are the median of the posterior probability distribution, i.e. the 50 per cent confidence upper/lower limits, rather than the 'most likely' value from explicit marginalization over the PDF. That said, at least for the GAMA mass estimates, we find that the (probability weighted) median and mean values of M_*/L are in extremely good agreement. This implies, albeit weakly, that the posterior probability distributions for M_*/L are roughly symmetric about the mean/median value.

B3 Comparison between the MPA-JHU- and GAMA-derived mass estimates: I. Using GAMA `auto` SEDs

How well are we able to reproduce the MPA-JHU values for M_*/L_i and M_*? We address this question in Fig. B3. In the left-hand panels of this figure, we compare the stellar masses that we derive based on SDSS photometry to those given in the MPA-JHU catalogue: these panels thus probe differences in the GAMA and SDSS algorithms applied to the same data. In the upper panels of this figure, we compare our fiducial stellar mass estimates based on GAMA photometry. It is thus these panels that most interest us, inasmuch as these panels show a direct comparison between the well-tested MPA-JHU values and our own.

Looking at the upper panels of Fig. B3, the agreement between our fiducial mass estimates and the MPA-JHU values is very good: the random scatter between the two values of M_*/L_i is small, and there are no obvious systematics. More quantitatively, our `auto`-derived M_*/L_is agree with the MPA-JHU values with a biweight mean and scatter in $\Delta M_*/L$ of -0.01 and 0.07 dex, respectively. The offsets in M_*/L_i as a function of restframe colour are at the level of a few per cent ($\lesssim$0.02 dex). That said, there are large differences in the total inferred M_* as a function of n. Given that we can faithfully reproduce the M_*/Ls, this discrepancy can only be explained by differences in the total Ls. These results thus suggest that missed flux is a significant problem in the MPA-JHU SDSS masses.

B4 Comparison between the MPA-JHU- and GAMA-derived mass estimates: II. Using SDSS `model` SEDs

While we have now shown very good agreement between the MPA-JHU- and GAMA-derived M_*/Ls for SDSS galaxies, the comparison

presented in the previous section mixes the effects of differences in both the input photometry and the mechanics of the stellar mass estimation algorithms. The next obvious question is how well the two algorithms agree when applied to the same data.

Looking at the lower panels of Fig. B3, it is clear that we *do not* do a particularly good job of reproducing the MPA-JHU masses when using the SDSS `model` photometry to construct galaxy SEDs. We see mild systematic differences between the GAMA- and SDSS-derived values of M_*/L as a function of both colour and structure, and the random scatter between the two estimates is not small: $\sim$0.15 dex. Further, there is a distinct population of de Vaucouleurs-like ($n \sim 2.5$–6) galaxies with rest frame $(g-i)$ colours of $\sim$1.1 whose GAMA-derived M_*/Ls are lower by $\sim$0.25 dex.

How can it be that we do a better job at reproducing the MPA-JHU M_*/Ls when using the GAMA photometry than we do using the SDSS `model` photometry? At least part of the answer is directly tied to differences between the SDSS `model` and GAMA `auto` photometry. We have made similar comparisons using SDSS `petro` photometry. Perhaps unsurprisingly, given the close agreement between the `petro` and `auto` colours, we do not find any strong systematic differences between the GAMA- and SDSS-derived values in this case. The median value of $\Delta M_*/L_i$ is -0.02 dex; the rms $\Delta M_*/L_i$ is 0.11 dex. There are no obvious trends in $\Delta M_*/L_i$ with apparent magnitude, Sérsic index or inferred restframe colour. That is, the problem appears to be specific to the SDSS `model` photometry.

We have seen that the SDSS `model` SEDs are systematically redder than those constructed using GAMA `auto` magnitudes. The effect of these differences can be understood by looking at Fig. 1. Using the `model` SEDs, the 'problem' objects (i.e. those galaxies where there are large differences in the GAMA- and SDSS-derived stellar mass estimates) prefer templates with young ages ($\langle t_* \rangle \lesssim 3$ Gyr), high metallicity ($Z \approx 0.05$; the highest value allowed in our BC03 library) and moderately heavy dust extinction ($E_{B-V} \sim 0.2$). When using the GAMA `auto` photometry, these objects come out to be considerably older ($\langle t_* \rangle \sim 6$ Gyr), lower metallicity ($Z \sim 0.01$) and less dusty ($E_{B-V} \sim 0.05$–0.10).

Looking carefully at the $1.0 < (g-i) < 1.2$ region of Fig. 1, one can see that immediately above the broad strip defined by the older, low-SSFR models (colour-coded red in the upper-left panel), there is a narrower strip of models with ages $\langle t_* \rangle \sim 1$ Gyr (colour-coded green). In the lower-left panel of Fig. 1, these models can also be seen to have $Z = 0.05$ (colour-coded red). Note that this is precisely the regime where we see the largest differences in the GAMA- and MPA-JHU-derived M_*/Ls.

This explains the differences between our stellar mass estimates based on the `auto` and `model` photometry: the 0.13 mag offset in $(u-r)$ between the `model` and `auto` photometry pushes these galaxies up towards the upper edge of the region of colour space spanned by the models. The redder $(u-r)$ `model` colours thus open up a qualitatively different, young, high-metallicity SP solution for what would otherwise be old, lower-metallicity galaxies.

But how is it that the SDSS stellar mass estimates, which are based on the 'wrong' `model` SEDs still get the 'right' value for M_*/L? We speculate that the answer may lie in the different metallicity and/or dust priors used by the MPA-JHU team. The priors most strongly affect galaxies with low metallicities and dust extinction (Jarle Brinchmann, private communication; 2009 September 24); these are precisely the kinds of galaxies where we see the greatest discrepancies between the GAMA- and MPA-JHU-derived values of M_*/L. That is, it would seem that the 'problem' dustier, younger and high-metallicity solutions preferred by the `model` photometry are down-weighted by the inclusion of a dust prior in the MPA-JHU algorithm. Here, too, the SDSS decision to use the median, rather than the mean, of the PDF will help to reduce any susceptibility to a 'bimodality' in the PDF, and so reduce the likelihood of choosing these 'problem' solutions. In our case, using the GAMA `auto` photometry, the inclusion of such a prior is unnecessary.

Again, our primary motivation for performing this comparison is to test our ability to reproduce the well-tested MPA-JHU values for M_*/L. Given that we have demonstrated our ability to do so using our own *ugriz* photometry, and the fact that without access to the MPA-JHU algorithm we are unable to perform any more detailed tests or comparisons, we have not investigated this issue any further.

B5 Summary

In this Appendix, we have compared the GAMA photometry and stellar mass estimates to those from SDSS. Our primary motivation for this comparison is that, based on consistency with dynamical mass estimates, it has been argued that the SDSS stellar mass estimates have no strong systematic, differential biases for galaxies with different SPs (Taylor et al. 2010b). When using the GAMA photometry, we find excellent agreement between our fiducial estimates of M_*/Ls and those from SDSS, with no strong differential biases as a function of mass, colour or structure. This argues against there being any strong biases in the GAMA M_*/L estimates. We will investigate this further through comparison between the GAMA stellar and dynamical mass estimates in a separate work.

We have also shown that there are significant differences between the GAMA and SDSS estimates of total flux, which come from `sersic` and `model` photometry, respectively. These differences are a strong function of n: for $n = 1$ and $n = 4$ galaxies, where the SDSS `model` assumes the 'right' value of n, we find excellent agreement between the two surveys' photometry. Away from these points, however, the SDSS `model` photometry is strongly biased. For de Vaucouleurs-like galaxies, the size of the differential bias in the `model` photometry is as large as a factor of 2. This will have a significant impact on a number of stellar mass-centric measurements like the mass function or the size–mass relation.

We have shown that there are significant systematic differences between the GAMA- and SDSS-derived colours, which are derived from `auto` and `model` photometry, respectively. The SDSS `model` photometry is systematically redder, with a net offset of $\Delta(u-z) = 0.2$ mag. We suggest that it may be better to use `petro`, rather than `model` photometry when analysing SDSS data: we find no such differentials between the GAMA `auto` and SDSS `petro` photometry. When we apply our SPS pipeline to the `model` photometry, our stellar mass estimates no longer agree well with those from SDSS. We suggest that these differences may be explained by the different priors used in the SDSS pipeline, which act to downweight young, moderately dusty, and high-metallicity SPS fits. In the case of SDSS, their priors would seem to effectively circumvent the potential biases in M_*/L that these photometric biases might produce. In our case, we are able to reproduce the well-tested SDSS values with no need for such priors.

This paper has been typeset from a TEX/LATEX file prepared by the author.